Expanding Ultrafast Photoacoustics for Investigation of Mechanical Properties and Thermal Transport

by

Hyun Doug Shin

B.S. Chemistry, University of California, Berkeley (2012)

Submitted to the Department of Chemistry
in partial fulfillment of the requirements for the degree of

Doctor of Philosophy

at the

MASSACHUSETTS INSTITUTE OF TECHNOLOGY

June 2019

Signature redacted

Author .....
Department of Chemistry
May 10, 2019

Signature redacted

Certified by ....
Keith A. Nelson
Haslam and Dewey Professor of Chemistry
Thesis Supervisor

Signature redacted

Accepted by ....
Robert W. Field
Haslam and Dewey Professor of Chemistry
Chairman, Department Committee on Graduate Students

This doctoral thesis has been examined by a Committee of the Department of Chemistry as follows:

Signature redacted

Professor Moungi G. Bawendi.....
Chairman, Thesis Committee
Lester Wolfe Professor of Chemistry

Signature redacted

Professor Keith A. Nelson.....
Thesis Supervisor
Haslam and Dewey Professor of Chemistry

Signature redacted

Professor Robert W. Field.....
Member, Thesis Committee
Haslam and Dewey Professor of Chemistry

Expanding Ultrafast Photoacoustics for Investigation of Mechanical Properties and Thermal Transport

by

Hyun Doug Shin

Submitted to the Department of Chemistry
on May 10, 2019, in partial fulfillment of the
requirements for the degree of
Doctor of Philosophy

Abstract

To address the need for broadband mechanical spectroscopy, femtosecond laser pulses were used to generate and detect acoustic waves. To expand the acoustic phonon frequency bandwidth and range, a thin metal film, a strongly magnetostrictive galfenol film, and strained piezoelectric InGaN/GaN multiple quantum wells were used as transducers. Acoustic wave detection methods included monitoring of optical transmittance/reflectance, polarization, and diffraction over time.

A magnetostrictive material galfenol ($Fe_{1-x}Ga_x$) with 80 percent iron and 20 percent gallium was used as an acoustic transducer using demagnetostriction effect. Galfenol showed great potential as an optimal transducer for the ultrafast magnetostriction in both longitudinal and shear modes.

Strained piezoelectric InGaN/GaN semiconductor superlattices were used to generate and to study longitudinal THz acoustic phonons in GaN based structures. During the investigation of the lifetime of up to a 1.4 THz frequency acoustic phonons, specular reflection from an air/GaN free surface was observed. The photo-excitation of THz acoustic phonons in layered structures was introduced as an effective noninvasive tool to investigate the integrity of the fabrication process. This study opened many possibilities for studying mechanical properties and thermal phonons.

Next, thermal conductivity reduction due to carrier-phonon interactions was presented. Phonon contributions are critical in heat transport in semiconductors and insulators. To isolate the carrier contributions to the scattering events, photo-excited carriers were generated in silicon through pulsed laser excitation. To measure thermal conductivity changes, time-domain thermoreflectance and transient thermal grating techniques were employed with a carefully timed additional excitation pulse for carrier generation.

Thesis Supervisor: Keith A. Nelson
Title: Haslam and Dewey Professor of Chemistry

Acknowledgments

Three boys are on bikes, roaming the countryside, over steep hills and narrow ridges, between the rice fields are their playgrounds. That is my favorite childhood memory. I was a child who liked to go exploring and was always engaged in the investigation and perturbation of natural systems. As I grew up, my natural curiosity matured into an interest in mathematics and science. In particular, chemistry mesmerized me by its puzzle-solving and its carefully designed experiments to test its theories. During my journey, I have had truly inspiring and enthusiastic mentors and teachers who ignited my passion for learning and teaching. It is my great honor to talk about some of the most amazing people that I have had the privilege to interact with.

I have met many brilliant people from around the world, but I cannot even picture any better advisor and role model than Professor Keith Nelson. Across many departments at MIT, Keith is well-known for asking critical questions and starting fascinating discussions on a broad array of topics. His passion for scientific creativity and problem solving always inspired me and everyone around him. Each conversation with him on science or any other topic motivated me to learn more about the world. I will never be able to forget that magical moment when a turkey flew across Keith's backyard. The sun was about to set after a social event at Keith's house, and a wild turkey appeared and soared into the sky hiding in a tree. That night, I learned that turkeys roost in trees at night. Every moment with Keith was a learning experience for me, and I cannot sufficiently express how I grateful I am to have had the opportunity to spend time with him. I had many ups and downs during my stay at MIT, but Keith has always been incredibly supportive and caring at every moment. I am truly thankful to Keith.

There are so many people I want to talk about, because I would not be here today without them. One of the greatest inspirations for me to pursue science was Professor Alexander Pines, my undergraduate research supervisor and professor for my first classes at UC Berkeley. From the first half of general chemistry to a seminar on order, disorder, fractal and chaos, his genuine passion for science inspired me to

learn about real world tools like NMR to investigate chemical dynamics. He once said, "If I am able to help cultivate a stimulating environment, one that encourages the students' natural curiosity and creativity, and opens for them a door to the mysteries of science and the thrill of learning, my efforts are worthwhile." This philosophy well describes both the research environment that I experienced in his lab and the inspiration I have received from his educational efforts.

I am grateful that I had the opportunity to work with and learn from Kara Manke, Alexei Maznev, Ryan Duncan, Jiawei Jhou, Ievgeniia Chaban, and Thomas Pezeril. Kara introduced me to the world of photoacoustics and taught me how to run experiments. Alex has incredible knowledge about photoacoustics among many other topics in physics and has been eager to share the wisdom and know-how. His level of knowledge and matching skills in the field never ceased to amaze me throughout the years. It was a great pleasure to share the scientific journeys with Ryan, especially during Son et Lumiér and beam times at SLAC LCLS and BESSY II. Working with Jiawei was eye opening, since he taught me how theorists approach experiments. Even though we worked together briefly, conducting experiments with Genia was productive and exciting. Finally, Thomas has taught me so much experimental know-how and introduced me to exciting materials to study with picosecond ultrasonics in such a short period of time.

The past and present Nelson group has provided me with incredible resources and lots of fun. I have never met Christoph Klieber in person, but I am grateful to him for tools and techniques left behind. Sharly Fleischer, Harold Hwang, and Nathaniel Brandt in Team THz taught me how to align and work with optics when I first joined the lab. It was a lot of fun to play volleyball together even with my busted right shoulder and to have mind-boggling discussions with group members including Andreas Steinbacher, Dylan Arias, Jeff Eliason, Samuel Teitelbaum, Benjamin Ofori-Okai, Prasahnt Sivarajah, David Veysset, Jian Lu, Colby Steiner, Frank Gao, Yaquing Zhang, Xian Li, Yu-Hsiang Cheng, Dmitro Martynowych, Jake Siegel, Brandt Pein, Blake Dastrup, Jude Deschamps, Eric Sung, Yongbao Sun, Stephanie Teo, Patrick Wen, Leora Dresselhaus-Cooper Tristan Pitt, and Yuchen Sun.

The works in this thesis would not be possible without amazing collaborators. I would like to express my sincere gratitude to Jateen Gandhi from University of the Houston who grew the piezoelectric superlattice samples, C. K. Sun and his group members for their work with superlattices, Dong Sung Choi for the help with oxide layer growths, Massimilano Marangolo and Eddrief Mahmoud for galfenol sample growths, Bolin Liao and Gang Chen for electron-phonon coupling and thermal transport simulations and experiments, scientists at SLAC LCLS including David Reis and Mariano Trigo, Matthias Rossle and Matias Bargheer at BESSY II in Helmholtz-Zentrum Berlin, Thomas Maroutian and Pascal Ruello from Le Mans Université, MIT MTL lab staff members for training and guiding me for fabrications, Li Miao for all the administrative magic, and many other collaborators.

The journey at MIT was full of excitement and joy of new discoveries, but I also had to learn life the hard way at times. I would not have been able to overcome the catastrophes that I faced so easily, if I did not have my friends. I have known Joseph Yoon from college, but I am glad that we joined the same lab and shared the entire experience at MIT together. He has been the best colleague and friend I could ask for. When I was going through rough patches many friends stood beside me and helped me to get right back on my feet. You know who you are and I have to thank you. I also need to thank Pastor Kim and many friends at the First Korean Church at Cambridge for the endless prayers and supports.

Last but not least, I would like to express my sincerest gratitude for You-min Lee and my family. You-min was the brightest star day and night pouring out endless encouragements and constant support, even when I was in the most vulnerable state. It is a true blessing to have Uncle Chris, Aunt Susan, and Cousin Valerie in my life. I am grateful for the prayers and love from my grandparents. I am grateful for my sister and best friend, Hyunjin Shin. My parents, Kyoung-Young Woo and Sung-Kyun Shin, sacrificed so much for my and my sister's well-being. Thank you for the unpayable love you have poured over me.

Hyun Doug Shin

May 10th, 2019

Contents

Chapter 1

Introduction

Imagine walking down a field full of golf balls as fast as possible without falling. Now imagine walking down the same field full of soccer balls, exercise balls, or car-sized bumper balls. Travel paths, speeds, and overall interaction with the balls to get through the field will dramatically change depending on the characteristic size of the balls. Next, imagine walking across the same field with sand-grain-sized or stadium-sized balls. The presence of the objects would not affect the journey at all. The characteristic length scale and energy of a person walking down the field and the size and density of particles the person is interacting with will change how long it would take to complete the trip and how much energy is retained in the end. By recording the initial and final states of the person, one should be able to figure out what is in the field.

Spectroscopy is the study of the interaction between matter and energy, usually delivered as electromagnetic waves. When photons encounter material of interest, the electric component of the electromagnetic wave will interact with electrons and excite them. Excitation will induce changes in material properties, which can be measured and interpreted through optical response change. For example, in elastic scattering found in X-ray diffraction, a crystalline sample diffracts the photons with the same wavelength as the incident light. On the other hand, during an inelastic scattering like Raman spectroscopy, the light matter interaction disperses light with a different frequency than the incident wavelength [1].

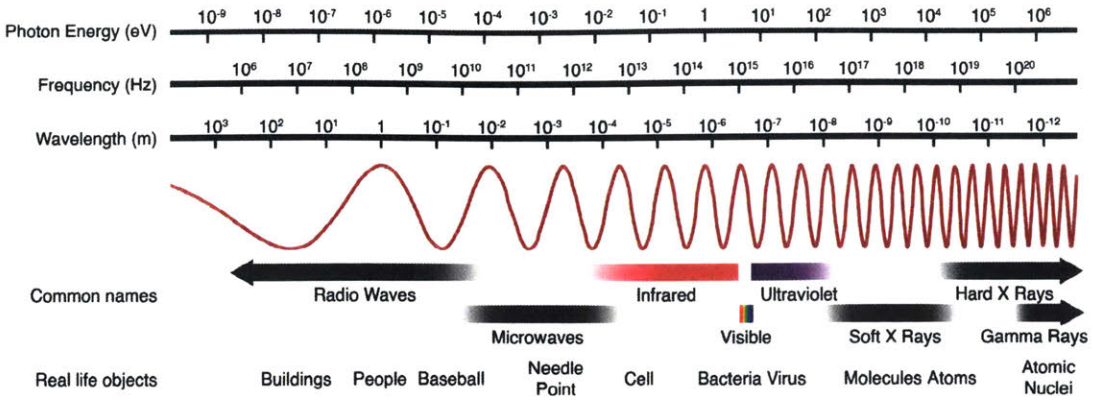

Figure 1-1: Electromagnetic Spectrum. The electromagnetic waves in different frequency ranges have different characteristics, such as generation method, interaction with matter, and practical applications.

Mechanical spectroscopy measures the response to deformation or strain of a material for an applied mechanical stress. When mechanical energy is applied, it can be stored, absorbed, or dissipated depending on the material response. Incident mechanical energy may be stored in an elastic solid, whereas it will be absorbed and dissipated in a viscous material. In a viscoelastic material, which exhibits both viscous and elastic behaviors, the material response will depend on the frequency of strain ω and characteristic relaxation time τ. When high-frequency stress is applied to a viscoelastic liquid, such that $\omega\tau \gg 1$, the material will behave like an elastic solid and store then release the energy. If the stress has low frequency, such that $\omega\tau \ll 1$, the material will exhibit viscous flow and the energy will be absorbed and dissipated. The ratio between applied mechanical stress and the resulting strain, called compliance J, can quantify how much energy is stored. Its inverse, modulus M, can also be used [2].

There are two main approaches for generation and detection of high-frequency acoustic waves. One approach is to apply alternating electrical currents to a transducer that produces mechanical motion. This technique can easily be spotted in everyday objects like speakers, sonars, and ultrasound imaging devices. While these tools are indispensable in day to day life, the upper frequency is limited by the speed of electronic transistors or mechanical responses, limiting the sound range to about

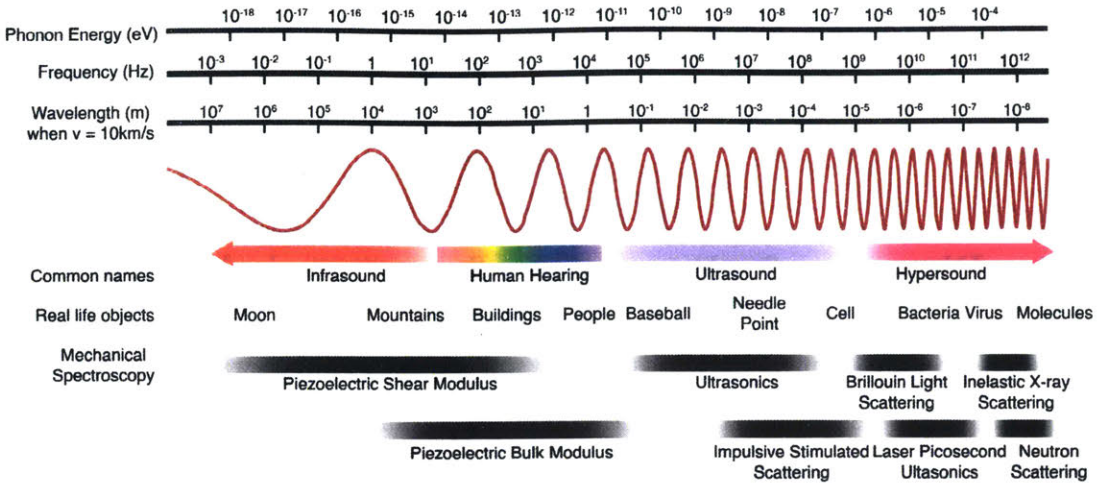

Figure 1-2: Acoustic spectrum. The wavelength shown in based on a speed of sound in a crystalline solid of 10,000 m/s, and the wavelength changes along with speed of sound in the material of interest. Mechanical spectroscopic tools used for viscoelastic materials at different frequencies are listed [3–10].

mHz to GHz ranges. Another method is photoacoustic transduction using ultrafast lasers with picosecond or femtosecond pulse lengths. When a pulse irradiates a material and excites electronic or vibrational modes, mechanical stress can form. The resulting strain response can be measured using another optical pulse. Photoacoustic techniques are capable of generating and detecting acoustic waves at frequencies ranging from MHz to THz. Acoustic waves at this frequency range can be valuable for studying thermal diffusion, phonon propagation, and mechanical responses in a wide array of systems.

In Figure 1-2, mechanical spectroscopic techniques for different frequency regimes are shown. In the infrasound to hearing range (mHz to 20kHz), piezoelectric shear modulus gauge and piezoelectric bulk modulus gauge methods can measure low-frequency shear and bulk complex moduli [3, 4]. For ultrasound (20 kHz to 1 GHz), ultrasonics and impulsive stimulated scattering can measure longitudinal and shear sound speeds and attenuation rates from which complex moduli can be determined. Brillouin light scattering, laser picosecond ultrasonics, inelastic X-ray scattering, and neutron scattering provide information in the hypersound ($>$ 1 GHz) regime. Developing tabletop mechanical spectroscopy in hundreds of GHz to THz range can be

uniquely valuable as will be discussed in the next sections. The goal of this thesis is to further develop non-contact and non-destructive photoacoustic methods to extend the frequency range of mechanical spectroscopy.

1.1 Picosecond ultrasonics of supercooled liquids

Glassy solids are formed by bypassing crystal nucleation upon rapid cooling into a metastable state. Understanding the glass transition has many scientific and industrial applications ranging from polymer processing to storing biomolecules [11]. It would be valuable to have new probing techniques to test the validity of the mode coupling theory, which is the only model of viscoelasticity derived from a first-principles microscopic description of the liquid.

Acoustic spectroscopy can directly probe density fluctuations through speed of sound and attenuation measurements and provide insights to dynamical and structural characteristics. There are other probing methods such as dielectric susceptibility measurements that span 18 decades of frequencies. However, coupling between the dielectric constant and structural relaxation dynamics is complicated, in part because the coupling is temperature-dependent [12]. Light scattering spectra spanning 16 decades of frequency have also been collected, but it is even more complicated to couple polarizability to viscosity [13]. Therefore, mechanical susceptibility spectra ranging from mHz to GHz, relevant frequencies for relaxation of supercooled liquids, can be uniquely valuable, especially if the acoustic frequencies from hundreds of GHz to a few THz can be reached.

When a glass-forming liquid is cooled down, it can be supercooled, avoiding crystallization below the melting point and behaving like a liquid with increasing viscosity and relaxation time until the glass transition temperature, T_g, is reached. T_g is defined as the point in temperature where the viscosity of the liquid reaches 10^{13} poise (1 poise = 0.1 Pa·s), or the relaxation time (τ) reaches 100 seconds [11, 14]. Unlike relaxation in normal liquids, which follows a single or near-single exponential decay, there are two distinct relaxation mechanisms on different time scales for supercooled

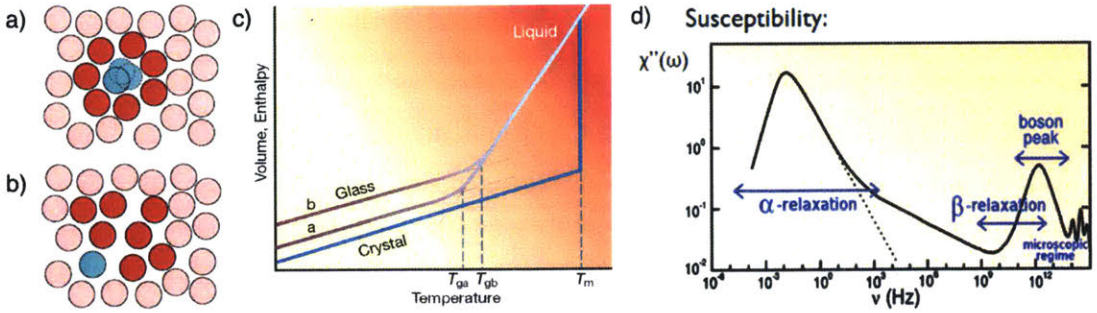

Figure 1-3: (a) Temperature-independent beta relaxation, also known as "cage rattling" on ps timescales. (b) Temperature-dependent alpha relaxation on ps to ks timescales. The molecule of interest (represented with a turquoise circle) surrounded by neighboring molecules (in red) shows localized movement in short time scale (a) or escapes its cage and has different neighbors in long time scale (b). (c) Schematic illustration showing temperature and enthalpy behavior of liquids at temperatures around T_g. (d) Schematic representation of the frequency dependence of the susceptibility. Figure adapted from [14]

liquids, as depicted in figure 1-3 a) and b) [15]. The first is a temperature-independent relaxation process called β-relaxation, which corresponds to locally isolated motions within the cages formed by neighboring molecules. The second relaxation process is a temperature dependent process called α-relaxation, which involves collective rearrangements of cages [16]. This process is highly non-exponential, typically covering several decades of time scales.

The mode coupling theory (MCT) describes the dynamics of the density response of a liquid through the time-dependent density correlator,$\phi_q(t) = \frac{<\rho_q^r(t)^*\rho_q^r(0)>}{<|\rho_q^r(0)|^2>}$, and the corresponding complex susceptibility $\chi''(t)$ that describes elastic compressibility, which are in a Fourier transform relationship [17]. As shown in Figure 1-4, idealized MCT predicts that the density correlator does not decay to zero after a liquid is cooled below the critical temperature T_c, but converges at long times to a limit, $\lim_{t\to\infty} \phi_q = f_q^c$, which is called the non-ergodicity parameter or Debye-Waller factor [18]. Because the idealized MCT includes only density fluctuations, an unphysical prediction is made that the system stays out of equilibrium for an indefinite time frame even well above the glass transition temperature. Extended MCT includes thermally assisted "hopping" terms, which are speculated as arising from coupling

between the density and transverse current modes. As is shown in 1-4 (c) and (d), a plateau region between fast and slow relaxation shows the effective non-ergodicity or Debye-Waller factor whose value can still be defined, yet the density fluctuations relax to zero (the liquid returns to equilibrium) at long times [19]. Note that Tc is considerably higher than Tg, below which the system might be considered truly non-ergodic.

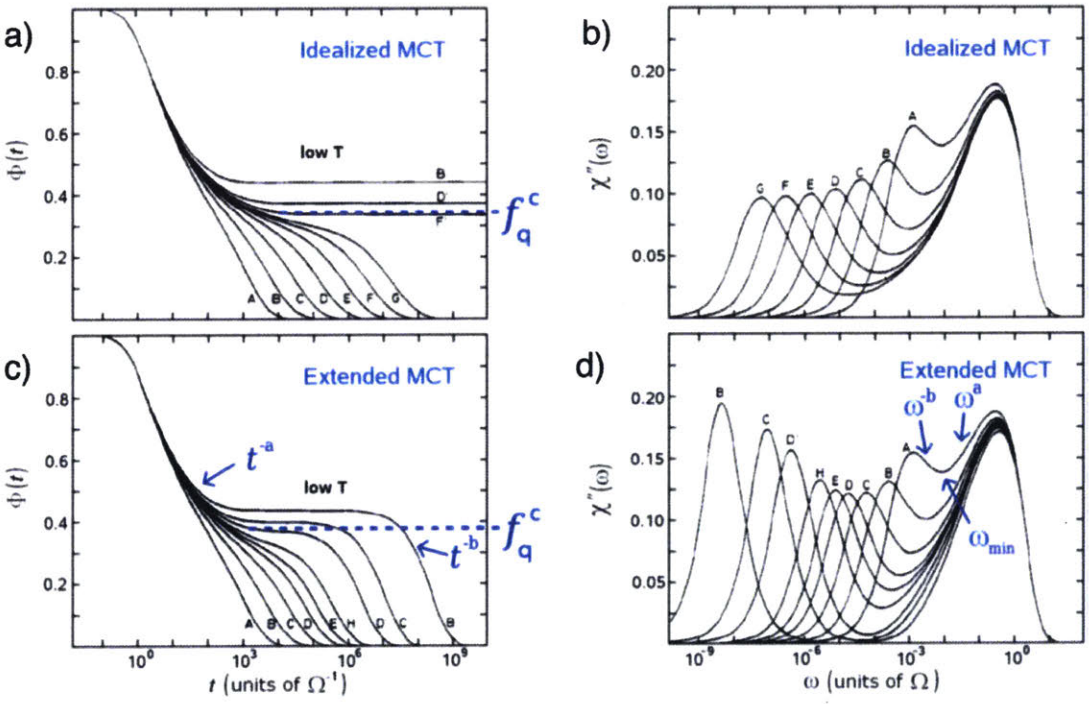

Figure 1-4: Mode-coupling theory predictions of the density correlator $\phi(t)$ and the susceptibility $\chi''(\omega)$ as a function of time and frequency at different temperatures. (a) and (b) show the results for the idealized mode coupling theory; below a critical temperature the density correlator does not decay to zero, indicating that the α-relaxation never occurs. (c) and (d) show the results of extended mode coupling theory, which includes "hopping" terms, the origins of which are under debate. This term, speculated to come from density and transverse current fluctuation, provides some insight into why T_g is generally lower than the critical temperature T_c. Figure adapted from [20]

The Debye-Waller factor is expressed in MCT as

$$f_q(T) = \begin{cases} f_q^c + h_q\sqrt{(T_c - T)/T_c}\, for\ T < T_c \\ f_q^c \qquad\qquad\qquad\qquad for\ T > T_c \end{cases} \tag{1.1}$$

where f_q^c is the Debye-Waller factor at the critical temperature and h_q is a critical amplitude. When the wave vector q approaches zero, the Debye-Waller factor can be expressed with constants measurable with acoustic spectroscopy: $\lim_{q\to 0} f_q^c = 1 - \left(\frac{c_0(T)}{c_\infty(T)}\right)^2$, where c_0 is the longitudinal zero-frequency speed of sound and c_∞ is the instantaneous (high-frequency limiting) speed of sound. Picosecond ultrasonics was applied to measure the instantaneous speed of sound at various temperatures, permitting determination of the Debye-Waller factor and testing of the square-root cusp temperature dependence predicted by MCT. The fast β-relaxation dynamics approaching the plateau region and the slow (α) relaxation dynamics leading away from it, observed in the time-domain plots in Figure 1-4 (c), lead in the frequency-domain susceptibility spectra (Figure 1-4 (d)) to the local minimum of the susceptibility $\chi''(t)$ between the α- and β-relaxation peaks and the surrounding regions of the spectrum, described in MCT by:

$$\chi''_{min}(\omega_{min}) \propto \sqrt{T - T_c}\ and\ \omega_{min} \propto \left(\sqrt{T - T_c}\right)^a \tag{1.2}$$

$$\frac{\chi''}{\chi''_{min}} = [a\left(\frac{\omega}{\omega_{min}}\right)^{-b} + b\left(\frac{\omega}{\omega_{min}}\right)^{a}]/(a+b), \tag{1.3}$$

where a ($0 < a < 0.5$) and b ($0 < b < 1$) are critical exponents. The susceptibility shows a ω^{-b} dependence for high-frequency side of α peak and a ω^a dependence for low frequency side of β peak. MCT predicts a quantitative relationship between the α- and β-relaxation peaks through the exponent parameter λ:

$$\lambda = \frac{\Gamma^2(1-a)}{\Gamma(1-2a)} = \frac{\Gamma^2(1+b)}{\Gamma(1+2b)}, \tag{1.4}$$

where Γ is the standard Γ function. In other words, a quantitative and testable relation between the α- and β-relaxation dynamics is predicted [19, 20]. There has

been an active collaborative effort to acquire ultra-broadband mechanical spectra with seven different experimental techniques covering 13 decades of frequency ranging from mHz to hundreds of GHz. As shown in Figure 1-5, the temperature-dependent relaxation dynamics have been collected with collaborators in Denmark (mHz to kHz range) and at MIT (MHz to GHz range) [21, 22].

It is impossible to conclusively test mode coupling theory without access to the high-frequency (β relaxation) response since that is needed for one of the critical exponents. In particular, the attenuation rates of high-frequency acoustic modes must be measured. Therefore, extending the frequency range above the limit of 400 GHz (100 GHz is rarely exceeded) is crucial for understanding the dynamical parameters of β-relaxation.

1.2 Investigation of thermal transport

Another application of the work in this thesis is the study of heat transport. In the early 17th century, heat flux was observed to be proportional to the temperature gradient over a macroscopic distance:

$$\mathbf{q} = -k\Delta T, \tag{1.5}$$

where $\mathbf{q}$ is the heat flux, k is the thermal conductivity, and ΔT is the temperature gradient. In his theory, Joseph Fourier theorized that heat carriers move diffusively such that:

$$\frac{\delta T}{\delta t} = \alpha \Delta^2 T, \tag{1.6}$$

where $\alpha = k/\rho c$ is the thermal diffusivity with ρ the density of medium and c the specific heat at constant pressure [23]. The average distance heat carriers travel before scattering is much shorter than the length scale of the thermal profile in diffusion.

Heat transport in semiconductors and insulators is dominated by acoustic phonons in the hundreds of GHz to few THz range. Phonons are normal modes of collective lattice vibrations in a periodic crystal. Like photons, phonons are quasi-particles that

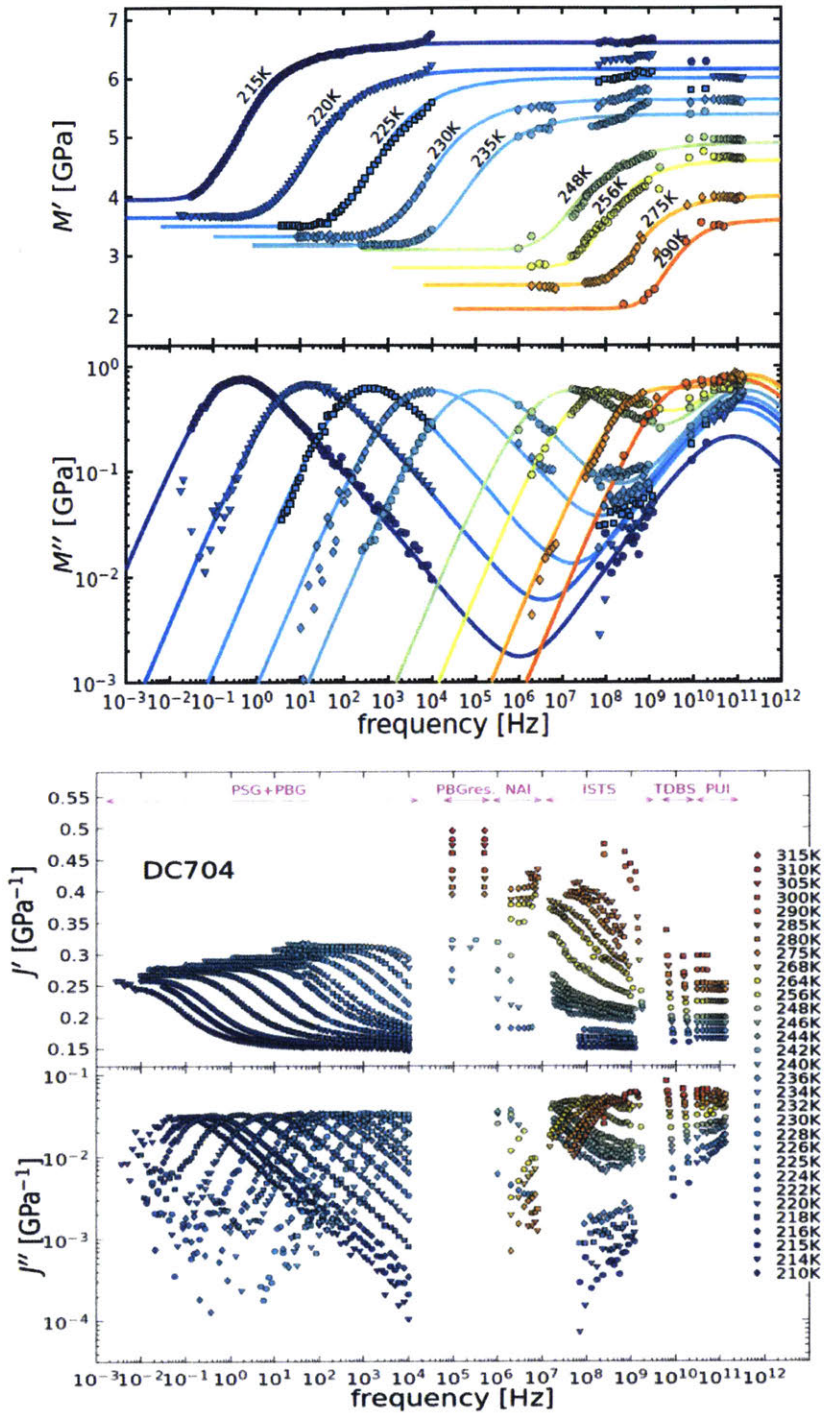

Figure 1-5: Ultra-broadband mechanical spectra of supercooled DC704. (a) Real and imaginary parts of longitudinal moduli (b) Real and imaginary elastic compliance spectra. Figure adapted from [22].

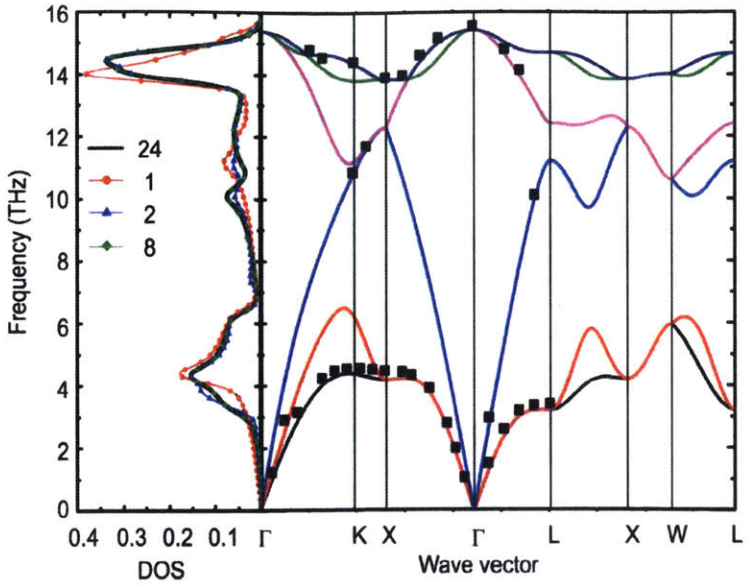

Figure 1-6: Phonon dispersion curve of bulk silicon. Black dots indicate experimental results from Nilsson and Nelin from 1972 [24]. On the left side, densities of states are shown for thin films of varying thickness with numbers in the label indicating number of unit cells. Figure adapted from [25].

exhibit both wave and particle like behaviors, well described in most cases by a classical wave equation with frequency ω, wavevector $\mathbf{q}$, and direction of particle motion (e.g. loongitudinal or transverse polarization) relative to the propagation direction. In longitudinal acoustic waves, material oscillations are parallel to the propagation direction, and in transverse or shear waves the oscillations are perpendicular to the propagation direction. The relationship between ω and $\mathbf{q}$ is called the dispersion relation, and the slope of the dispersion curve, $d\omega/d\mathbf{q}$ is the group velocity for each acoustic mode.

The mean free paths of heat-carrying phonons in the hundreds of GHz to few THz range are expected to be short, but the high density of states makes them relevant to heat transport. The thermal conductivity κ of a material can be modeled microscopically through the relation,

$$\kappa = \frac{1}{3}\int_0^{\omega_{max}} C_\omega v \Lambda(\omega) d\omega, \tag{1.7}$$

where C_ω is the heat capacity of phonons at frequency ω, v is the speed of sound, and $\Lambda(\omega)$ is the strongly frequency-dependent phonon mean free path whose values in the crucial frequency range have eluded direct measurement. If we could determine the frequency-dependent mean free paths $\Lambda(\omega)$, we would be able to calculate thermal conductivities based on direct experimental measurements of the underlying microscopic parameters.

Phonons are bosons that have population numbers across different modes that will follow the Bose-Einstein distribution. Heat capacity, a measure of relative energy contribution of phonon at given frequencies, will depend on the density of states, $\mathbf{q}(\omega)^2/(2\pi^2 v(\omega))$. The heat capacity in a given material is:

$$C(\omega) = \hbar\omega g(\omega)\frac{\delta n(\omega, T)}{\delta T}, \tag{1.8}$$

where $g(\omega)$ is the density of states and $n(\omega, T)$ is the phonon occupation number [26].

When phonons are populated, they are expected to interact with other phonons, electrons, impurities in the lattice, defects, grain boundaries, and interfaces. At given temperatures, different interactions will affect different parts of phonon spectrum and thereby influence the thermal conductivity [27]. Phonon scattering by atomic-sclae defects and impurities is proportional to ω^4 as in Rayleigh scattering of light. Typically, electron-phonon scattering results in a small change in the intrinsic scattering rate in semiconductors [28], leaving phonon-phonon interactions as the main influence on phonon mean free path in high-quality single crystals. In Chapter 5, the carrier effects on phonon scattering and thermal conductivity will be discussed in a silicon membrane with high carrier density.

There has been success in recent years in calculating mean free paths through molecular dynamics and first-principles calculations [29–31]. These studies showed that about 50 percent of thermal conductivity can be attributed to phonons with $\geq 1\mu m$ mean free path at room temperature [31]. The density of states of phonons is concentrated in the higher frequency phonons with short wavelengths, so these findings were striking. Non-diffusive thermal transport has been observed as heat

carriers propagated ballistically for phonons with long wavelengths [32]. Studying the mean free paths of heat-carrying phonons in the hundreds of GHz to a few THz range can be a valuable asset to understanding of heat transport in semiconductors.

1.3 Overview

To address the need for broadband mechanical spectroscopy, femtosecond laser pulses were used to generate and detect acoustic waves. In this thesis, experimental generation and detection schemes to expand the accessible acoustic phonon frequency bandwidth and range are discussed. To photo-excite acoustic waves, different types of transducers were used such as a thin metal film, a strongly magnetostrictive material, and strained piezoelectric superlattices. Acoustic wave detection methods included monitoring of optical transmittance/reflectance, polarization, and diffraction over time.

In Chapter 2, general concepts and experimental methods of optical generation and detection of acoustic phonons will be presented. An introduction to strain and stress will be presented to address propagation of elastic waves in condensed matter. Common experimental methods such as the picosecond ultrasonics with the time-domain Brillouin scattering detection and a four-wave-mixing transient grating experiment will be introduced. After an introduction to common methods to study acoustic phonons, temperature dependent measurement instrumentation will be discussed.

Chapter 3 introduces generation and detection of acoustic phonons in the magnetostrictive material FeGa (galfenol). Acoustic phonon generation through laser-induced demagnetostriction and detection through magneto-optical Kerr effect will be discussed. Using a magnetostrictive material as a transducer can produce not only a longitudinal wave but also a shear wave. Gigahertz longitudinal and shear acoustic waves were excited by releasing magnetoelastic strain in FeGa. Acoustic phonons generated either through transient demagnetostriction or acoustic mode conversion can have several hundreds of GHz frequencies matching the demagnetization timescale.

Chapter 4 discusses piezoelectric generation and detection of acoustic phonons in the THz regime. Strained piezoelectric semiconductor superlattices with different numbers of periods, roughness, and sample structures were studied to measure acoustic phonon mean free paths in layered structures and in a semiconductor spacer. Using an InGaN/GaN superlattice, the lifetime and bandwidth measurement of THz phonons was shown to be a noninvasive and sensitive tool to test the layered structure quality, applicable for semiconductor industries. Additionally, the lifetime of THz phonons in GaN was measured by placing a GaN spacer between two superlattices. This was the first direct measurement of THz-frequency phonon propagation lengths in a bulk material.

In Chapter 5, thermal conductivity changes due to carrier-phonon interactions will be discussed. Phonon contributions are critical in heat transport in semiconductors and insulators. Previously, theoretical studies have shown that the lattice thermal conductivity can be reduced by electron-phonon interactions when the carrier concentration is above 10^{19} cm^{-3}. To isolate the carrier contributions to the scattering events, photoexcited carriers were generated in silicon through pulsed laser excitation. To measure thermal conductivity changes, time-domain thermoreflectance and transient thermal grating techniques were employed with a carefully timed additional excitation for carrier generation.

Chapter 2

Photoacoustic Spectroscopy

Acoustics, or the study of sound, involves measurement of vibrations varying in time in a material, sometimes through hearing as well as other measurement methods. The first person to approach sound propagation mathematically was Sir Isaac Newton. He treated sound as pressure pulses through a fluid medium [33]. From the early 1960s, a variety of photo-acoustic spectroscopic techniques have been developed and applied to study microscopic structures, glass transitions, and thermal conductivity in condensed matter [34]. Especially with development of titanium-sapphire lasers, picosecond ultrasonics emerged using subpicosecond laser pulses to generate and detect sound waves at ultrafast time scales in the 1980s [35–37]. There are many spectroscopic tools for structural and mechanical properties like scanning probe microscopy, atomic force microscopy, surface force apparatus, nonlinear optical spectroscopy, infrared and THz spectroscopy, sum-frequency vibrational spectroscopy, scanning tunneling microscopy, neutron-scattering, and x-ray diffraction [38–47]. However, picosecond laser ultrasonics provides unique values as a non-destructive, non-contact spectroscopy that measures mechanical responses directly.

In this chapter, picosecond laser ultrasonics will be introduced. An overview of strain and stress will be presented to understand propagation of elastic waves in condensed matter. Next, optical generation and detection of acoustic waves will be discussed. Finally, experimental techniques and setups used in the experiments for subsequent chapters will be presented.

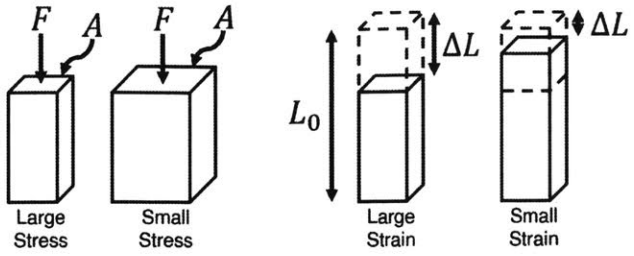

Figure 2-1: Stress and strain in a single dimension. Stress is generated when force is applied (Stress = Force/Area), and the resulting deformation compared to the initial shape is the strain (Strain = $\Delta L/L_0$).

2.1 Stress and strain

Before discussing the generation and detection of propagating elastic waves, characteristics of stress and strain need to be addressed. When force is applied, a material of interest undergoes a deformation. Stress is a physical quantity expressing internal forces that neighboring particles exert on each other found by force over area. Strain is a measure of deformation found by deformation over initial shape. The deformation is elastic, if the body returns to its original form after the external forces are removed. Ideal elastic behaviors can be characterized by an linear response to an applied stress and an equilibrium position to which system recovers [48].

The following description is based on reference [49]. When a particle is located at $\mathbf{r}$ and displaced to $\mathbf{r}'$, the time-dependent displacement vector field $\mathbf{u}$ can be defined as,

$$\mathbf{u}(\mathbf{r},t) = \mathbf{r}'(\mathbf{r},t) - \mathbf{r}. \tag{2.1}$$

The term material deformation implies that particles in a medium are displaced relative to each other. Rigid translations and rotations do not have relative change between particle distances in the lattice, so they are out of consideration. By taking a differential form of equation 2.1,

$$d\mathbf{u}(\mathbf{r},t) = d\mathbf{r}' - d\mathbf{r} = \frac{\partial \mathbf{u}}{\partial x}dx + \frac{\partial \mathbf{u}}{\partial y}dy + \frac{\partial \mathbf{u}}{\partial z}dz = \Sigma_{ij}\frac{\partial u_i}{\partial x_j}dx_j\mathbf{u_i}, \tag{2.2}$$

where $\mathbf{u}(\mathbf{r},t) = \mathbf{x}u_x(\mathbf{r},t) + \mathbf{y}u_y(\mathbf{r},t) + \mathbf{z}u_z(\mathbf{r},t)$ and $\{i,j\} \in$ [1,2,3] $\Leftrightarrow$ [x,y,z]. In

a matrix form, equation 2.2 can be expressed with displacement gradient matrix, $\xi(\mathbf{r}, t_0)$ by,

$$\begin{pmatrix} du_1 \\ du_2 \\ du_3 \end{pmatrix} = \underbrace{\begin{pmatrix} \frac{\partial u_1}{\partial x} & \frac{\partial u_1}{\partial y} & \frac{\partial u_1}{\partial z} \\ \frac{\partial u_2}{\partial x} & \frac{\partial u_2}{\partial y} & \frac{\partial u_2}{\partial z} \\ \frac{\partial u_3}{\partial x} & \frac{\partial u_3}{\partial y} & \frac{\partial u_3}{\partial z} \end{pmatrix}}_{\xi(\mathbf{r},t_0)} \begin{pmatrix} dx \\ dy \\ dz \end{pmatrix}$$

For a rigid translation, $\mathbf{u}(\mathbf{r}, t)$ and $\mathbf{u}(\mathbf{r} + d\mathbf{r}, t)$ are equal and the differential displacement $d\mathbf{u}$ is zero. To show that the rigid rotation does not apply deformation, let us define a measure of deformation ς as,

$$\varsigma = dr'^2 - dr^2. \tag{2.3}$$

Then using equation 2.2, dr'^2 in terms of dr^2 becomes,

$$dr'^2 = \sum_i dx_i'^2 = \sum_i (dx_i + du_i)^2 = \sum_i dx_i^2 + \sum_i du_i du_i + 2\sum_i du_i dx_i \tag{2.4}$$

$$= dr^2 + \sum_{ijk} \frac{\partial u_k}{\partial x_j}\frac{\partial u_k}{\partial x_i} dx_j dx_i + \sum_{ij} (\frac{\partial u_i}{\partial x_j} + \frac{\partial u_j}{\partial x_i}) dx_i dx_j \tag{2.5}$$

$$= dr^2 + \sum_{ij} (\frac{\partial u_i}{\partial x_j} + \frac{\partial u_j}{\partial x_i} + \sum_k \frac{\partial u_k}{\partial x_j}\frac{\partial u_k}{\partial x_i}) dx_i dx_j \tag{2.6}$$

For a small deformation, such that $\frac{\partial u_k}{\partial x_i} \ll 1$, the quadratic terms become negligible, leaving the measure of deformation to be,

$$\varsigma = \sum_{ij} 2\eta_{ij} dx_i dx_j, \tag{2.7}$$

where

$$\eta_{ij} = \frac{1}{2}(\sum_{ij} (\frac{\partial u_i}{\partial x_j} + \frac{\partial u_j}{\partial x_i}). \tag{2.8}$$

A symmetric and dimensionless η_{ij} is a component of the strain tensor for small deformations, where η_{ii} show simple expansion or compression in a given direction (longitudinal strain), while η_{ij} with $i \neq j$ represent shear strain. For a force acting

on a small volume, the total force can be expressed by $\int \mathbf{F}(\mathbf{r})dV$, where $\mathbf{F}(\mathbf{r})$ is the force per unit volume or force density with components F_i. Through the divergence theorem, the force density component F_i is a divergence of a second rank tensor $F_i \equiv \sum_i \frac{\partial \sigma_{ij}}{\partial x_j}$ such that,

$$\int \mathbf{F}(\mathbf{r})dV = \sum_i \frac{\partial \sigma_{ij}}{\partial x_j} = \sum_i \oint \sigma_{ij} ds_j, \tag{2.9}$$

where ds_j is the surface element of small volume element. The tensor σ_{ij} is called the stress tensor with units of force per unit area (Pa or J/m^3). The stress tensor is related to strain tensor by,

$$\sigma_{ij} = \sum_{kl} c_{ijkl}\eta_{kl}. \tag{2.10}$$

From above relationship and equation 2.8,

$$\sigma_{ij} = \frac{1}{2}\sum_{kl} c_{ijkl}\left(\frac{\partial u_k}{\partial x_l} + \frac{\partial u_l}{\partial x_k}\right) = \sum_{kl} c_{ijkl}\frac{\partial u_k}{\partial x_l}. \tag{2.11}$$

Due to symmetry of the strain and stress tensors, the 81 component elastic tensor can be reduced to 21 components. The components can be contracted through Voigt notation as $c_{ijkl} = c_{\alpha\beta}$, where $\alpha = (ij)$ and $\beta = (kl)$ [50]. Then the notations become, $(11) \leftrightarrow 1, (22) \leftrightarrow 2, (33) \leftrightarrow 3, (23) = (32) \leftrightarrow 4, (13) = (31) \leftrightarrow 5$, and $(12) = (21) \leftrightarrow 6$.

There are three specific types of uniform stress and deformation for which stress and strain tensors can be simplified. For uniform linear or longitudinal dimension, Young's modulus, $M = stress/strain = \frac{F/A}{\Delta L/L_0}$, can capture expansion or compression. The larger the Young's modulus, the stiffer the material. For example, glass, brass, and steel have Young's moduli of 6.0, 9.0, and 20 N/m^2. Shear modulus, $G = \frac{F/A}{\Delta x/R}$, applies when a force is applied to create a transverse deformation, where Δx is maximum distortion in x direction and R is the height of unit cell of distortion. Bulk modulus, $K = \frac{F/A}{-\Delta V/V_0}$, is inverse of compressibility that is applicable when equal

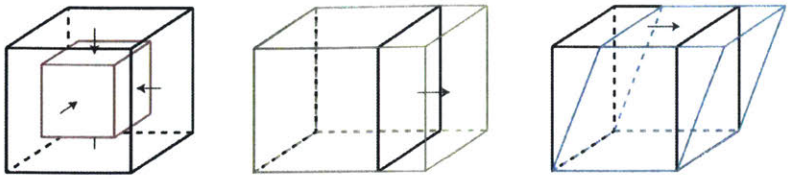

Figure 2-2: Illustration of moduli. Black and colored lines indicate the shapes before and after a perturbation. Bulk compression modulus, K, applies when equal forces are applied to all faces of an element. Bulk longitudinal modulus, M, applies when stress and strain are limited to one dimensional expansion or compression. Simple shear modulus (G) applies when a force is applied to create a transverse deformation.

forces are applied to all faces of an element. These moduli are related by:

$$K = M - \frac{4}{3}G. \tag{2.12}$$

The photoacoustic techniques described in this thesis will mainly focus on the measurement of the longitudinal stress and deformation. The modulus M or its inverse, compliance J, give the ratio between an applied mechanical stress and the resulting strain. For a step function stress applied at time-zero, the relationship can be simplified as [2]:

$$\sigma(t) = \eta(t)M(t) \tag{2.13}$$

$$\eta(t) = \sigma(t)J(t), \tag{2.14}$$

where $\eta(t)$ is the time dependent strain and $\sigma(t)$ is the stress.

2.2 Pump-probe spectroscopy

To capture phenomena that occur faster than eyes can discern, stop-motion photography was adopted in late 1800s. In 1872, Eadweard Muybridge captured images of a horse running on a track. At the time, it was a mystery whether a horse's hooves were completely off the ground at a point in time during its run or at least one of them was always in contact with the ground. To show the fast dynamics that could

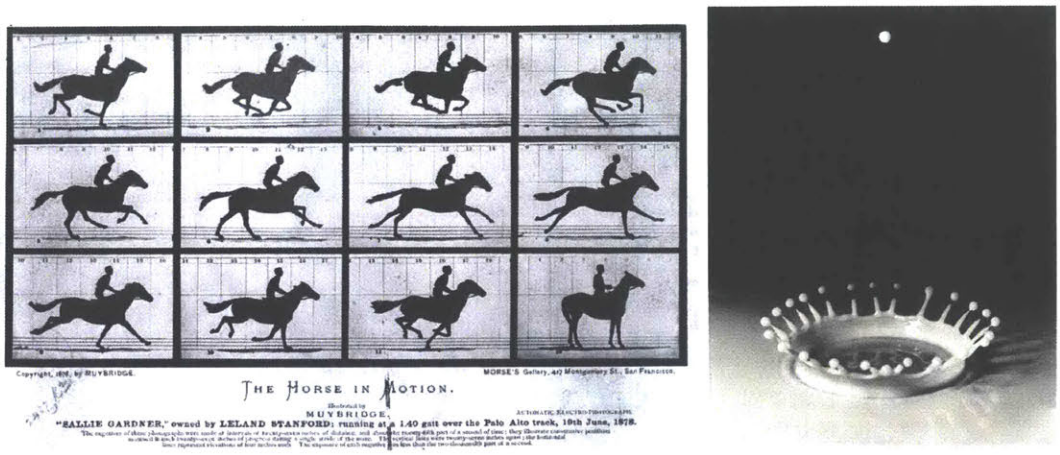

Figure 2-3: Picture on the left: Sallie Gardner at a Gallop, also known as the Horse in Motion, by Eadweard Muybridge is one of the first motion pictures (1878). Twelve cameras were installed and set up to be triggered by wires as a horse ran on the track (Picture from [51]). Picture on the right: Milk-Drop Coronet Splash by Harold Edgerton was taken by stop motion photography using strobe lights (1936) (Picture from [52])

not be observed with naked eyes, Muybridge installed 12 cameras that were triggered by wires on the track. As the horse ran across the track, the wires were broken taking pictures at an interval. By putting the pictures together, Muybridge could show how horses ran. Another common way to capture fast dynamics in a frozen frame was stroboscopes. A former MIT professor Harold Edgerton took a famous Milk Drop Coronet picture in 1936 using high-tech strobe lights. Drops of milk were made, and they fell to a liquid surface below. Circuits were designed to make burst of lights at a given frequency. By varying the timing between flashing lights and the milk droplets, Edgerton could capture a millisecond phenomenon imperceptible to the naked eyes with a camera and show how milk drop coronets were forming [51, 52].

Similar to stop-motion photography or stroboscopy, pump-probe laser techniques make use of timed and designed events to study ultrafast phenomena. Laser-based pump-probe techniques can capture ultrafast processes and dynamics on the time scales inaccessible by conventional electronics down to femtoseconds, or 10^{-15} s. Using an optical pulse called a pump, an ultrashort stimulus triggers a dynamic change in a system of interest. Then a weaker optical pulse called a probe is introduced to

capture the state of the system at a given moment. As long as the perturbation is infinitesimally small, the thermodynamic system responds to an external perturbation linearly, providing valuable insight into the system at equilibrium through fluctuation dissipation theorem. To ensure that the dynamic process is weak enough to not to change intermolecular interactions, the linearity of material responses need to be monitored.

2.3 Picosecond ultrasonics pump-probe setup

The experiments presented in this thesis were performed with a system built around a Coherent Verdi G-18 (18 W, 532 nm, CW) pump laser unless noted otherwise. The 16W of pump laser power was used to feed an oscillator and an amplifier. About six watts of laser power were used in a Coherent Mira-900 mode-locked Ti:sapphire oscillator to generate about 790 nm beam with 150 fs full width at half maximum (FWHM) pulse width at a repetition rate of 80 MHz with a pulse energy of 6 nJ. The other 10 watts of power and the Mira output were used to pump a Coherent RegA-9000 regenerative amplifier (RegA) with 1 W output with 200 fs FWHM pulse width at a repetition rate of 250 kHz with about 4 μJ. Shorter pulse durations are not necessarily beneficial in most photoacoustic experiments, because shorter pump beams could damage transducer films used for acoustic generation more easily. When higher energy per photon was needed either for pump or probe, the beam was frequency doubled through second harmonic generation in a nonlinear birefringent $\beta - BaB_2O_4$ (BBO) crystal.

The 790nm beam out of the RegA was split into two beams with unequal intensity using a plate beam splitter. The more intense beam was used as an optical pump to generate acoustic waves, carriers, and thermal excitation. To enhance the signal, an acousto-optic modulator (AOM) was placed in the pump arm and the pump beam was chopped by suppression at a defined frequency. By chopping the pumping frequency, steady state heating is reduced while pulse energy can be increased at the same power level. The AOM driver voltage could be tuned continuously between 0V and 5V, which

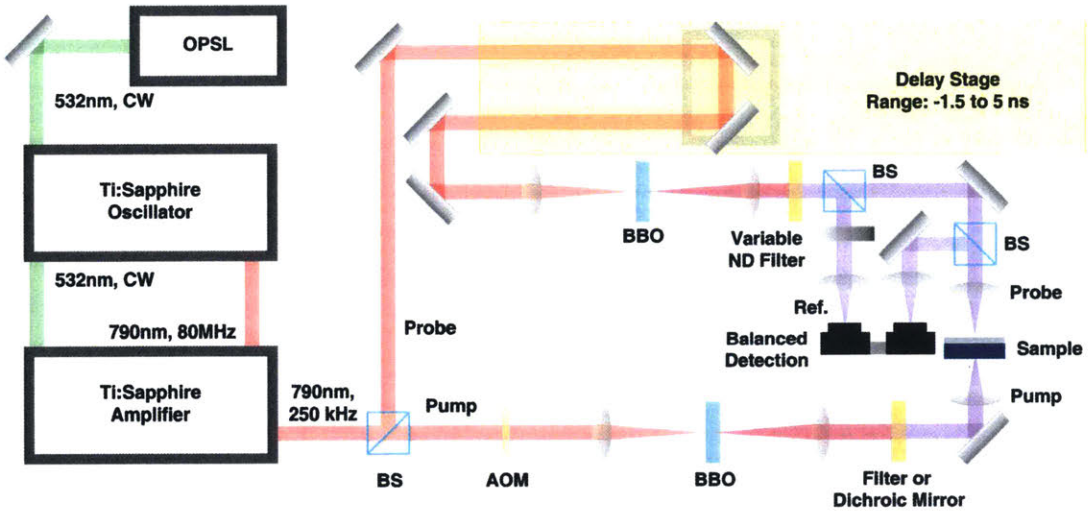

Figure 2-4: Schematic illustratioin of pump-probe setup. The beam out of the RegA amplifier is split into pump and probe, and the probe beam is time delayed using a mechanical delay stage. Detection is modulated by an acousto-optic modulator in the pump path and the probe beam is measured using a balanced detector.

changed the diffraction efficiency and adjusted pump power. Through a series of tests, modulation frequency of 41.7 kHz was found ideal for optimizing signal to noise ratio. TGP110 10MHz Pulse Generator made by Thurlby Thandar Instruments was used to set the AOM driver modulation frequency by applying square wave pulses. The detection frequency was synced with the pumping frequency, and Stanford Research Systems SRS 844 Lock-in amplifier was used for signal detection. The lock-in amplifier was needed due to small signal-to-noise levels from acoustic signals on the order of 10^{-5} to 10^{-7}. In the Nelson group, a pulse shaper called "Death Star" has also been used to enhance the signal to noise ratio. By using a multiple recirculation-reflection design and set of delay paths, seven pulses were temporally separated to define an excitation repetition rate between 1 GHz and 1 THz, but detailed explanation of the Death Star pulse shaper is outside the scope of this thesis [53].

The weaker arm out of the RegA was used as an optical probe to monitor the dynamics created by the pump pulse. The probe pulse was time delayed by a 81-inches-long linear air-bearing translation stage from Aerotech Inc., which generated more than 6 ns time delay with less than one micrometer (6.6 fs) resolution. Due to

the long beam path on the delay stage, small misalignment of the retroreflector on the stage could result in walking of the focused probe on the sample away from the pump spot with about 100 μm diameter. To minimize beam divergence and walking, the probe beam diameter was increased using a telescope. A balanced photodetection scheme was employed using two large-area, low-noise silicon-based photodiodes to minimize laser noise and air fluctuations. The probe beam was split into a reference and a probe. After the delay stage, the reference was fed to one of the detectors after passing through a variable neutral density filter for balancing intensity. The probe, which was sent to a sample and contained dynamic information, was fed to the other detector. The two diodes with opposite polarity were balanced to an equal background intensity prior to each measurement by tuning reference and probe intensity. The common output from the connected diodes was fed to the lock-in detector to monitor intensity changes in the probe.

2.4 Picosecond ultrasonics

2.4.1 Photogeneration of acoustic strain

The development of lasers with nanoseconds to attoseconds pulses brought tremendous developments in spectroscopy and imaging from Raman Spectroscopy to NMR to fluorescence spectroscopy to photoactivated localization microscopy [54–57]. For mechanical spectroscopy, the development of ultrafast lasers has enabled access to higher than GHz photoacoustic transduction. The highest frequency phonons that can propagate through a material are given by $v/2a$, where v is the speed of sound and a is the unit cell dimension [58]. For a typical crystal lattice, the highest frequency of sound propagation is around 10 THz, assuming it has lattice constant of $a \approx 5$ and speed of sound of $v \approx 10,000 m/s$. Therefore, photoacoustic techniques have the potential to probe acoustic modes across the Brillouin zone. The acoustic frequency bandwidth is usually limited by the excitation and detection material responses rather than the laser pulse duration of $\tau \approx 100 fs$. For metal transducers, the

frequency generated is determined by the heating profile and depth for through-plane acoustic waves. The range may vary depending on the wavelength of the optical pulse and the type of metal, but the typically excited thickness is on the order of 10 to 100 nm. Using a 10 nm aluminum film and femtosecond 800 nm pulses, up to 440 GHz acoustic frequency was reported [59].

To convert electromagnetic wave energy to acoustic energy, a medium called acousto-optic transducer is used. Electromagnetic waves can excite electronic or vibrational modes in a transducer, leading to mechanical strain through thermal expansion, inverse piezoelectric effect, or inverse magnetostriction. In Chapter 3 and 4, magnetostrictive and piezoelectric conversion will be discussed in more depth, but discussion in this section will mainly focus on photoacoustic generation using thermal expansion in a thin metal film, a more conventional approach.

When ultrafast laser pulses are absorbed by a solid, acoustic waves can be generated through thermal expansion. After electrons in the metal surface absorb photons, they are electronically excited and their population becomes well-defined within the first 500 fs. Then the energy from electrons is transferred to lattice, and the lattice temperature rises causing thermal stress [35, 60]. The thermal stress launches an elastic strain in three dimensions, but this thesis focuses mainly on the plane longitudinal acoustic waves with the highest acoustic frequency that propagates normal to the surface. The excessive thermal energy causes shifts in the equilibrium positions of the atoms and thermal expansion of the lattice. The collective displacements in the lattice are the acoustic phonons, or acoustic waves.

When an ultrashort optical pulse with energy Q focused on area A is absorbed by a metal with reflectivity R and optical skin depth ζ, the total energy deposited per unit volume at depth z is given by [35, 61],

$$W(z) = (1 - R)\frac{Q}{A\zeta}e^{-z/\zeta}. \tag{2.15}$$

The deposited energy results in temperature change ΔT,

$$\Delta T = W(z)/C = (1-R)\frac{Q}{A\zeta C}e^{-z/\zeta}, \tag{2.16}$$

where C is the specific heat per unit volume. In a elastically isotropic medium, the thermal stress $\sigma(z)$ is given by,

$$\sigma(z) = -3K\kappa\Delta T, \tag{2.17}$$

where κ is the thermal expansion coefficient and K is bulk modulus. The thermal expansion tensor κ is related to strain tensor η by [62],

$$\eta_{ij} = \kappa_{ij}\Delta T. \tag{2.18}$$

By combining relationship between the stress tensor and the strain tensor from equation 2.11 and thermal stress from equation 2.17, the stress tensor is given as,

$$\sigma_{ij} = c_{ijkl}\eta_{kl} - 3K\kappa_{ij}\Delta T(z). \tag{2.19}$$

Therefore, along the z direction in an elastically isotropic material, the stress and strain are given by,

$$\sigma_{33}(z) = 3\frac{1-\nu}{1+\nu}K\eta_{33}(z) - 3K\kappa\Delta T(z), \tag{2.20}$$

$$\rho\frac{\partial^2 u_3(z)}{\partial t^2} = \frac{\partial\sigma_{33}(z)}{\partial z}, \text{ and} \tag{2.21}$$

$$\eta_{33} = \frac{\partial u_3(z)}{\partial z}. \tag{2.22}$$

The density of material is denoted by ρ, the Poisson's ratio is given by ν, and the displacement in the z direction is u_3. From the above relationship with an assumption that the initial strain is zero everywhere and stress zero at the surface, the time dependent strain wave is given by,

$$\eta_{33}(z,t) = (1-R)\frac{Q\kappa}{A\zeta C}\frac{1-\nu}{1+\nu}[e^{-z/\zeta}(1 - \frac{1}{2}e^{-vt/\zeta} - \frac{1}{2}e^{-|z-vt|/\zeta}\text{sgn}(z-vt)], \tag{2.23}$$

where v is the speed of sound or longitudinal sound velocity with relationship,

$$v^2 = 3\frac{1-\nu}{1+\nu}\frac{K}{\rho}. \tag{2.24}$$

When the counter propagating strain pulses meet interfaces, they bounce back and forth within the film while getting partially transmitted into the adjacent material. The ratio of transmitted to reflected acoustic wave is dependent on the acoustic impedance of material $Z = \rho v$. For an interface of two materials, the reflectivity r_{12} and the transmittance t_{12} are given by,

$$r_{12} = \frac{Z_2 - Z1}{Z_1 + Z_2}, \ and \tag{2.25}$$

$$t_{12} = 1 - r_{12} = \frac{2Z_2}{Z_1 + Z_2}. \tag{2.26}$$

For a metal free surface, the acoustic wave is entirely reflected from the metal/air interface because of four orders of magnitude impedance differences. For example, the acoustic impedance is 17 $\times 10^6$ $Pa \cdot s/m$ in aluminum and 409 $Pa \cdot s/m$ in air. This results in a bipolar acoustic waveform with exponential tails with smoothed out and elongated peaks due to electron diffusion and heat conduction. For a thin metal film with thickness in the order of 10 to 100 nm, the peak frequency of the pulse can be approximated from $f = 1/\tau$, where $\tau = d/v$ is pulse length approximated from thickness of the film d and speed of sound in the metal v.

Piezoelectric semiconductor superlattices (SLs) exhibit zone-folding of the acoustic branches within the mini-Brillouin zone. The periodicity of the elastic properties along the growth direction can generate zone-folded acoustic modes in the 100 GHz to THz range. An electric field is present in the strained piezoelectric material in a multiple-quantum well. When the pump beam enters the superlattices, photo-excited electrons and holes are spatially separated and generate charge density variation, which causes the system to lose mechanical equilibrium. As the lattice relaxes, an acoustic wave is launched with a frequency tuned by the period between layers [65–70]

In previous studies, acoustic waves with frequencies from a few hundred GHz to a

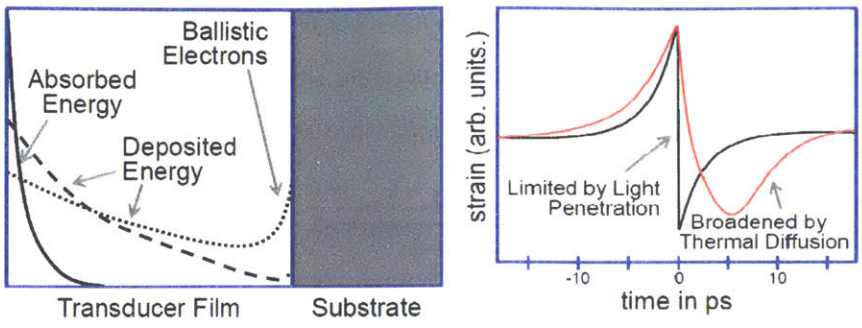

Figure 2-5: Strain profile in a transducer film. The figure on the left shows the effect of electron diffusion on the deposited energy across the film thickness. If the electron can diffuse deep into the film before losing its excess energy to the lattice, then more energy can be deposited deeper in the film until electrons are stopped by an interface with an insulating substrate, dumping energy at the interface. The figure on the right shows a bipolar rectangular pulse broadened by thermal diffusion. The broadened acoustic strain has reduced bandwidth as a result. Figure adopted from [63, 64]

few THz (with fundamental frequencies between about 300 and 800 GHz) have been measured using GaN/InGaN and $SrRuO_3/SrTiO_3$ superlattices. In a study with a GaN/InGaN superlattice in the Nelson Group, acoustic harmonic frequencies up to 2.5 THz has been observed using a quantum well/barrier superlattice with closely matched acoustic impedance and velocities, resulting in zone-center eigenmodes. Up to about 2 THz, no significant peak broadening is observed, but peak broadening and signal to noise ratio became an issue above 2 THz [69]. Photoacoustic techniques with GaN/InGaN superlattices will be further discussed in Chapter 4. Up to 1.45 THz fundamental frequency phonons were generated and detected for phonon lifetime measurements in GaN based structures.

2.4.2 Photodetection of acoustic strain: Brillouin scattering

There are multiple ways to measure acoustic strains either by monitoring the reflected/transmitted probe intensity or by tracking the displacement of a reflective surface. Multiple strain detection mechanisms monitoring reflected or transmitted probe intensity will be discussed throughout this thesis, and Brillouin scattering is one of them. Brillouin Scattering is based on the photoelastic effect [71]. The dielec-

tric constants change when a strain pulse η enters a medium, changing the reflected optical probe intensity. The change in refractive index $\delta n(z,t)$ with applied strain along the z axis as a function of position and time is,

$$\begin{aligned} \delta n(z,t) &= \frac{\partial n}{\partial \eta_{33}} \eta_{33}(z,t) \\ &= -\frac{1}{2} P n^3 \eta_{33}(z,t), \end{aligned} \tag{2.27}$$

where P is photoelastic constant of the material [71, 72]. Most of the probe beam gets reflected at the transducer film, while a portion of it is reflected by a propagating acoustic wave front with index of refraction $n + \delta n$. Depending on the distance that the acoustic wavepacket traveled during the time between the pump excitation and probe interaction, the total reflected intensity will change due to the interference between the reflected beam from the film and from the wave front. In time, as the acoustic wave travels in material of interest, the total reflected intensity will oscillate between constructive or destructive interferences at a phonon frequency,

$$f = \frac{2n(\lambda)v}{\lambda} \cos\theta, \tag{2.28}$$

where n is the reflective index, λ is the probe wavelength, v is speed of sound, and θ is the back-scattering angle. The Brillouin frequency can provide information on the speed of sound when the refractive index at the probe wavelength is known. The measurement is also sensitive to the acoustic attenuation $\Gamma(f)$ given by,

$$\Gamma = 2\pi \frac{\Delta f}{2}, \tag{2.29}$$

where $\Delta f/2$ is the full width at half maximum of the Brillouin peak. The Brillouin scattering oscillations can be described by a wave form,

$$\Delta R = A_0 \exp(-\Gamma t) \cos(2\pi f t + \phi), \tag{2.30}$$

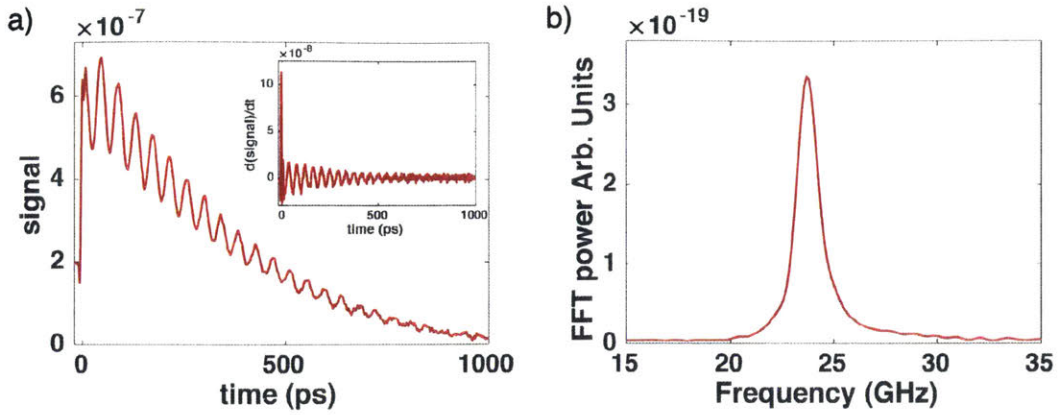

Figure 2-6: Brillouin oscillation and its Fourier transform. (a) The change of the optical reflectivity as a function of time is shown. The data were measured in OM-CTS at 250 K using a 40 nm Cr photoacoustic transducer layer on amorpouse SiO_2 substrate. The inset is the time derivative of the recorded reflectivity change. (b) The Fourier transform of the oscillation that shows the oscillation frequency.

where A_0 is the amplitude, f is the frequency, and ϕ is the phase defining the zero of time.

The functional form above does not capture all the features of the acquired data due to slowly decaying thermal expansion of the transducer layer, as shown in the Figure 2-6 (a). To address this, a decaying background term can be added to the functional form of the Brillouin scattering oscillation. By adding a single exponential decay for thermal background and lock-in offset level δ, the functional form becomes,

$$\Delta R = A_0 \exp(-\Gamma t)\cos(2\pi f t + \phi) + B_0 \exp(-\frac{t}{\mu} + \delta), \tag{2.31}$$

where B_0 is the initial amplitude of the temperature induced reflectivity change, and μ is the time constant for transducer cooling [73].

The thermal background can easily be compensated by taking a time derivative as shown in the inset of Figure 2-6 (a). The time derivative provides an accurate way to determine the oscillation frequency through Fourier transformation, since it preserves the periodicity and rate of decay from the original signal. Even though the numerical differentiation increases the noise level significantly, the time derivative of the recorded signals is used to filter out the thermal background when the signal to

noise ratio is sufficiently high, due to complexity from multiple fitting parameters in the Brillouin oscillation functional form.

2.5 Transient thermal grating techniques

In addition to picosecond ultrasonics, the transient thermal grating method, also known as impulsive stimulated scattering, was employed to study thermal transport. The transient thermal grating (TTG) technique is a four-wave mixing process between two pumps, a probe, and a reference beam that can detect and characterize from few tens of MHz to a few GHz acoustic waves when visible beams are used. Using 13 nm extreme ultraviolet (EUV) radiation as pumps, tens of GHz range surface acoustic phonons were observed in diamond, BK-7 glass, and $Bi_4Ge_3O_{12}$, and 2.8 THz optical phonons were observed in $Bi_4Ge_3O_{12}$, but EUV TTG is out of the scope of this thesis [74]. By spatially and temporally crossing two plane waves with the same wavelength and polarization, a periodic intensity profile is generated through interference. This well established technique was used for studying thermal transport discussed in Chapter 5 [75]. When the intensity profile irradiates a sample, a sinusoidal thermal grating with interference period L is formed given by,

$$L = \frac{2\pi}{q} = \frac{\lambda}{2\sin\left(\frac{\theta}{2}\right)}, \tag{2.32}$$

where q is the grating wavevector magnitude, λ is the laser wavelength, and the θ is the beam crossing angle. The period is independent of the material refractive index because the angle change from refraction is counteracted by optical wavelength shift. A schematic illustration of the beam geometry is shown in Figure 2-7.

2.5.1 Material excitation

When short laser pump pulses are crossed on an isotropic sample, periodic heating and fast thermal expansion results in a transient thermal grating and a step-function-like stress. The stress response launches counter propagating acoustic waves. The

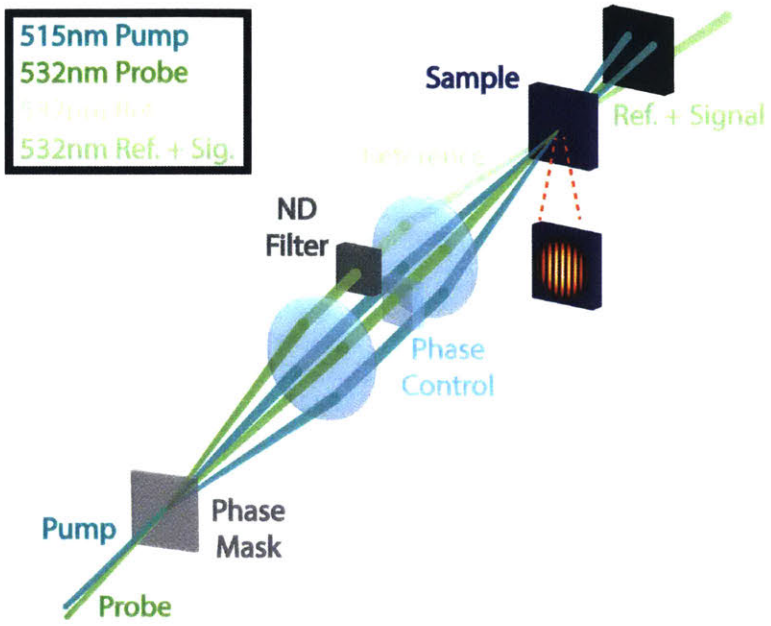

Figure 2-7: Schematic illustration of the transient thermal grating setup. Two pulsed laser pumps create a sinusoidal excitation pattern, which can be probed through diffraction from the periodic index of refraction change.

temperature rise in the material δT is proportional to the intensity of light with a relationship given by,

$$\delta T(x) \propto I(x) = I_0 \cos^2(\frac{q}{2}x) = \frac{1}{2} I_0(1 + \cos(qx)), \tag{2.33}$$

where $I(x)$ is the spatially periodic intensity profile, I_0 is the initial intensity from absorbed energy, q is the grating wavevector. The period of the resulting thermal profile and the wavelength of the acoustic wave match the period of the interference pattern from equation 2.32. The stress from thermal expansion σ_{ij} is given by,

$$\sigma_{ij}(x) = c_{ijkl}\kappa_{kl}\delta T(x) \propto c_{ijkl}\kappa_{kl} cos(qx), \tag{2.34}$$

where c_{ijkl} is the elastic stiffness tensor and κ_{kl} is the thermal expansion tensor [76, 77]. In an isotropic material, c_{ijkl} becomes the bulk elastic modulus and κ_{kl} becomes the linear thermal expansion coefficient. In the region that two counter-propagating waves overlap, a standing wave is formed. The wave will continue to propagate until the

energy is dissipated by material damping. The temperature profile will decay over time due to heat transport. The thermal and acoustic excitations cause change in the refractive index, which can be probed by diffraction of a probe beam [78, 79].

2.5.2 Heterodyne detection

The time-dependent and spatially periodic excitation generates acoustic waves and thermal expansion that changes index of refraction [75, 80]. In the linear regime, the change in real and complex part of the complex refractive index, δn and δk respectively, are given by,

$$\delta n = \frac{\partial n}{\partial \eta} d\eta + \frac{\partial n}{\partial T} dT \tag{2.35}$$

$$\delta k = \frac{\partial k}{\partial \eta} d\eta + \frac{\partial k}{\partial T} dT. \tag{2.36}$$

The strain response from the applied stress is expressed with η. The change in the real component of the index of refraction n leads to transient phase gratings, while the change in the imaginary component k results in transient amplitude gratings. When a continuous wave (CW) laser probe beam reaches the grating, the diffracted beam is directed to a detector whose output is read by fast detection electronics. The time dependent signal is recorded with a 33 GHz oscilloscope.

Transmission Mode

To separate amplitude and phase grating contributions in the signal, a heterodyne detection scheme is employed. To do this, the CW probe beam is split into two parts: the probe and reference beams. The reference beam is usually attenuated and directed to the detector. The probe beam has a thin glass plate in its optical path to control the relative phase between the probe beam and the reference beam. When the probe irradiates excited sample, the diffracted beam is superposed with the reference beam, yielding time dependent signal [82]. Neglecting reflection at the interfaces, the probe transmission through a thin sample Υ can be described by a complex transfer

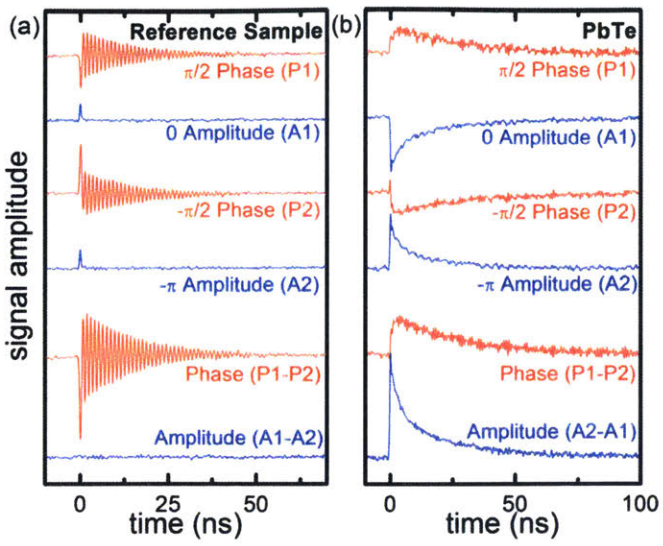

Figure 2-8: Transient grating data from a reference liquid sample m-xylene (a) and a solid sample PbTe (b). The grating period was 2.05μm and the heterodyne phases were $\varphi = \pi/2, 0, -\pi/2, -\pi$. The acoustic waves are shown only in the phase grating. Especially in PbTe, only thermal decay can be seen in the amplitude grating. Figure adapted from [81].

function as [83, 84],

$$\Upsilon(x,t) = \Upsilon_0(1 + \cos(qx)[i\Upsilon'(t) - \Upsilon''(t)], \tag{2.37}$$

$$where\ \Upsilon_0 = \exp(i(\Upsilon_0'(t) + i\Upsilon_0''(t))). \tag{2.38}$$

Here, $\Upsilon'(t)$ and $\Upsilon''(t)$ are the real and complex part of the transmission function, q is the transient grating wavevector, and Υ_0 is the transmission function in the absence of excitation from the pump. $\Upsilon'(t)$ will result in a phase grating, while $\Upsilon''(t)$ will result in an amplitude grating. The equation 2.38 can be rewritten with δn and δk as,

$$\Upsilon(x,t) = \Upsilon_0(1 + \cos(qx)[i\delta n(t) - \delta k(t)] \tag{2.39}$$

The electric field of the probe and the reference beams as plane waves can be expressed as,

$$E_p = E_{p0}\exp(i(k_p^2 - \frac{q^2}{4})^{1/2}z - i\frac{q}{2}x - i\omega_p t + i\varphi_p) \tag{2.40}$$

$$E_r = a_r E_{p0} \exp(i(k_p^2 - \frac{q^2}{4})^{1/2} z + i\frac{q}{2}x - i\omega_p t + i\varphi_r), \tag{2.41}$$

where a_r is the reference attenuation coefficient, E_{p0} is the amplitude of the incident probe, k_p is the optical wavevector of the probe, q is the wavevector of the transient grating, ω_p is the frequency of the optical light, and φ_p and φ_r are the probe and reference phases. Then from equations 2.38 and 2.40, the signal E_s from the +1 diffraction order is,

$$E_s = E_{p(+1)} = E_{p0}\Upsilon_0[i\delta n(t) - \delta k(t)] \exp(i(k_p^2 - \frac{q^2}{4})^{1/2} z - i\frac{q}{2}x - i\omega_p t + i\varphi_p). \tag{2.42}$$

For the heterodyne detection to work, the first order diffraction from the probe has to overlap with one of the reference beam diffraction orders. The first order diffraction from probe beam overlaps with 0^{th} diffraction order of the reference beam given by,

$$E_{r(0)} = a_r E_{p0}\Upsilon_0 \exp(i(k_p^2 - \frac{q^2}{4})^{1/2} z + i\frac{q}{2}x - i\omega_p t + i\varphi_r). \tag{2.43}$$

Since the probe and the 0^{th} order reference fields are collinear, the interference between the two results in a field intensity,

$$I_{s+r(0)} = I_{p0}\Upsilon_0^2(a_r^2 + \delta n^2(t) + \delta k^2(t) - 2a_r[-\delta n(t)\sin\varphi + \delta k(t)\cos\varphi]), \tag{2.44}$$

where I_{p0} is the intensity of the probe beam and $\varphi = \varphi_p - \varphi_r$ is the heterodyne phase. If the reference beam is absent, the diffraction signal without heterodyning is,

$$I_{s0} = I_{p0}\Upsilon_0^2(\delta n^2(t) + \delta k^2(t)), \tag{2.45}$$

showing mixed contributions from both phase and amplitude gratings. To minimize complexity in the analysis of the signal, it is beneficial to have much larger intensity for the reference beam than the diffracted signal ($a_r \gg \delta n,\ \delta k$). In this case, the heterodyne signal dominates and has the form,

$$I_{s(het)} = 2I_{p0}\Upsilon_0^2 a_r[-\delta n(t)\sin\varphi + \delta k(t)\cos\varphi]. \tag{2.46}$$

Since the signal is proportional to the probe intensity and reference attenuation, increasing both probe and reference intensity is beneficial. The probe intensity is increased as high as possible during an experiment within the linear material response regime avoiding over heating and sample damage. The reference beam is attenuated just enough to avoid detector saturation.

Due to the heterodyne phase φ dependence above, either the phase or amplitude grating contribution to the signal can be isolated. When $\varphi = n\pi$, where n = 0, $\pm$ 1, $\pm$ 2, etc., the signal will come from the phase grating. When $\varphi = (n+1/2)\pi$, where n = 0, $\pm$ 1, $\pm$ 2, etc.,the signal comes from the amplitude grating. The ability to select between the phase and amplitude grating signal permits unambiguous analysis of the transient grating signal, and subtracting signals with π phase difference eliminates any non-heterodyne terms. In the investigation of thermal transport in the Chapter 5, an amplitude grating will be used to measure thermal decay.

Reflection Mode

For strongly absorptive materials at the laser wavelengths used, the beam is absorbed near the surface and the transmission is too small to effectively measure. In this case, the reflected reference along with the diffracted signal is guided to the detector for a reflection mode measurement. Upon energy absorption, the complex reflectivity changes and a net surface displacement from thermal expansion occurs. The complex reflection function is given by,

$$r(x,t) = r_0 \exp(i(\gamma'(t) + i\gamma''(t)) \cos(qx)) \exp(-i2k_p u(t) \cos(qx) cos(\beta_p)), \qquad (2.47)$$

where r_0 is the reflectivity of the sample without excitation, γ' is the change in the amplitude of the reflectivity, γ'' is the change in the phase of the reflectivity, k_p is the optical wavevector, $u(t)$ is surface displacement, and β_p is the angle of probe incidence. Then, the intensity of the reflection is given by,

$$I_{s(het)} = 2I_{p0} r_0^2 a_r [r'(t) \cos\varphi - (r''(t) - 2k_p u(t) cos(\beta_p)) \sin\varphi], \qquad (2.48)$$

where I_{p0} is the probe amplitude, a_r is the reference attenuation coefficient, and φ is the heterodyne phase as given in the section above. Changing the heterodyne phase provides the amplitude and phase grating separation, but the signal processing is not as straight forward as in the transmission case. The real part of the reflectivity $r'(t)$ will give the amplitude grating, but the phase grating is affected by both the change in reflectivity and the surface displacement, $r''(t) - k_p u(t)\cos(\beta_p)$ [81, 85]. This complicates analysis of the phase grating, but can be a straightforward tool for measuring kinetics of the thermal grating decay. In Chapter 5, both reflection and transmission modes will be used to monitor thermal transports in silicon membranes.

2.6 Temperature dependent measurements

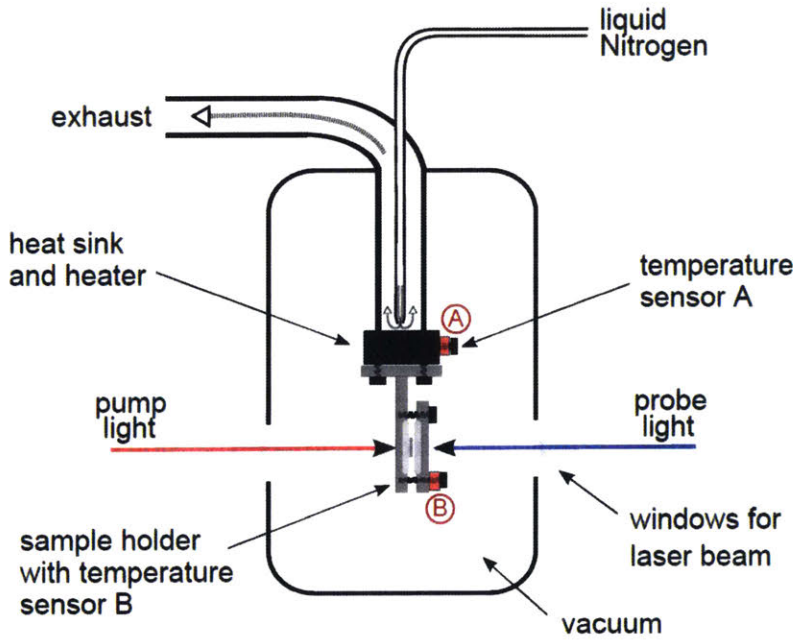

Figure 2-9: Schematic illustration of a cold finger cryostat. The sample sits in a vacuum chamber while the heat transport to and from the sample is mediated by a conductive mount. Figure adapted from [64]

Some of the experiments during the thesis work required either vacuum environment or temperature dependent measurements. To facilitate these needs, a cold finger cryostat from Janis Co., Inc., with model number ST-100 was used, both to heat up

and to cool down the sample of interest. The sample was placed on a copper mount attached to a cold finger in a vacuum sealed chamber. The vacuum provides thermal insulation from the air. When liquid nitrogen is introduced to another chamber with a transfer line, the heat is removed from the sample to the mount to the cold finger to liquid nitrogen. The cryostat has a temperature sensor and a 50W resistive heater on a copper heat sink between two chambers to provide active feedback, and the same heater is used for experiments with higher than room temperature needs. Turbulence from the nitrogen flow is not an issue due to chamber separation, providing high optical stability, but extra care is needed to mechanically stabilize the transfer line. A heat tape was used on the exhaust to ensure that condensation of water does not freeze and clog the exhaust opening. The ST-100 cold finger cryostat has a temperature range from 4K up to 500K, but it needs 15 minutes to an hour for the temperature to equilibrate depending on the sample and the temperature range. To ensure stable measurements, the nitrogen flow and the operation current of the heater were closely monitored. With high nitrogen flow, the transfer line could vibrate, hindering stable measurement in the cryostat, and the heater under high load resulted in bigger temperature fluctuations and longer times to equilibrate. The temperature recorded with the sensors on the cold finger had an absolute uncertainty range of $\pm$ 2K, and the temperature stability under normal operation was better than $\pm$ 0.2 K.

2.7 Summary

In this chapter, photoacoustic spectroscopy and experimental methods were introduced. First, concepts of stress and strain were introduced to better understand how mechanical spectroscopy worked. Next, pump-probe spectroscopy using an ultrashort pulsed laser was introduced so that ultrafast dynamics, events occurring in shorter than picosecond or $10^{-}12$ s timescale, could be monitored. Optical generation and detection of strain through picosecond laser ultrasonics and transient thermal grating techniques were presented. Between these two techniques using optical lasers, acoustic waves with frequencies from a few MHz to hundreds of GHz could be readily

accessed. The remainder of the thesis is focused on extending the higher end of the acoustic wave frequency range and understanding thermal transport in condensed matter, especially in semiconductors.

Chapter 3

Ultrafast Photoacoustics through Magnetostriction

Magnetostriction is a property of ferromagnetic materials to expand or contract in response to a magnetic field. When a magnetic field is applied to a ferromagnetic material, the molecular dipoles and the magnetic field boundaries inside the sample rotate to minimize the energy. These processes stress and deform the material, and can convert some of the electromagnetic energy into the mechanical energy [86]. The first measurement of magnetostriction was performed by James Prescott Joule in 1847, by measuring change in the length of an iron sample under an applied magnetic field [87]. The opposite effect, magnetic susceptibility change under mechanical stress, was discovered by E. Villari in 1865 [88]. However, the practical application of magnetostriction only started appearing from the World War II era, when nickel based alloys were used as transducers for sound navigation and ranging (sonar) systems [89].

In the 1960s, the magnetic and magnetoelastic properties of rare-earth elements were comprehensively studied leading to a discovery of $\Re Fe_2$, where $\Re$ represents a rare earth element such as samarium (Sm), terbium (Tb), dysprosium (Dy), erbium (Er), and thulium(Tm). These alloys showed strong exchange interaction and high magnetoelastic coupling. The electrons in highly anisotropic 4f orbitals and the strong Fe-Fe and Fe-$\Re$ exchange coupling resulted in the strong magnetostriction and high Curie temperatures [90–93]. Following the development of ultrafast lasers with

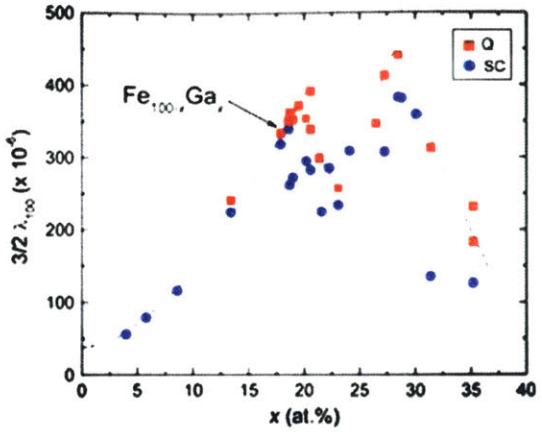

Figure 3-1: Magnetostriction coefficient λ_{100} in bulk $Fe_{1-x}Ga_x$ as a function of Ga concentration. The blue dots were measured in slowly cooled samples, while the red dots were measured in thermally quenched samples. Figure adapted from [96]

femtosecond pulses and the beginning of picosecond ultrasonic spectroscopy in the 1980s, coherent acoustic phonons were generated to decrease the magnetization modulus of magnetic materials at subpicosecond timescales or to switch magnetization of ferromagnetic materials [35, 94, 95]. In this chapter, ultrafast laser study of magnetostrictive $Fe_{1-x}Ga_x$ to generate and detect GHz to THz frequency range longitudinal and shear acoustic waves is described.

3.1 Galfenol ($Fe_{1-x}Ga_x$) samples

Among the known materials, binary compounds $\Re Fe_2$ show the strongest magneto-crystalline anisotropy, or magnetostriction coefficients. For example, $TbFe_2$ has the highest magnetostriction coefficient of $\lambda_{s,111} = 1750 \times 10^{-6}$, compared to iron with $\lambda_{s,100} = 21 \times 10^{-6}$ and $\lambda_{s,111} = -21 \times 10^{-6}$, where the negative sign implies contraction rather than expansion [97]. However, due to high magneto-crystalline anisotropy in $\Re Fe_2$, a high magnetic field is needed to saturate the deformation for these systems. To address the high anisotropy problem, $Tb_{0.27}Dy_{0.73}Fe_{1.95}$ alloy (terfenol-D) was introduced. Terfenol-D has high magnetostriction 1600×10^{-6} at room temperature with a low saturation field, but it is brittle with tensile strength of about 28 MPa. In

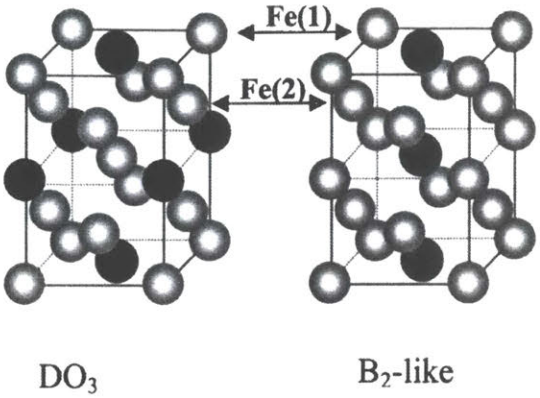

Figure 3-2: $Fe_{0.75}Ga_{0.25}$ crystalline structure model. The gray spheres represent Fe and the black ones represent Ga atoms. Figure adapted from [96]

an attempt to balance a large magnetostriction coefficient, a high Curie temperature, and a high tensile strength, galfenol ($Fe_{1-x}Ga_x$) was developed in 1999 by scientists at the Naval Surface Warfare Center [98]. Galfenol with 80 percent iron and 20 percent gallium has magnetostriction coefficient of $\lambda_{s,100} = 400 \times 10^{-6}$ with tensile strength of about 500 MPa [98, 99].

For bulk galfenol, a team of scientists led by A. E. Clark at the Naval Surface Warfare Center reported the magnetostriction and the elastic constants of $Fe_{1-x}Ga_x$ with varying gallium concentrations [96]. The dependence of magnetostriction coefficient on the gallium concentration is shown in Figure 3-1. The team also reported the effect of thermal treatments on the sample prepared at 1000 °C. One set of samples experienced constant cooling at 10 °C/min, and another set was dropped into a water bath and experienced a quenching. The study shed light on complicated galfenol atomic structures. For $x = 20\%$ sample used for the samples used in this chapter, there were three different types of bcc networks [100]. In the A_2 structure, Fe and Ga atoms were randomly distributed. In the B_2 structure, Ga pairs occupied second nearest neighbor sites along the [100] directions. In the DO_3 structure, Ga pairs occupied neighboring sites along the [110] directions. Only A_2 and DO_3 structures are present in the slowly cooled samples, while B_2 structure is also present in the quenched samples.

The two galfenol samples, used for the study presented in this chapter, were

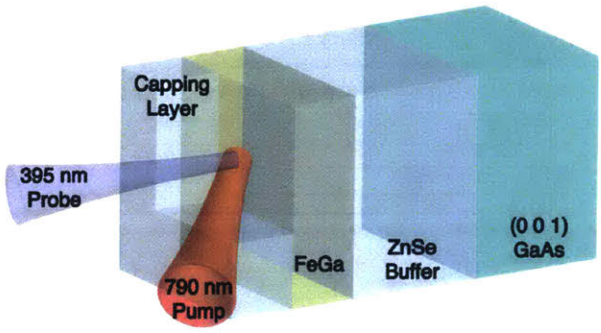

Figure 3-3: Schematic illustration of the FeGa sample structure. A galfenol film was grown on top of a GaAs(001) substrate and a ZnSe buffer layer. The FeGa layer was capped with either ZnSe or Au. The figure is drawn out of proportion.

grown with molecular beam epitaxy by a team of scientists at the Paris Institute of Nanosciences (INSP), France. On a GaAs(001) substrate, a GaAs buffer and a 20 nm ZnSe epitaxy buffer were deposited. Then, an epitaxial FeGa thin film with the [001] out-of-plane orientation was deposited on top, capped with either a gold or a ZnSe layer. One of the samples had a 25-nm-thick FeGa and a 360 nm ZnSe capping layer. The other sample was prepared with a 92 nm FeGa film and a 6 nm Au capping layer. The FeGa films were prepared with 80 percent iron and 20 percent gallium to maximize the magnetoelastic coupling and with a cubic structure to stabilize the in-plane magnetization equilibrium orientation [101].

3.2 Introduction to laser-induced magnetostriction

3.2.1 Femtomagnetism

In a ferromagnetic material, a spontaneous magnetization occurs at temperatures below the Curie point. In other words, ferromagnets have preferred internal magnetic moments even in the absence of an external magnetic field, if the temperature is below a material-dependent point. Above this temperature, materials become paramagnetic, because thermal vibrations hinder the alignments. Within the magnetic material, there are magnetic domains with their own defined magnetic moments. Once a ferromagnetic material is exposed to an external magnetic field, it undergoes

an irreversible non-linear response by aligning magnetic moments to minimize the energy. The Zeeman energy, which is the energy of a magnetic moment in an external field is given by,

$$E_z = -\mu_0 \int_V \mathbf{M} \cdot \mathbf{H}_{ext} dV, \tag{3.1}$$

where μ is the magnetic dipole moment of an atom, $\mathbf{M}$ is the local magnetization, $\mathbf{H}_{ext}$ is the external field, and the integral is over the volume of interest. Even when the field is removed, part of the alignment will remain and the material remains magnetized, until either heat or an opposite-direction magnetic field is applied [102].

Femtomagnetism is the study of changes in magnetic materials upon impacts of femtosecond laser pulses, started in late 1990s [94]. The femtomagnetism is crucial in understanding the fast dynamics of laser-induced demagnetization, in the ~1 ps demagnetization timescale [103]. Materials with a strong magnetoelastic coupling are expected to generate both longitudinal and shear acoustic waves by releasing stress from laser-induced demagnetization. Even though, there is no consensus on a model to describe how this phenomenon manifests, the phenomenological three-temperature (3TM) model was proposed to describe laser-induced demagnetization of ferromagnetic materials [94].

When ferromagnetic materials are excited by a pump pulse, incoherent dynamics dominate the first picosecond, and the magnetization quickly drops. In the next hundreds of picoseconds, coherent precession of the magnetization around the effective field manifests. The 3TM model provides simple description of the energy equilibration process without considering a transfer of the angular momentum, instead it focuses on the energy flux between electrons, spins, and the lattice. The energy fluxes between these subsystems can be described by,

$$C_e \frac{dT_e}{dt} = P(t) - g_{ep}(T_e - T_p) - g_{es}(T_e - T_s), \tag{3.2}$$

$$C_s \frac{dT_s}{dt} = -g_{es}(T_s - T_e) - g_{sp}(T_s - T_p), \tag{3.3}$$

$$\textit{and } C_p \frac{dT_p}{dt} = -g_{ep}(T_p - T_e) - g_{sp}(T_p - T_s), \tag{3.4}$$

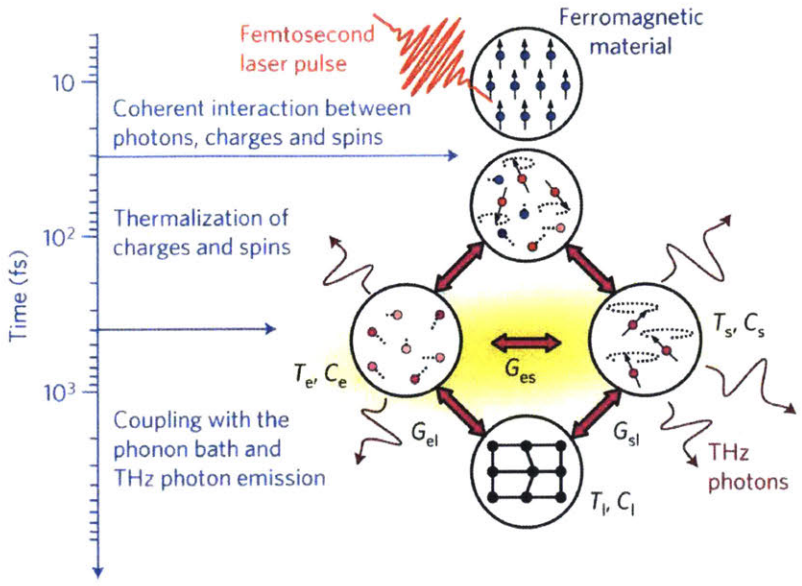

Figure 3-4: Schematics of energy transfer dynamics in a magnetic material upon a photo-excitation. The coupling between spins, charges, and the lattice are expected to launch THz phonons. Figure adapted from [104]

where C is the specific heat and T is the temperature for electron (e), spin (s), and lattice (p). The coupling constants g_{ep}, g_{es}, and g_{sp} indicate the coupling strength between electron-lattice, electron-spin, and spin-lattice respectively [94].

Within the first 50 femtoseconds (fs), photons from the fs pump laser pulse interact coherently with the electrons and the spins in the ferromagnet. Over the next hundreds of fs to a ps, the excited charges and spins relax and thermalize resulting in a demagnetization of the ferromagnet, for which the fundamental mechanism is under intense debate. Then, the heat exchange between the charges and the spins with the lattice follows. During this process, a magnetic precession starts as one of the relaxation mechanisms, as will be presented later in the chapter. But more importantly, an orbit-lattice coupling could induce THz phonons [104, 105].

3.2.2 Detection through magneto-optical Kerr effect

The magneto-optic Faraday effect or the magneto-optical Kerr effect(MOKE) enables the detection of a presence or a change in a magnetization of a sample through a rotation of the polarization and a change in the reflectivity of light interacting with

the medium. While the magneto-optic Faraday effect is detected by the transmitted light, MOKE detects changes in the reflected light from a magnetized surface. The dielectric tensor of the magnetic medium is given by,

$$\tilde{\varepsilon} = \varepsilon \cdot \begin{vmatrix} 1 & i \cdot \mathbf{Q}_z & -i \cdot \mathbf{Q}_y \\ -i \cdot \mathbf{Q}_z & 1 & i \cdot \mathbf{Q}_x \\ i \cdot \mathbf{Q}_y & -i \cdot \mathbf{Q}_x & 1 \end{vmatrix}, \tag{3.5}$$

where Q_i is the Voigt vector for $i = x, y, z$, proportional to $\mathbf{M}$ by,

$$\mathbf{Q} = q \cdot \mathbf{M}, \tag{3.6}$$

where q is the Voigt constant. Depending on the plane of probe incidence and the orientation of the magnetization vector M, there are three MOKE geometries. The first one is the polar MOKE, where the magnetization of the film lies perpendicular to the film surface and in the plane of the probe incidence. The change of probe polarization is proportional to the out-of-plane magnetization. The second geometry is the longitudinal MOKE where the magnetization is parallel to both the reflective surface and the plane of incidence. The light is reflected in an angle away from normal to the surface, and becomes elliptically polarized. The change in the polarization is directly proportional to the in-plane component of the magnetization. Finally, there is a transversal MOKE where magnetization is perpendicular to the plane of incidence and parallel to the surface. The transversal MOKE detects change of reflectivity.

The change in reflectivity $\Delta R(t)$ is given by [35],

$$\Delta R(t) = \int_0^\infty = f(z)\eta(z,t)dz, \tag{3.7}$$

where $f(z)$ is a sensitivity function given by,

$$f(z) = f_0[\underbrace{\frac{\partial n}{\partial \eta_{33}} \sin(\frac{4\pi nz}{\lambda} - \phi)}_{A} + \underbrace{\frac{\partial k}{\partial \eta_{33}} \cos(\frac{4\pi nz}{\lambda} - \phi))}_{B}]e^{-z/\zeta}, \tag{3.8}$$

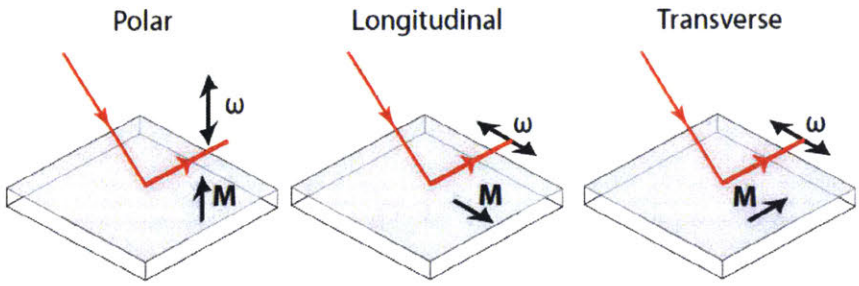

Figure 3-5: Three magneto-optical geometries. The polarization changes in the polar and the longitudinal MOKE, whereas the reflectivity changes in the transversal MOKE. Figure adapted from [106]

where f_0 is the initial reflectivity response, n and k are the real and complex components in the complex index of refraction, λ is the optical wavelength, ϕ is the phase term, and the ζ is the probe skin depth. The ratio between the smooth optical constants term A and the sharp pulse shape term B reveals the shape of the transient reflectivity response.

In the MOKE detection, the reflected probe polarization is analyzed, using a quarter-wave plate and a Wollaston prism, which splits the probe into two orthogonally polarized pulses. The split pulse is guided to a detector pair used for the balanced detection. If the probe experiences a polarization ellipticity change or a rotation, the change can be recorded by the intensity differential. The strain propagating in the z-axis, with nonzero shear ($\eta_4 = 2\eta_{yz}$, $\eta_5 = 2\eta_{xz}$) and longitudinal ($\eta_3 = 2\eta_{zz}$) components, can modulate the permittivity tensor $\Delta\varepsilon$ of the isotropic film as given by,

$$\Delta\varepsilon = \begin{vmatrix} P_{12}\eta_3 & 0 & P_{44}\eta_5 \\ 0 & P_{12}\eta_3 & P_{44}\eta_4 \\ P_{44}\eta_5 & P_{44}\eta_4 & P_{11}\eta_3 \end{vmatrix}, \tag{3.9}$$

where P_{11}, P_{12}, and $P_{44} = (P_{11} - P_{12})/2$ are the photoelastic tensor components [76, 107]. The induced probe polarization change depends on the z-component of the probe electric field. To better overlap the probe wavevector and the shear photoelastic term, the probe pulse was introduced obliquely.

3.2.3 Free energy density of magnetostrictive thin films

In a mechanistic approach to magnetoelasticity, coupling between the elastic and the magnetic behaviors can be explained by a modification of the free energy density F_t of a crystal given by [105, 108],

$$F_t = F_k + F_e + F_z + F_{ex}, \tag{3.10}$$

where F_k is the magneto-crystalline energy, F_e is the elastic energy, F_z is the Zeeman energy, and F_{ex} is the exchange energy. The magneto-crystalline energy can be expressed as,

$$F_k(m, \varepsilon_{ij}) = F_a + F_{me}(m, \varepsilon_{ij}), \tag{3.11}$$

where $F_a = K_1(m_1^2 m_2^2 + m_2^2 m_3^2 + m_3^2 m_1^2)$ is the anisotropy energy to model the magnetization along different crystalline axes for an anisotropy constant K_1, a unit vector m along $\mathbf{M}$, and the projection of m, m_i (i = 1,2,3). ε_{ij} is the deformation tensor in the Cartesian coordinate. F_{me} is the magnetoelastic energy expressed as,

$$F_{me} = \sum_{ij} \sum_{kl} = (b_{ij})_{kl} m_k m_l \varepsilon_{ij}, \tag{3.12}$$

where b is the magnetoelastic tensor. The elastic energy is,

$$F_e = \frac{1}{2} \sum_{ijkl} c_{ijkl} \varepsilon_{ij} \varepsilon_{kl}, \tag{3.13}$$

where c_{ijkl} is the elastic tensor. The Zeeman energy is,

$$F_z = -M_s(m H_i), \tag{3.14}$$

where M_s is the saturation magnetization, and H_i is the demagnetizing fields. Finally, the exchange energy in cubic symmetry is,

$$F_{ex} = \frac{1}{2} H_{ex} a^2 M_s((\nabla m_x)^2 + (\nabla m_y)^2 + (\nabla m_z)^2), \tag{3.15}$$

where H_{ex} is the exchange field, and a is the lattice constant.

If the crystallographic axes [100], [010], [001] coincides with the x, y, z axes respectively, the equation 3.12 and 3.13 are simplified to [50],

$$\begin{aligned} F_{me} = b_0(\varepsilon_{xx} + \varepsilon_{yy} + \varepsilon_{zz}) + b_1(m_x^2\varepsilon_{xx} + m_y^2\varepsilon_{yy} + m_z^2\varepsilon_{zz}) \\ +b_2(m_x m_y \varepsilon_{xy} + m_x m_z \varepsilon_{xz} + m_y m_z \varepsilon_{yz}) \end{aligned} \tag{3.16}$$

$$F_e = \frac{1}{2}c_{11}(\varepsilon_{xx}^2 + \varepsilon_{yy}^2 + \varepsilon_{zz}^2) + c_{12}(\varepsilon_{xx}\varepsilon_{yy} + \varepsilon_{yy}\varepsilon_{zz} + \varepsilon_{xx}\varepsilon_{zz}) + \frac{1}{2}c_{44}(\varepsilon_{xy}^2 + \varepsilon_{yz}^2 + \varepsilon_{xz}^2), \tag{3.17}$$

where b_0, b_1, and b_2 represent the isotropic, tetragonal, and rhomboidal magnetoelastic constants, ε_{ij} is the elastic strain tensor, and c_{11}, c_{12}, and c_{44} are the elastic constants of a cubic crystal.

The relative change in length $\frac{\Delta l}{l}$ along an arbitrary measurement direction with directional cosines β_i under a magnetization is given by [109],

$$\frac{\Delta l}{l} = \sum_{ij} \varepsilon_{ij} m_i \beta_j, \tag{3.18}$$

where the strain components depend on the magnetization directions. These equilibrium strains ε_{ij} as a a function of the magnetization direction m_j can be found from the equation 3.16 and 3.17, resulting in

$$\varepsilon_{ii} = -\frac{b_0}{c_{11} + 2c_{12}} - \frac{b_1 m_i^2}{c_{11} - c_{12}} + \frac{c_{12} b_1}{(c_{11} + 2c_{12})(c_{11} - c_{12})} \tag{3.19}$$

$$\varepsilon_{ij} = -\frac{b_2 m_i m_j}{c_{44}}, \tag{3.20}$$

where ε_{ii} and ε_{ij} are the longitudinal and shear strains. The relative length change equation can be rewritten, by applying the equations 3.19 and 3.20, as,

$$\frac{\Delta l}{l} = \lambda_\alpha + \frac{3}{2}\lambda_{100}(m_x^2\beta_x^2 + m_y^2\beta_y^2 + m_z^2\beta_z^2 - \frac{1}{3}) + 3\lambda_{111}(m_x\beta_x m_y\beta_y + m_x\beta_x m_z\beta_z + m_y\beta_y m_z\beta_z), \tag{3.21}$$

where λ_α, λ_{100}, and λ_{111} are the magnetostrictive strain constants. These values indicate the relative material shape modification under an external magnetic field.

The $\lambda_\alpha = -\frac{b_0+b_1/3}{c_{11}+2c_{12}}$ term indicate isotropic volume change. The $\lambda_{100} = -\frac{2}{3}\frac{b_1}{c_{11}-c_{12}}$ term show relative deformation along [100]. Finally, $\lambda_{111} = -\frac{b_2}{3c_{44}}$ term show the relative deformation along [111] resulting in a rhomboidal distortion. In a polycrystalline sample, a direction-averaged value, $\lambda_{poly} = \frac{2}{5}\lambda_{100} + \frac{3}{5}\lambda_{111}$, is measured.

3.2.4 Elastic and magnetoelastic energy in FeGa

To consider the static magnetostrictive strain along the [110] direction in the (100) plane of the galfenol films, the elastic constants need to be transformed into the new bases: $x_1' = [110]$, $x_2' = [1\bar{1}0]$, $x_3' = [001]$. The coordinate transformation follows the transformation rule: $c'_{ijkl} = R_{i\alpha}R_{j\beta}R_{k\gamma}R_{l\delta}c_{\alpha\beta\gamma\delta}$, where R is a clockwise $\frac{\pi}{2}$ rotational transformation matrix given by,

$$R = \begin{pmatrix} \frac{1}{\sqrt{2}} & \frac{1}{\sqrt{2}} & 0 \\ -\frac{1}{\sqrt{2}} & \frac{1}{\sqrt{2}} & 0 \\ 0 & 0 & 1 \end{pmatrix}. \tag{3.22}$$

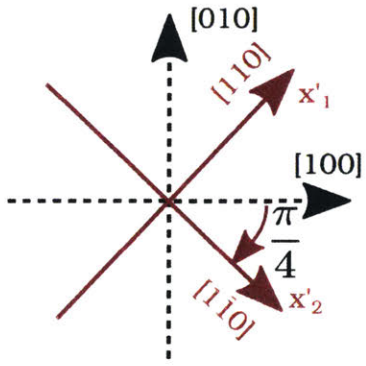

Figure 3-6: Clockwise $\frac{\pi}{2}$ rotational transformation along z-axis. The new bases are $x_1' = [110]$, $x_2' = [1\bar{1}0]$, $x_3' = [001]$.

which results in the elastic components,

$$c'_{\alpha\beta} = \begin{pmatrix} c'_{11} & c'_{12} & c_{12} & 0 & 0 & 0 \\ c'_{12} & c'_{11} & c_{12} & 0 & 0 & 0 \\ c_{12} & c_{12} & c_{11} & 0 & 0 & 0 \\ 0 & 0 & 0 & c_{44} & 0 & 0 \\ 0 & 0 & 0 & 0 & c_{44} & 0 \\ 0 & 0 & 0 & 0 & 0 & \frac{c_{11}-c_{12}}{2} \end{pmatrix} = \begin{cases} c'_{11} = \frac{c_{11}+c_{12}}{2} + c_{44} \\ c'_{12} = \frac{c_{11}+c_{12}}{2} - c_{44} \\ c'_{13} = c_{12} \\ c'_{33} = c_{11} \\ c'_{44} = c_{44} \\ c'_{66} = \frac{c_{11}-c_{12}}{2}. \end{cases} \tag{3.23}$$

Using the equation 3.13 and the new coordinate, the elastic energy is given by,

$$\begin{aligned} F_e =& \frac{1}{2}[c_{11}(\frac{1}{2}\varepsilon^2_{x'x'} + \frac{1}{2}\varepsilon^2_{y'y'} + \varepsilon_{x'x'}\varepsilon_{y'y'} + \varepsilon^2_{z'z'} + \frac{1}{2}\varepsilon^2_{y'x'}) \\ &+c_{12}(\frac{1}{2}\varepsilon^2_{x'x'} + \frac{1}{2}\varepsilon^2_{y'y'} + \varepsilon_{x'x'}\varepsilon_{y'y'} + 2\varepsilon_{x'x'}\varepsilon_{z'z'} + 2\varepsilon_{y'y'}\varepsilon_{z'z'} - \frac{1}{2}\varepsilon^2_{x'y'}) \\ &+c_{44}(\varepsilon^2_{x'x'} + \varepsilon^2_{y'y'} - 2\varepsilon_{x'x'}\varepsilon_{y'y'} + \varepsilon^2_{y'z'} + \varepsilon^2_{z'x'})]. \end{aligned} \tag{3.24}$$

Since only the strain waves along z', (001) direction, are considered with the elastic strain tensors $\varepsilon_{x'x'} = \varepsilon_{y'y'} = \varepsilon_{x'y'} = 0$, the equation 3.24 is simplified to,

$$F_e = \frac{1}{2}[c_{11}\varepsilon^2_{z'z'} + c_{44}(\varepsilon^2_{y'z'} + \varepsilon^2_{x'z'})]. \tag{3.25}$$

The elastic constants are reported by R. A. Kellogg as $c_{11} = 196.0$ GPa, $c_{12} = 156.0$ GPa, and $c_{44} = 123.1$ GPa [98].

Following the coordinate change from above, the magnetoelastic energy from the

equation 3.12 becomes,

$$\begin{aligned}
F_{me} =& b_2[\sum_i m_i^2\varepsilon_{ii} + \sum_{ij} m_i m_j \varepsilon_{ij}] + (b_1 - b_2)\sum_i m_i^2\varepsilon_{ii} \\
=& b_1(\frac{1}{2}\varepsilon_{x'x'}(m_{x'}^2 + m_{y'}^2) + \frac{1}{2}\varepsilon_{y'y'}(m_{x'}^2 + m_{y'}^2) + \varepsilon_{z'z'}m_{z'}^2 + 2m_{x'}m_{y'}\varepsilon_{x'y'}) \\
&+ b_2(\frac{1}{2}\varepsilon_{x'x'}(m_{x'}^2 - m_{y'}^2) + \frac{1}{2}\varepsilon_{y'y'}(m_{y'}^2 + m_{x'}^2) + 2m_{y'}m_{z'}\varepsilon_{y'z'} + 2m_{x'}m_{z'}\varepsilon_{z'x'}) \\
=& b_1\varepsilon_{z'z'}m_{z'}^2 + 2b_2(m_{y'}m_{z'}\varepsilon_{y'z'} + m_{x'}m_{z'}\varepsilon_{z'x'}),
\end{aligned} \tag{3.26}$$

where $b_1 = b_{11} - b_{12}$ and $b_2 = b_{44}$ are the magnetoelastic constants of a cubic crystal. b_{11}, b_{12}, and b_{44} represent the tetragonal, rhomboidal, and isotropic magnetoelastic constants, respectively. In a $Fe_{0.8}Ga_{0.2}$ film, the magnetoelastic constants are $b_1 = -(3/2)\lambda_{100}(c_{11} - c_{12}) = -15.6MJ/m^3$ and $b_2 = -3\lambda_{111}c_{44} = -10.1MJ/m^3$ [96].

In this section, the expressions of the elastic and the magnetoelastic energies were derived. The acoustic modes traveling normal to the surface and the cubic symmetry of galfenol simplified the final expressions for these energies, which are crucial for understanding the laser-induced strain waves amplitudes.

3.2.5 Demagnetostriction of galfenol

By minimizing the free energy density, the built-in static strain in the galfenol film can be obtained. Understanding the static strain in the sample can optimize experimental geometry for picosecond shear acoustic waves generation. In the experimental configuration, the free energy density is the sum of the elastic and magnetoelastic energies. From equations 3.25 and 3.26, the free energy is

$$\begin{aligned}
F = F_e + F_{me} =& \frac{1}{2}[c_{11}\varepsilon_{z'z'}^2 + c_{44}(\varepsilon_{y'z'}^2 + \varepsilon_{x'z'}^2)] \\
&+ b_1\varepsilon_{z'z'}m_{z'}^2 + 2b_2(m_{y'}m_{z'}\varepsilon_{y'z'} + m_{x'}m_{z'}\varepsilon_{z'x'}).
\end{aligned} \tag{3.27}$$

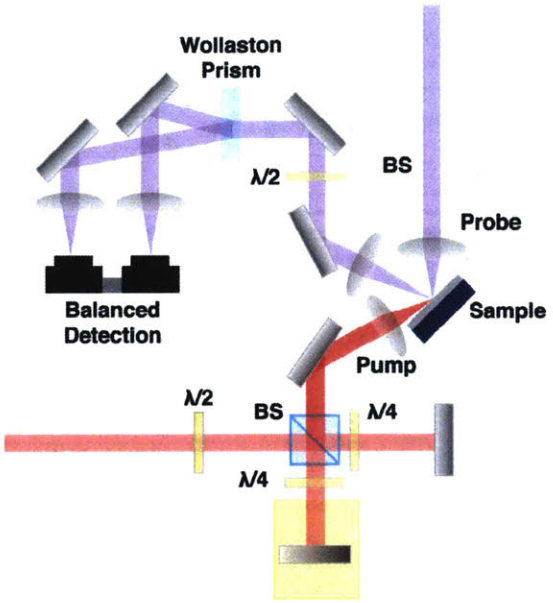

Figure 3-7: Schematics of the experimental setup. The probe was split by a Wollaston prism after hitting the sample, and each polarization arm was directed to a separate detector to track the polarization change in time.

From the relationships, $\frac{\partial F}{\partial \varepsilon_{z'z'}} = 0$, $\frac{\partial F}{\partial \varepsilon_{y'z'}} = 0$, and $\frac{\partial F}{\partial \varepsilon_{x'z'}} = 0$, the expressions of the static magnetoelastic strains are derived as,

$$\varepsilon_{z'z'} = -\frac{b_1 m_z^2}{c_{11}}, \tag{3.28}$$

$$\varepsilon_{x'z'} = -\frac{2b_2 m_x m_z}{c_{44}}, \tag{3.29}$$

$$\text{and } \varepsilon_{y'z'} = -\frac{2b_2 m_y m_z}{c_{44}}, \tag{3.30}$$

where $\varepsilon_{z'z'}$ is the static longitudinal, and $\varepsilon_{x'z'}$ and $\varepsilon_{y'z'}$ are the static shear strains of a [001] galfenol film.

3.3 Experimental scheme

A Coherent Verdi G-18 laser, a Coherent Mira-900 mode-locked Ti:sapphire oscillator, and a Coherent RegA-9000 regenerative amplifier were used to generate 790 nm wavelength pulse with about 4 μJ pulse energy and a 200 fs FWHM pulse width at

a repetition rate of 250 kHz. The output pulse was split unequally to be used as a pump and a probe. The pump was modulated at 41.7 kHz with an acousto-optic modulator to enhance the signal to noise ratio. The probe was time delayed up to 1000 ps to record time-dependent dynamics. A balanced detector was used for the MOKE detection. After the probe hit the sample, it went through a half waveplate and a Wollaston prism to be split into two separate beams of the orthogonal polarizations. The split probe pulses were directed to the balanced detectors, instead of the probe and the reference pulses in a conventional balanced detection scheme. When the probe irradiates the magnetic sample and interacts at the surface, the polarization may be altered and this change can be recorded through the fluctuations in the amplitude. A nonlinear birefringent $\beta - BaB_2O_4$ (BBO) crystal was used to generate 395 nm probe when needed. The two diodes with the opposite polarities were balanced to an equal background intensity prior to each measurement by turning the half waveplate.

Figure 3-7 shows a schematics of the experimental setup. The 790 nm pump arm was split into two using a half waveplate and a polarizing beam splitter pair. One of these arms was time-delayed and intensity-modulated to suppress the precession signal, when both of the arms were used during an experiment. The pump and the probe were introduced at an angle about 34 degrees and 21 degrees off the sample surface, respectively. Even though the probe comes in at a more oblique angle, the schematics does not reflect this for the simplicity.

The sample was placed at the center of two magnetic lenses on a ball-bearing frame, called the "Magnetic Stargate". Permanent nickel-plated neodymium magnet cubes were stacked into a pyramid-shape magnetic lenses, creating an inhomogeneous field from 700 mT along the magnet edges to 1 T at the center. The field profile had a radial gradient. The magnetic lenses were mounted on a steal ball-bearing frame to confine and to guide the field. The ball-bearing made it possible to rotate the whole structure 360 degrees to define the external magnetic field direction [105].

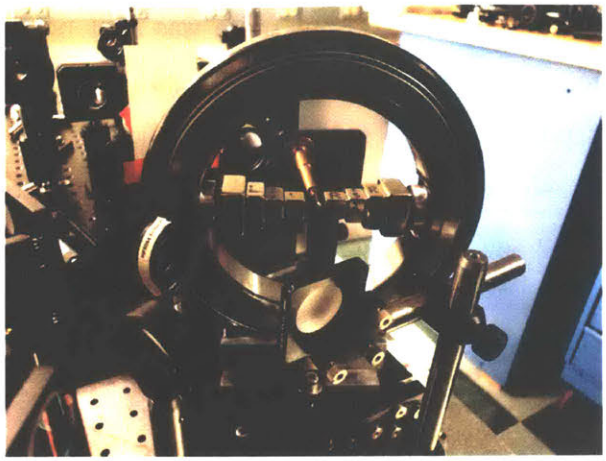

Figure 3-8: Picture of the detection region. The external magnetic field was controlled by the "Magnetic Stargate". Magnets were mounted on a ball-bearing frame to change the polarization of the applied field.

3.4 Experimental results

3.4.1 Brillouin scattering in GaAs and spin precession

The first set of experiments were conducted with a 25 nm $Fe_{0.8}Ga_{0.2}$ sample with a 360 nm ZnSe capping layer. The sample was excited by a 50 mW, 790 nm pump pulse introduced at an angle about 34 degrees off the sample surface, or 56 degrees with respect to the surface normal. The 5 mW probe was introduced at about 21 degrees off the sample surface, or 69 degrees with respect to the surface normal. In Figure 3-9, the rapid change in reflectivity amplitude at time zero is proportional to the pump fluence, corresponding to the laser heating of the electrons and the lattice. On top of this slowly decaying thermal signal, coherent oscillations were recorded that are associated with the inelastic Brillouin scattering of the probe pulse from the propagating acoustic waves and spin precession. The Fourier transform of the signal reveals two distinct frequencies at 8 GHz and 43 GHz. From the Brillouin frequency equation introduced in Chapter 2, $f = \frac{2n(\lambda)v}{\lambda}\cos\theta$, 43 GHz corresponds to Brillouin scattering of 800 nm probe in the GaAs substrate, which leaves the magnetic-field-polarization dependent 8 GHz oscillation to the spin precession in the galfenol sample.

In Figure 3-10, the spectra from the 25 nm galfenol sample measured with a 790 nm

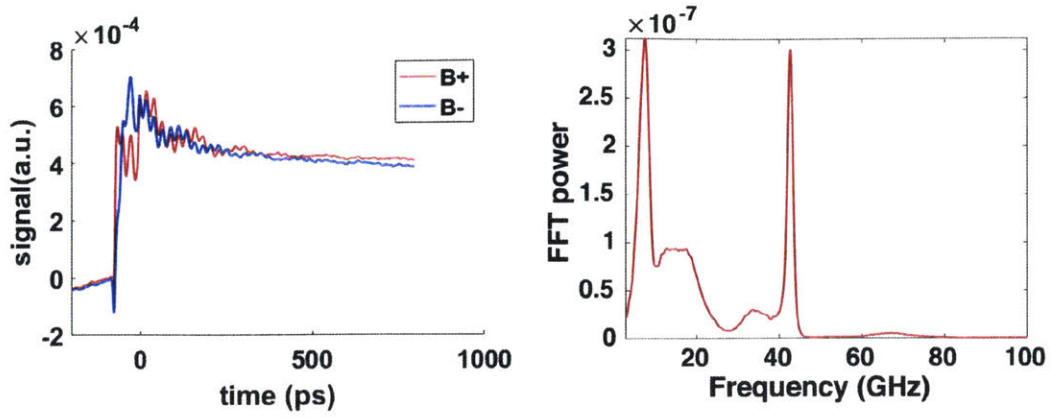

Figure 3-9: Lock-in signal from MOKE detection (left) and Fourier analysis of a signal (right). B+ and B- indicate the opposite polarity (180 degree field rotation) of the external magnetic field. The slow oscillatory signal at 8 GHz corresponds to the precession and the fast oscillation at 43 GHz is the Brillouin oscillation frequency in the GaAs substrate.

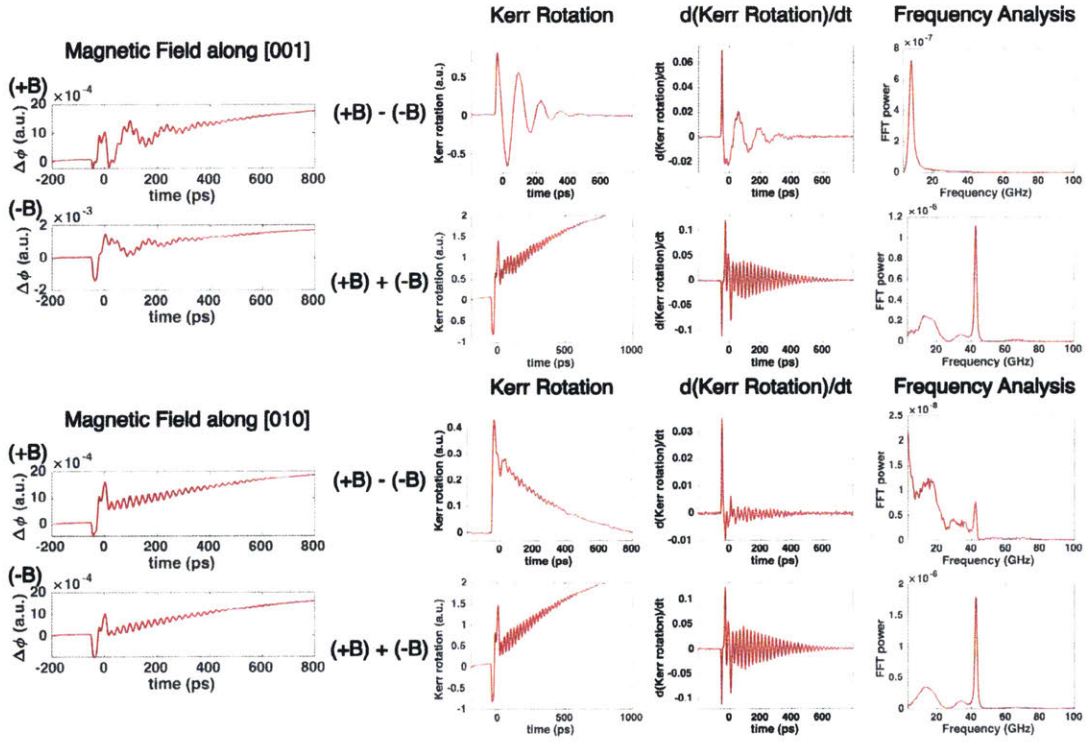

Figure 3-10: MOKE signals from the 25 nm galfenol sample measured by a 790 nm probe. The top figures are measured with an out-of-plane external magnetic field, and the bottom figures are measured with an in-plane field. In the in-plane field measurement, the 8 GHz precession signal is absent.

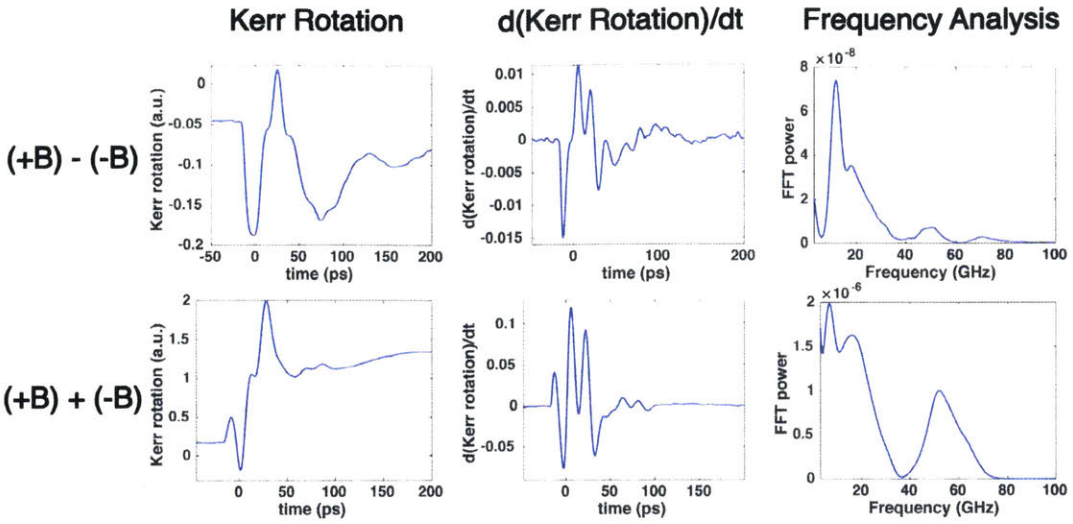

Figure 3-11: MOKE signal from 25 nm galfenol sample measured by a 395 nm probe. Unlike the 790 nm counterpart, the Brillouin oscillation is from the ZnSe capping layer instead of the GaAs substrate.

probe is shown. The easy axis [100] was aligned with the probe propagation direction, and the external magnetic field direction was varied. The top figures show the results from measurements with an out-of-plane external field along [001] direction, and the 8 GHz precession signal is clearly present, especially in the subtraction plot between two opposite external magnetic field polarities, (+B)-(-B). One thing to note here is that the time derivative of the subtraction plot shows the amplified presence of fast oscillations. As mentioned in the Chapter 2, the numerical time derivatives can amplify small variations lowering the signal-to-noise ratio. In case of the in-plane magnetic field along [010], the spin precession signal is absent. In both cases, the 43 GHz signal from Brillouin scattering in GaAs shows an interesting envelop shape. The amplitude of the Brillouin scattering oscillation maxes out at about 150 ps after the initial excitation. The Billouin oscillations were independent of the magnetic field orientation, indicating that the detected longitudinal acoustic modes were initiated by thermal expansion. For $Fe_{0.8}Ga_{0.2}$, $c_{11} = 196.0$ GPa, $c_{12} = 156.0$ GPa, and $c_{44} = 123.1$ GPa [98]. With the density of 7.42 g/cm^3, the longitudinal and shear speed of sound in galfenol is 5140 m/s and 4585 m/s, respectively. The 150 ps delay can be attributed to the counter-propagating longitudinal acoustic waves making a round trip in the

360 nm ZnSe capping layer and entering galfenol and GaAs layers.

In Figure 3-11, the spectra from the 25 nm galfenol sample measured with a 395 nm probe is presented. For 395 nm probe beam, expected Brillouin scattering frequencies for the longitudinal and shear waves are 100 GHz and 90 GHz inside the GaAs. In the Fourier analysis presented, however, the fast oscillations detected had a frequency of 52 GHz that does not agree with any modes in the GaAs at the given probe wavelength and angle. The penetration depth, $\zeta = 1/\alpha$, where α is the extinction coefficient, may account for this. The penetration depth of 395 nm beam in GaAs is 14 nm, whereas it is 683 nm for 795 nm beam [110, 111]. The detected oscillation frequency is defined even before the probe reaches the GaAs layer. The penetration depth of 790 nm beam in ZnSe is 1.4 μm, therefore the Brillouin scattering in ZnSe was unnoticeable for 790 nm probe. However, the penetration depth in ZnSe is only 69.7 nm for the 395 nm beam [110, 112]. The Brillouin scattering frequency of 52 GHz measured in this experiment matches with ZnSe substrate with 3563 m/s longitudinal speed of sound. Due to short penetration depth in ZnSe, 395 nm probe is not ideal.

3.4.2 Controlling precession

Due to the strong precession and Brillouin oscillations signals, the weak longitudinal and shear acoustic pulses from demagnetostriction are difficult to detect. To detect small signals that are otherwise buried in the noise floor, the oscillations need to be suppressed. To negate the spin precession, double-pump geometry, described in the section 3.3, was employed. Both the pump and the probe had 790 nm wavelength, and the external magnetic field was oriented normal to the sample along the |001| axis. Sixty-eight fs after the first 42.5 mW pump, the second 12 mW pump was introduced. As shown in Figure 3-12 in comparison to Figure 3-10, the amplitude of the precession signal is effectively suppressed. However, the second beam renormalized the precession and it could not be entirely removed. Another and bigger issue with this attempt was the Brillouin oscillation. To eliminate the Brillouin oscillations, the galfenol sample with a different structure was explored.

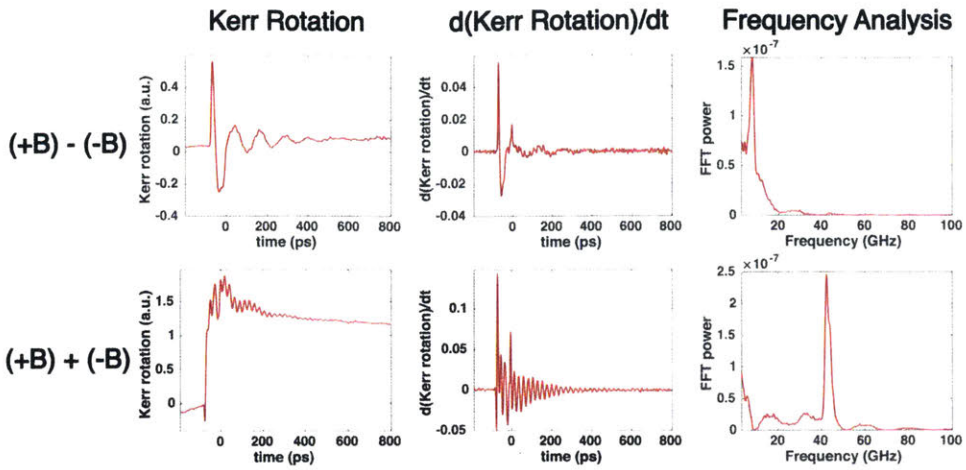

Figure 3-12: MOKE signal from a 25 nm galfenol sample pumped with two pump arms with 68 ps time separation measured by a 790 nm probe. Double pump suppressed the oscillation from the precession.

3.4.3 Detection of acoustic echoes

Instead of a thin 25 nm galfenol that lets 800 nm probe to bleed into the GaAs substrate, 92 nm galfenol sample with 6 nm of gold capping layer was used. The sample was pumped with the 71 mW, 790 nm beam and probed with the 700 μW, 395 nm probe. The sample was initially mounted with [100] easy axis aligned with the probe propagation direction. The external magnetic field was applied along the [001] out-of-plane axis. In Figure 3-13, inflection points were observed every 140 ps. The Fabry-Perot cavity effect could explain this. As a reflective interface was displaced by the arrival of an acoustic pulse, the signal amplitude shifted significantly. Considering the speed of sound of $v_L = 5140$ m/s and $v_S = 4585$ m/s, the 140 ps time delay corresponds to 720 nm or 642 nm, origin of which is still under investigation.

In another experiment, the $[1\bar{1}0]$ hard axis was aligned with the probe propagation direction and the external magnetic field was applied from the sample normal along the [001] axis. The signal did not have any coherent oscillations. Instead it contained some intriguing features. As discussed earlier in the chapter, the frame of reference and some parameters need to be adjusted for the sample rotation. The new magnetoelastic constants are given as $c'_{11} = (c_{11} - c_{12})/2 + c_{44} = 299$ GPa and $c'_{11} = (c_{11} - c_{12})/2 - c_{44} = 52.9$ GPa. In this frame, it takes 29 ps for longitudinal

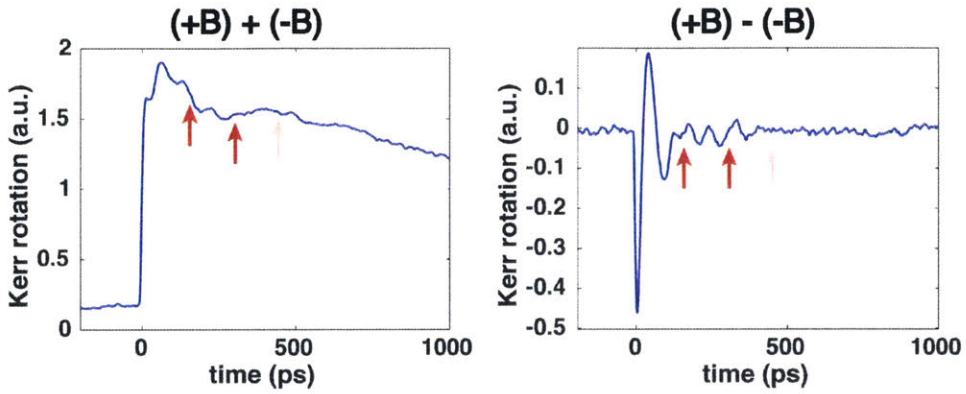

Figure 3-13: MOKE signal from 92 nm galfenol sample measured by a 395 nm probe along [100] easy axis. The resulting spectra showed inflection points every $\sim$ 140 ns. The light red mark indicates the next possible inflection point.

acoustic mode to make a 184 nm round trip to the FeGa/Buffer interface, and it takes 68 ps for shear acoustic modes. In Figure 3-14, the results are shown and contain some longitudinal (L) and shear (S) acoustic echoes. The amplitude of the echoes decreases as the result of acoustic attenuation and partial transmission through the sample interfaces. The three longitudinal echoes (L, 2L, 3L) were separated by 29 ps as expected, and showed π phase difference one after another arising from impedance mismatch. At 69 ps, a pulse with the same phase as L is observed, and it can be attributed to the shear mode (S). At 98 ps, the sum of the longitudinal and shear modes arrival time, a mode conversion was observed. Part of the longitudinal pulse L should have been converted to a shear pulse when it was reflected at the FeGa/Au/air interface. This shows that the galfenol film can be an effective transducer using the demagnetostriction effect. To confirm the result, more samples need to be tested and signal to noise ratio need to be improved.

3.5 Summary

In this chapter, a magnetostrictive material galfenol ($Fe_{1-x}Ga_x$) with 80 percent iron and 20 percent gallium was used as an acoustic transducer using demagnetostriction effect. In the thin (25 nm) galfenol sample, both spin precession and Brillouin scat-

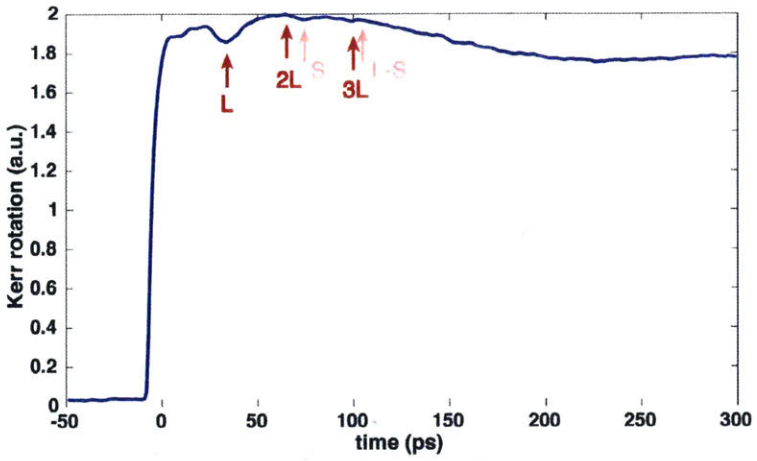

Figure 3-14: MOKE signal from 92 nm galfenol sample measured by a 395 nm probe along [$1\bar{1}0$] hard axis. The signal suggests the presence of longitudinal (L), shear(S), and mode conversion (L-S) acoustic modes.

tering were observed. The 790 nm probe could penetrate through the 360 nm ZnSe capping layer and galfenol film to record the Brillouin scattering in GaAs substrate. The 395 nm probe had short penetration depth into the ZnSe layer, and exhibited Brillouin scattering in ZnSe. Carefully designed pulse sequence was used to test the precession suppression. The presence of strong coherent oscillations from precession and the Brillouin scattering makes it hard to observe acoustic echoes. In the thick (92 nm) galfenol sample, the Fabry-Perot cavity effect and acoustic echoes were observed. The results need to be verified by testing a set of samples, and the amplitudes of the echoes over the background signal need to be improved. Galfenol has a strong magnetostriction in a relative small saturation field ($\sim$0.1 T) and the Curie temperature of 973 K. Additionally, its robustness and ease of growing optically smooth surface makes it an optimal transducer for ultrafast magneto-acoustics.

Chapter 4

Phonon Lifetime in InGaN/GaN superlattices

4.1 Strained piezoelectric superlattice

A semiconductor superlattice is an excellent model system for studying coherent acoustic phonons. By controlling the periodicity of the superlattice, one can control the period of acoustic phonons generated, thus dictating the frequency of the phonons [70]. Traditional picosecond ultrasonics with a thin metal film for generation and detection of coherent acoustic phonons were limited by slow energy transfer to the lattice due to electron-phonon coupling. However, with the help of nanofabrication techniques developed for nanoparticles and semiconductor structures with less than nanometer roughness, the generation of THz acoustic phonon became accessible.

While a layer of semiconductor with single nanometers thickness can generate broadband acoustic pulses encompassing THz frequencies, a periodic structures can produce higher signals at well defined frequencies [113, 114]. The artificial periodicity in superlattice structures introduces a zone folding in the mini-Brillouin zone, enabling detection of coherent acoustic phonons through acoustic deformation-mediated modulation of interband transitions or through the inverse piezoelectric effect [70, 115, 116]. The effective optical constants of the superlattice structure change due to the acoustic oscillations, and the resulting changes in reflection or transmission of the probe light

can show the coherent acoustic phonon presence in the structured material during time dependent measurements [117, 118].

In this chapter, InGaN/GaN multiple quantum wells with different sample structures, thicknesses, and roughness were tested to measure THz acoustic phonon lifetime in each setting. Wurtzite GaN and InN along (0001) c-axis orientation has a large piezoelectric constraint coming from lattice mismatch (a_{GaN} = 0.3189 nm, c_{GaN} = 0.5185 nm, a_{InN} = 0.3544 nm, c_{InN} = 0.5703 nm) [119–121]. The compressional strain in the structure results in a piezoelectric field, which can be released upon photoexcitation as a set of counter-propagating acoustic waves.

4.2 Optical generation and detection of coherent acoustic phonon in piezoelectric multiple quantum well

The detailed explanations of the laser generation and detection of acoustic waves in InGaN/GaN superlattices have been reported in the literature. A time-dependent Hartree-Fock approach with many-body Coulomb interaction was used to explain generation of electrons and holes from ultrafast photo excitation, and the generation of longitudinal acoustic phonons was described with a loaded string model [118], which was supported by experimental results [67]. The coherent acoustic phonons can be treated as macroscopic elastic waves, since coherent acoustic phonons have a high degree of temporal coherence. The optical absorption of the multiple quantum wells change by the acoustic phonons through both piezoelectric and deformation couplings, while dominated by the piezoelectric coupling through the quantum-confined Franz-Keldysh effect [117, 122, 123].

The generation of the coherent acoustic oscillations is initiated by piezoelectric field screening. When above-bandgap photons are absorbed by the quantum wells, the large piezoelectric field in the lattice causes electrons and holes to spatially separate, screening the preexisting field. The sudden change in the piezoelectric field perturbs mechanical equilibrium through piezoelectric and deformation potential couplings,

described by:

$$T_i = C_{ij}S_j - e_{ki}E_k + \delta_i \sum_{v=e,h} d_v \rho_v \tag{4.1}$$

$$D_i = \varepsilon_i E_i + e_{ij}S_j. \tag{4.2}$$

Here, T_i is the stress tensor, S_j is the strain tensor, D_i is the electric displacement, and E_i is the electric field. C_{ij}, ε_i, e_{kj} are the stiffness, dielectric, and piezoelectric constants. d_v and ρ_v are the deformation potential constants and carrier densities of electrons and holes. The delta function, δ_i, is 1 for i = 1, 2, 3 and 0 for i = 4, 5, 6 signifying that deformation potential coupling only applies to the diagonal parts of the stress tensor. As the quantum wells relax to a new inhomogeneous equilibrium, coherent acoustic phonons are launched [117, 118]. While the piezoelectric coupling and deformation potential can both contribute to the generation of acoustic phonon, the effect from the piezoelectric contribution is dominant [67, 118]. It has also been reported that deformation potential can only contribute to longitudinal waves. On the other hand, the effective piezoelectric tensor direction can be tuned by the angle between the c-axis and the growth direction, in effect tuning the ratio between the longitudinal and transverse acoustic phonons generated [124]. In this work, the c-axis was the propagation direction such that only the longitudinal acoustic wave was generated.

The existence of coherent longitudinal acoustic phonon causes shifts in the resonant wave vector, which changes the optical absorption of the multiple quantum well structure. The change in probe transmission, $\Delta T/T$ can be expressed with a sensitivity function:

$$\left(\frac{\Delta T}{T}\right)_{LA}(t) = \int_{-\infty}^{\infty} dz S_3(z,t) F(z;\omega), \tag{4.3}$$

where S_3 denotes strain amplitude of a small volume element along the c-axis and $F(z) = -\delta\alpha_i/\delta S_3$ is the weighted strain contribution to transmission change. The absorption constant in ith layer α_i for a perturbing strain S_3 changes in accordance

with $\alpha_i = (\delta\alpha_i/\delta S_3)S_3$, resulting in a constant value of the sensitivity function in each layer of multiple quantum wells [35, 117]. Detailed calculations, reported by references [117] and [118], show that the piezoelectric coupling is the dominating factor in the system sensitivity function, significantly changing optical transmission when the strain pulse travels through the wells.

4.3 Sample preparation and characterization methods

In the Nitride Materials and Devices Laboratory at the University of Houston, $In_{0.2}Ga_{0.8}N$ /GaN superlattice structures were grown on double-side-polished sapphire substrate with a 5 μm thick GaN template using a custom built molecular beam epitaxy tool. After a 100 nm GaN buffer layer was introduced, desired sample structures were grown with varying numbers of layers, roughness, and GaN spacer thicknesses, by modulating the shutters for In and Ga while the substrate was exposed to the N plasma. The superlattice stacks were capped by a 120 nm thick GaN layer with surface roughness of about 0.9 nm over 1 μm^2 and 4 nm over 10 μm^2. The prepared samples were monitored by scanning electron microscopy (SEM) and tapping-mode atomic force microscopy (AFM).

The structural integrity of the samples was characterized by scanning transmission electron microscopy (STEM) at the Center for Nanophase Material Science Division of Oak Ridge National Laboratory and by high resolution x-ray diffraction at the Energy Research Park of the University of Houston. The samples were ground and milled for imaging with atomic resolution STEM. The x-ray diffraction measurement was performed with Cu $K_{\alpha 1}$ radiation with 1.540 Å wavelength, and the diffracted beam was optimized with a triple bounce analyzer for fine line resolution with minimal background [125].

For coherent acoustic phonon measurements, amplified Ti:Sapphire laser pulses with 790 nm wavelength, 200 fs pulse width, and 250 kHz were split into pump and

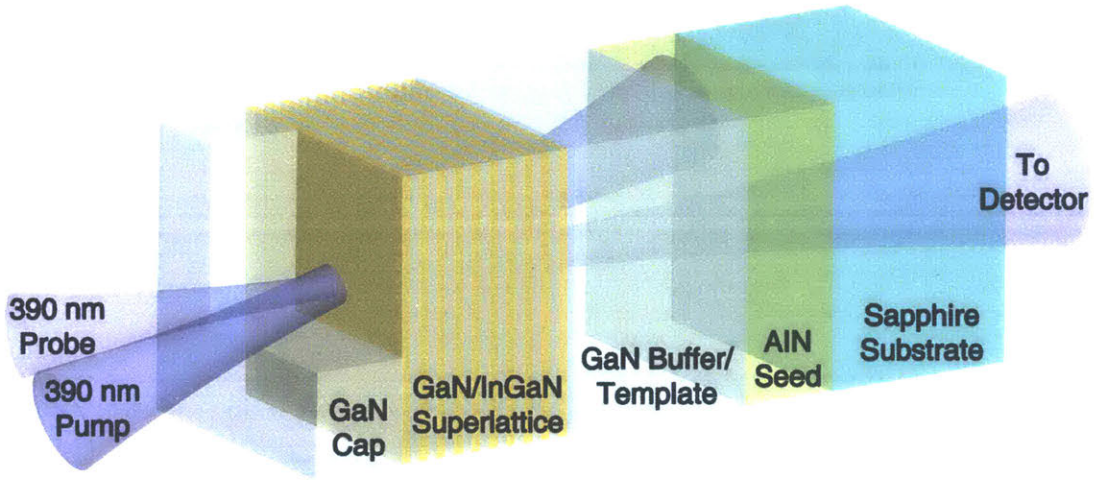

Figure 4-1: Out-of-scale sample structure and beam geometry. The probe beam is introduced at normal incidence and transmitted through the sample, while the pump is introduced at a 20 degree angle.

time delayed probe, which then were frequency doubled. The 395 nm wavelength has a photon energy above the bandgap of $In_{0.2}Ga_{0.8}N$ but below the bandgap of GaN. The excitation beam with 0.1 μJ pulse energy was modulated at 93 kHz using an acousto-optic modulator and was focused on to the sample with a spot size of 90 μm. The pump had incident angle of 20° off normal incidence to provide spatial separation between pump and probe transmitted through the sample. The probe was split into reference and probe for balanced detection. The probe with 3.6 nJ energy was focused onto the sample with 25 μm diameter, with the center overlapped with that of the pump beam. The incidence angle separation could introduce time separation of up to 25 fs across the probe beam, but the effect should be negligible considering the pulse duration and period of the generated phonon mode.

4.4 Surface specularity and phonon dispersion

The first structure of interest had 25 periods of 4 nm $In_{0.2}Ga_{0.8}N$ / 4 nm GaN sandwiched between GaN cap and GaN substrate. When the pump beam arrives at the multiple-quantum-well structure, acoustic phonons are simultaneously generated from each $In_{0.2}Ga_{0.8}N$ layer and get launched into both the cap and substrate, where they

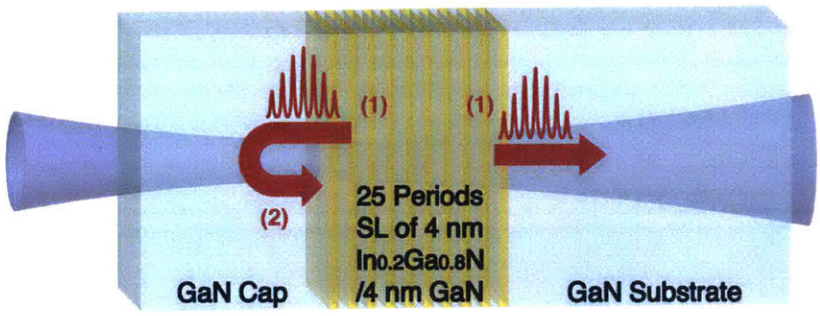

Figure 4-2: THz coherent acoustic phonons are launched in both c-axis directions. The wavepacket gets reflected at the GaN substrate-air interface and measured when it enters the superlattice again after a time delay.

travel along the c-axis at 8020 m/s [126]. After about 34 ps of time delay, another set of coherent acoustic phonon signals is observed as shown in Figure 4-3. The wavepacket launched toward the cap is measured again when it gets reflected from the free surface and transverses back into the multiple-quantum-well, while there are no reflected acoustic phonons measured from the substrate side. The effective capping layer thickness can be estimated as 136 nm. The lifetime of THz phonons in GaN substrate will be discussed in Section 4.6. This was the first demonstration of a specular reflection of THz acoustic phonons from a free surface.

After subtracting the slow background dominated by the electronic response, the acoustic oscillations in Figure 4-3 are analyzed. The number of acoustic periods in each wavepacket matched with the number of superlattice periods. After the initial wavepacket generation, the transmitted probe intensity oscillates and the oscillation intensity decreases linearly as the wavepacket propagates away from the multiple quantum-well structure. When it reappears after the reflection, the number of periods doubles and the shape of the measured signal shows a diamond-shape profile, as the rectangular wavepacket propagates through the superlattice. In Figure 4-3, reflected signal shows the broadening of the wavepacket indicating the free surface roughness.

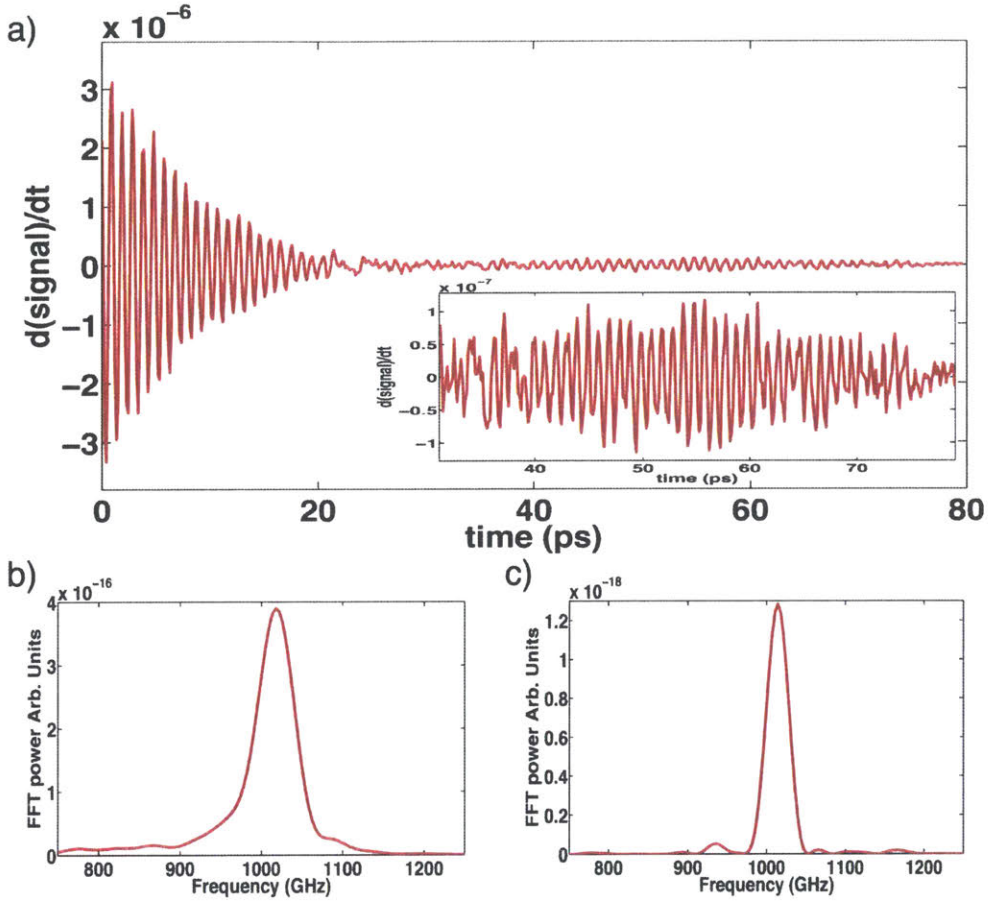

Figure 4-3: (a) Background subtracted signal with an inset of signal from reflected wavepacket. (b) and (c) show Fourier transforms of initial and reflected responses.

Figure 4-4: InGaN/GaN superlattices with 100 periods were prepared to launch THz coherent acoustic phonons in both c-axis directions. The wavepacket gets reflected at the GaN substrate-air interface and measured when it enters the superlattice again after a time delay.

4.5 THz phonon lifetime within superlattices

Next, two structures with 100 periods of 4 nm $In_{0.2}Ga_{0.8}N$ / 4 nm GaN were prepared with different uniformity of GaN periods by modulating Ga flux intensity. Increase in plasma density reduces the diffusion length of adsorbed Ga and forms rougher growth front [127]. The overall uniformity of each InGaN/GaN double layer was controlled by InGaN growth. Using z-contrast scanning transmission electron microscopy under high-angle annular dark field mode, cross section images of the samples with smooth and rough InGaN/GaN interfaces were captured. The dark strips correspond to GaN layers, while the light ones are InGaN layers. Close inspection of the superlattice period thicknesses revealed that the periodicity changed due to the non-uniformity in GaN layer. The smooth sample had period thickness of 8.08 nm $\pm$ 0.75 nm, while the rough sample had period thickness of 6.17 nm $\pm$ 0.84 nm. Even though the roughness of GaN layers was different between two samples, the roughness was not repeated or increased cumulatively across the periods as can be seen from Figure 4-5.

The Figure 4-6 shows the x-ray diffraction pattern from the two samples. The signal from the diffraction was normalized based on the $Al_2O_3(006)$ peak. The black solid curve is for the smooth sample, and the red dotted curve is for the rough sample. One thing to note is that there is an extra SL(-2) peak at 31.89 degrees for the smooth sample, which can be attributed to the uniformity difference between the two. Change in the diffraction peaks was consistent with previously reported x-ray diffraction study of superlattice interfaces, where roughness was introduced through

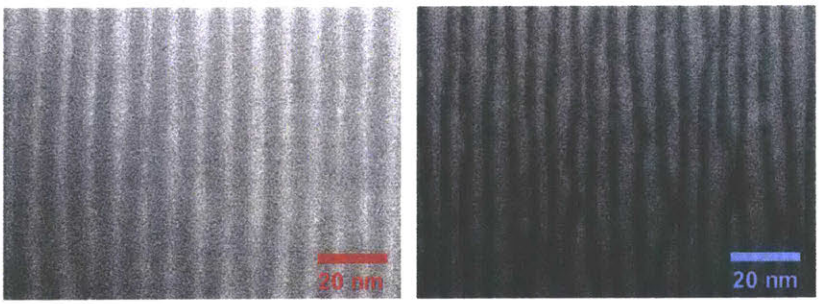

Figure 4-5: STEM images of superlattices with smooth (left) and rough (right) GaN layers. The light strips are InGaN, and the dark strips are GaN.

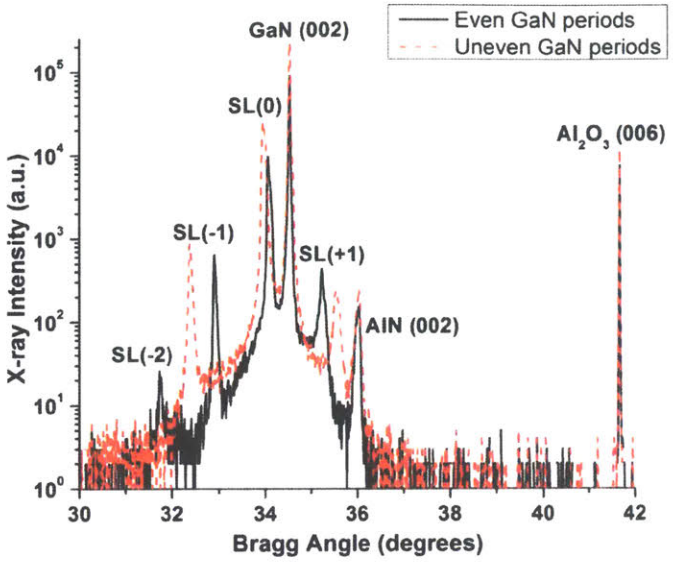

Figure 4-6: (002) $\omega - 2\theta$ scan of GaN, InGaN, and AlN and (006) scan for the sapphire substrate. The black solid curve representing smooth sample has an extra SL (-2) satellite peak over the red dotted curve representing the rough sample, demonstrating that the sharper interfaces yield higher overtones of the fundamental multiple quantum well wavevector.

annealing at 1000 ^{o}C [128].

In Figure 4-7, the photoacoustic measurement results are shown. Since the acoustic impedances and velocities in GaN and InGaN are closely matched, scattering losses at the interfaces are expected to be small. However, the coherent acoustic phonon signal would decrease significantly, if the layer periodicity does not match closely from layer to layer. Also, rough generation fronts could contribute to the strong damping of the acoustic response. From (a) and (c) the decay time of the acoustic oscillations measured at 1/e level is about 50 ps in the smooth sample while the decay time was about 6 ps in the rough sample, an order of magnitude difference. From (b) and (d), the Fourier spectra show that the frequencies of the observed coherent phonon are significantly different, 1.0 THz for the smooth sample and 1.3 THz for the rough sample. Even though the thicknesses were supposed to be identical between the smooth and rough samples, the roughness control resulted in 25% thinner GaN layers in the rough sample, as seen through the TEM measurement. This average period thickness

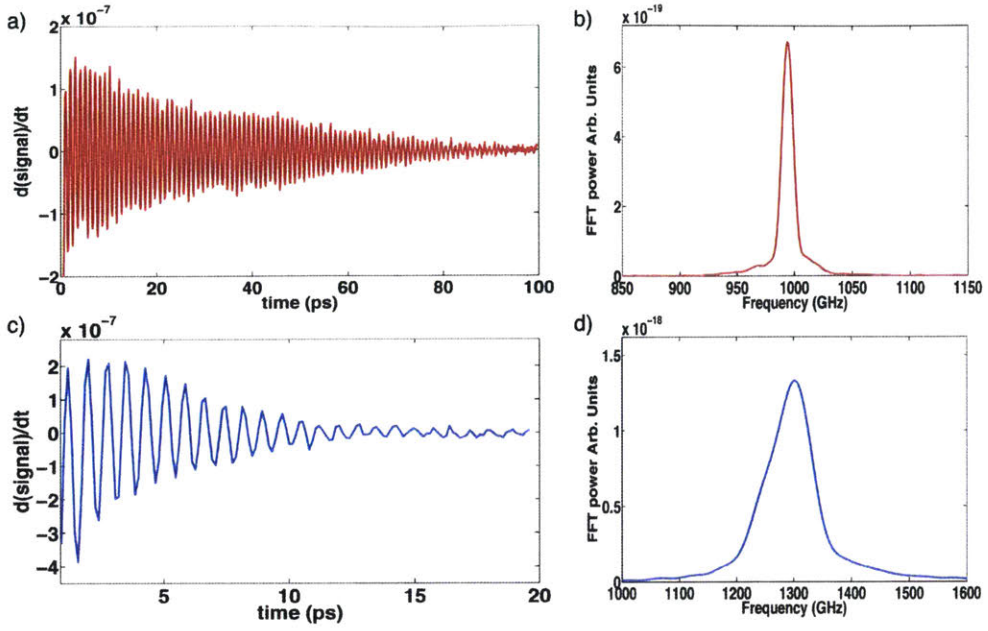

Figure 4-7: The transient probe transmission change (a) and (b), and frequency analysis through Fourier transformation (c) and (d) for superlattices with smooth and rough GaN layers. The red curves is for smooth layers, while the blue curve represents the rough layers result.

difference is also reflected in the phonon frequency. Also, the Fourier spectrum for the rough sample was much broader.

Noninvasive, non-contact photoacoustic measurement of layered structures has been demonstrated to be an effective and sensitive tool to test layer thickness uniformity. The tunneling electron microscopy can present a clear picture of the roughness, however the imaging process involves time-consuming and destructive preparation steps. X-ray diffraction is not invasive, but it is difficult to evaluate the non-uniformity from small variation in the peaks. Therefore, photoacoustics can be uniquely valuable in assessing homogeneity of multi-layer semiconductor structure fabrication process, such as the ones used for LEDs, laser diodes, and quantum cascade lasers.

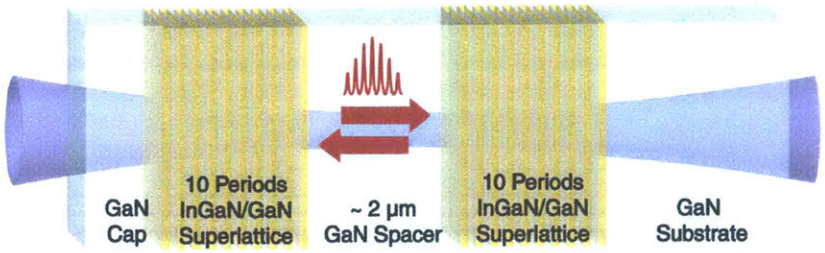

Figure 4-8: InGaN/GaN superlattices with two sets of 10 periods. The GaN spacer between the two were varied for THz acoustic phonon lifetime determination.

4.6 THz phonon lifetime in GaN spacer

Finally, structures with a spacer between superlattices were fabricated and tested. Pairs of multiple quantum wells with 10 periods of 2.7 nm $In_{0.2}Ga_{0.8}N$ / 2.7 nm GaN were fabricated with varying spacer thicknesses of 0.5 μm, 1 μm, 2 μm, and 3 μm between them. The corresponding phonon frequency was 1.4 THz. For the 2 μm structure, another sample with 4 nm $In_{0.2}Ga_{0.8}N$ / 4 nm GaN was prepared generating 1.06 THz oscillation. The acoustic phonons were generated and launched from each of the multiple quantum wells, and probed after they traveled across the spacer, to measure the lifetime of THz coherent acoustic phonons in GaN. The maximum distance between the first and the last layers of the InGaN was about 3.16 μm, which corresponds to about 10 femtosecond timing difference for excitation from the pump beam as it propagated through the structure. This difference in time is equivalent to 84 picometer structural irregularities. This difference is negligible considering the $\sim$ picosecond period of the acoustic waves and about 0.8 nm irregularities in the periodicity. Since phonon mediated thermal transport plays a crucial role in thermal management of GaN based devices, phonon lifetime in GaN will be studied in this section.

4.6.1 THz phonon lifetime measurement with variable spacer thickness

The counter propagating wavepackets with rectangular envelopes were detected through transmission changes as shown in earlier experiments. Based on the speed of sound of 8020 m/s, the spacer thicknesses of the 1.4 THz structures were 0.55 μm, 1.1 μm, 2.3 μm, and 3.4 μm. The spacers were 10 percent thicker across the board than targeted thickness. By comparing the Fourier transform amplitude between the initial and transmitted wavepackets, the attenuation of the acoustic wave from traveling through the GaN spacer can be calculated. The attenuation of the acoustic wave is given by:

$$\alpha(\omega) = \frac{1}{d_s} ln \left[\frac{\Delta R_1(\omega)}{\Delta R_2(\omega)} \right] \tag{4.4}$$

where d_s is the spacer thickness, R_1 and R_2 are the peak values of the Fourier transformation [124]. Based on the Fourier analysis shown in Figure 4-10 and equation 4.4, the average attenuation was 6.5 μm^{-1}, and the average lifetime was 23 ps for 1.4 THz coherent acoustic phonons. The results from the four samples, however, had large deviation from each other. Also, they deviated significantly from the expected value of 400 ps obtained from theoretical calculations [129, 130]. Another approach was taken to find the phonon life time in GaN. The values of $\ln\left(\frac{R_2}{R_1}\right)$ for the increasing spacer thicknesses were -5.7, -7.7, -12, and -11. From the relationship $\ln\left(\frac{R_2}{R_1}\right) = -2.2x - 5.5$, the attenuation was calculated to be 0.46 μm^{-1} and the lifetime was 270 ps, which was in better agreement with the theoretical calculation. The measurements are influenced by attenuation in the structures themselves or at the boundaries. Therefore, comparing the attenuation results from different spacer thicknesses could partly correct for the intrinsically low measured lifetime value.

The lifetime of THz phonons was measured using a set of structures with double superlattices with spacers in between. This approach has great potential to build a phonon lifetime library for semiconductors at frequencies that were nearly inaccessible. However this method suffered significantly from the fact that each sample was grown separately. As seen in Section 4.5, unexpected small variations during fabri-

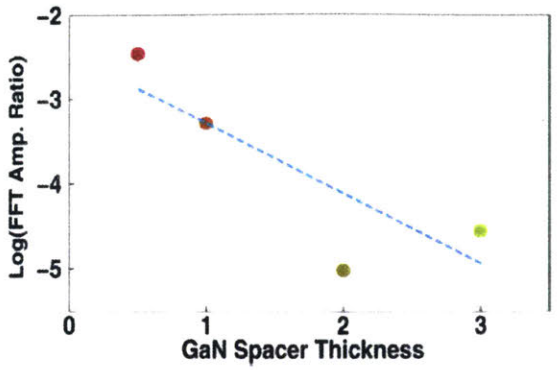

Figure 4-9: Fourier transform amplitude ratio between the initial and transmitted wavepacket at 1.4 THz frequency with varying spacer thicknesses.

cation process could result in misleading lifetime estimate. The low signal to noise ratio toward the higher spacer thickness also hindered precise measurement at thicker spacer samples.

4.6.2 Frequency dependent THz phonon lifetime in 2 μm GaN spacer

Further testing of the double superlattice structures was conducted at the National Taiwan University by a team led by C.-K. Sun. They have used a system with frequency doubled Ti:Sapphire oscillator with a 76 MHz repetition and about 200 fs pulse length at 404 nm wavelength, which falls below bandgap of GaN but above band gap of $In_{0.2}Ga_{0.8}N$. The spot size for both the pump and probe was 15 μm, and the pump power was 0.5 nJ and probe pulse was 0.05 nJ. During this investigation higher signal to noise ratio achieved by frequency filtering showed a total of four acoustic signals. The first and the third signals correspond to those shown in the Section 4.6.1. The second and fourth signals come from wavepackets reaching the free surface between the GaN cap and air and returning as depicted in Figure 4-11 [130].

For this testing, two samples with 2 μm spacers were tested. The amplitude of the fourth signal compared to the third was smaller as seen in the Figure 5-1. The squared ratio of the Fourier transform peak was found to be 0.21 for 1.06 THz sample, and it reflected the surface specularity and additional crossing of InGaN/GaN

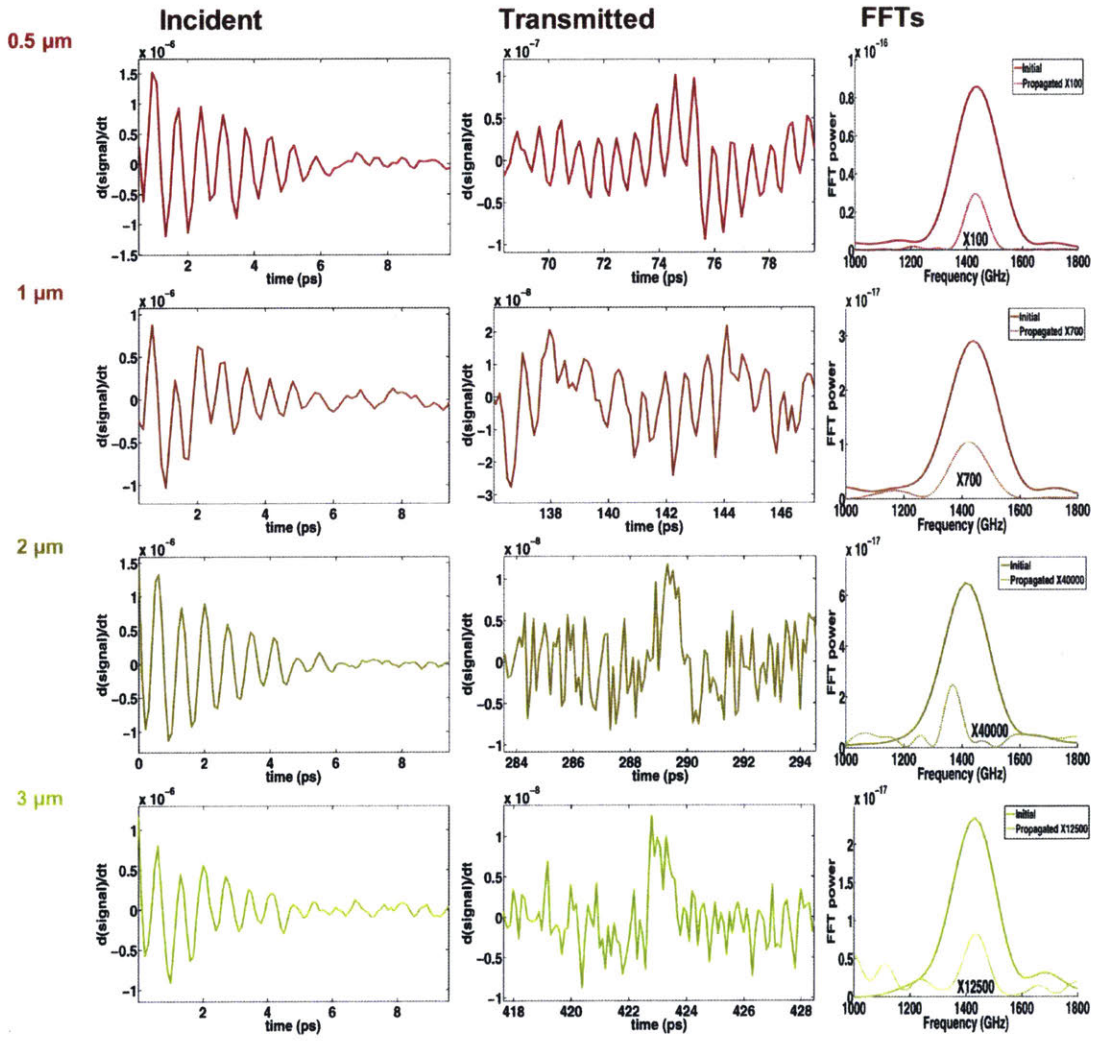

Figure 4-10: Initial and transmitted acoustic signals with the Fourier transforms for double InGaN/GaN multiple quantum well structures with a GaN spacer of 0.5 μm, 1 μm, 2 μm, and 3 μm. The effective spacer thickness can be estimated as well as the lifetime of 1.4 THz longitudinal acoustic phonons in GaN.

boundaries. To quantify the losses from the propagation in GaN, the first and the third signals were compared. The amplitude is bigger in the first tone burst, but the third tone burst has longer duration such that ideally they should have the same Fourier transform peak. The attenuation was, therefore, calculated from the Fourier transform peak amplitude ratio:

$$\frac{A_3}{A_1} = exp\left(-\frac{T_d}{2\tau}\right), \tag{4.5}$$

where T_d is the delay between the tone bursts and τ is the phonon lifettime. The 1/2 factor comes from the fact that the phonon lifetime is 1/e decay for energy not amplitude. The calculation based on the above equation resulted in 136 $\pm$ 20 ps for 1.06 THz and 55 $\pm$ 7 ps in 1.4 THz samples, which was significantly shorter than predicted by calculations as shown in the Figure 4-13. This sensitivity measurement, however, could be significantly affected by the layer thickness nonuniformity expressed by:

$$\frac{A_3}{A_1} = exp\left(-\frac{k^2\sigma^2}{22}\right), \tag{4.6}$$

where k is the phonon wavevector and σ is the root mean square deviation of the spacer thickness. It would only take thickness nonuniformity of σ = 1.9 nm and 2.1 nm for 1.06 THz and 1.4 THz, if the attenuation only came from the thickness variations. Therefore the observed phonon lifetimes should be considered lower bounds, and more experiments should follow to separate these factors [130].

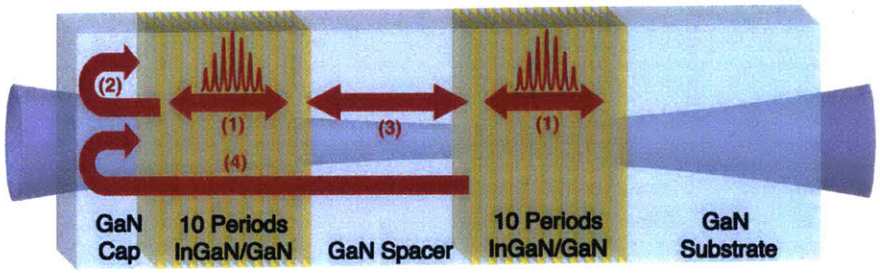

Figure 4-11: The sample structure schematic with labels indicating the sequential order of detection. The arrows indicate the path that acoustic wavepackets take before the detection. The numbers marked here match the labels in Figure 5-1.

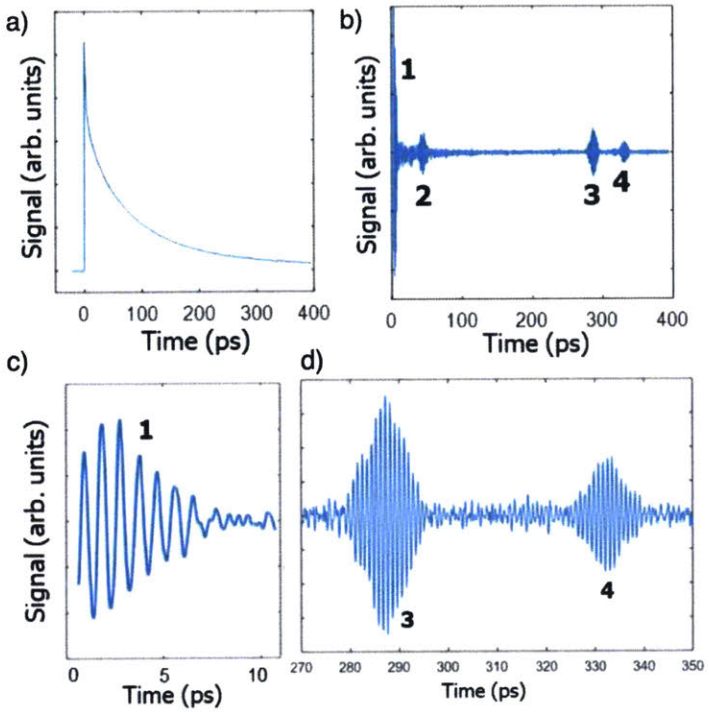

Figure 4-12: Signal from the 1.06 THz sample. (a) shows the raw signal with slow electronic response. (b) is the processed signal with the background subtracted. (c) and (d) are the zoom-ins of initial and transmitted acoustic signals (adapted from [130]).

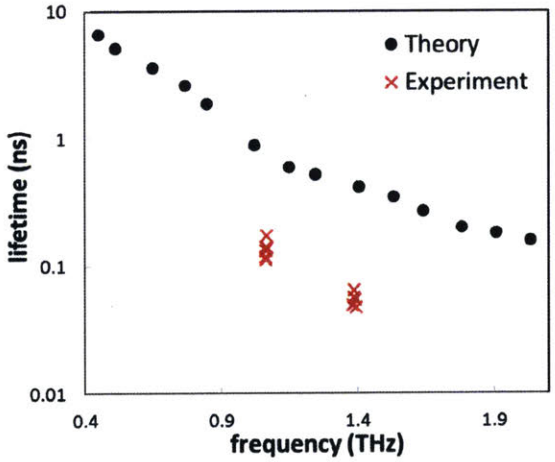

Figure 4-13: The experimental results compared to the ab-initio longitudinal acoustic phonon lifetime in wurtzite GaN at 300 K along the c axis (adapted from [130]).

4.7 Summary

In this chapter, strained piezoelectric semiconductor superlattices were used to generate THz acoustic phonons and to study THz phonon properties in GaN based structures. During the investigation of the lifetime of up to a 1.4 THz frequency acoustic phonons, specular reflection from an air/GaN free surface was observed. To use these high frequency phonons for liquid experiments, impedance matching layers may be introduced between the GaN/InGaN structure and liquid sample. The photoexcitation of THz acoustic phonons in layered structures with nanometer scale irregularities was introduced as an effective tool to investigate the integrity of the fabrication process. The roughness introduced during the fabrication process was effectively probed. Unlike SEM or TEM that are only surface sensitive or limited to ultra-thin layers, the lifetime and bandwidth measurement of phonons in the layered structure was shown to be a noninvasive and sensitive tool to test the layered structure quality, applicable for semiconductor industries. Finally, the lifetime of THz phonons in GaN was determined by using double superlattice structures. There are still challenges like separating extrinsic factors like interface roughness or thickness nonuniformity within the probe spot, but it is shown that the intrinsic losses within GaN do not hinder the study of acousto-electronic devices in the THz range. Overall, the experiments with piezoelectric superlattices opened many possibilities for studying mechanical properties and thermal phonons, which previously were only accessible though molecular dynamics simulations.

Chapter 5

Electron-Phonon Coupling and Thermal Transport

5.1 Electron-phonon coupling

In this chapter, the thermal conductivity change due to carrier-phonon interactions will be discussed. While thermal transport is mostly mediated by electrons in metals, phonons carry most of the heat in semiconductors and insulators [131]. Previously, theoretical studies have shown that the lattice thermal conductivity can be reduced by electron-phonon interactions when the carrier concentration is above 10^{19} cm^{-3} [132, 133]. There are many scattering events including impurity scattering and electron-phonon and phonon-phonon scattering [28, 134]. To isolate the carrier contribution to the scattering events, photo-excited carriers will be generated in silicon membranes through a pulsed laser excitation.

Most studies of electron-phonon scattering have measured the effects on the electrons, i.e. on electronic relaxation dynamics. Earlier experiments studying electron-phonon interaction effects on phonons or thermal transport focused on changing the carrier concentration by either doping or electrostatic gating. However, the doping process introduced impurities that also scattered phonons, and the phonon scattering from the impurities was hard to be distinguished and isolated from the scattering from carriers [135–138]. Electrostatic gating has a few nanometers of screening length

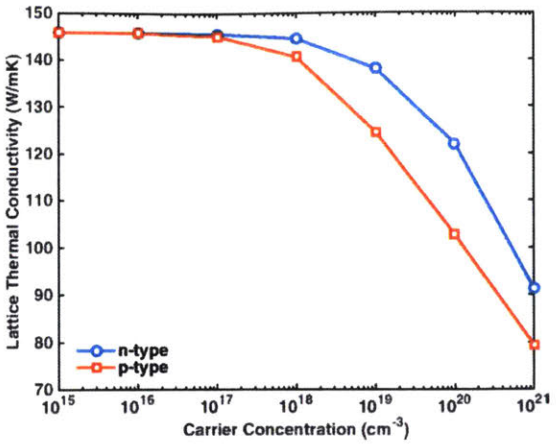

Figure 5-1: First principles calculation results showing how the lattice thermal conductivity changes as the carrier concentration increases. The calculation shown in the figure accounted for electron-phonon interactions and phonon-phonon interactions. (adopted from [132]).

that results in a short interaction time between carriers and phonons, such that the experiments were limited to cryogenic temperatures [139, 140].

For conventional electronic devices, a typical carrier concentration in a semiconductor is below 10^{19} cm^{-3}, and the carrier concentration in a metal is above 10^{22} cm^{-3}. Below 10^{19} cm^{-3} carrier concentrations, the effect of electron-phonon coupling on phonon transport is negligible. For metals with carrier concentrations of above 10^{22} cm^{-3}, phonons facilitate less than 10 percent of the thermal transport [131, 141]. However, demand for heavily-doped semiconductors rose in the thermoelectrics industry in the recent years, and the electron-phonon dynamics in materials with carrier density between 10^{19} cm^{-3} and 10^{21} cm^{-3} became relevant. Electron-phonon scattering as well as phonon-phonon scattering processes were studied with first-principles calculations by the Gang Chen Group in the Mechanical Engineering Department at MIT to provide a baseline for intrinsic lattice thermal conductivity and to evaluate the effects of electron-phonon scattering on the thermal conductivity [142, 143]. In those studies, it has been shown that the lattice thermal conductivity of silicon can be reduced by up to 45% in p-type silicon and 38% in n-type silicon by electron-phonon interactions at the carrier concentration of 10^{21} cm^{-3} [132]. Experimental tests of the theoretical results have not been reported to date.

5.2 Electron-phonon scattering of coherent acoustic phonons

In 2015, Bolin Liao of the Gang Chen group and a team of scientists conducted an experiment measuring coherent phonon lifetimes in a silicon membrane with variable carrier concentrations. In addition to a 390 nm pump pulse generating 250 GHz coherent acoustic phonons on one side of the Si membrane and a 390 nm probe pulse detecting the resulting strain pulse on the opposite side of the membrane through coherent Brillouin scattering in reflection mode, a 780 nm excitation pulse was introduced to generate carriers throughout the 1.7 μm thick membrane. While the penetration depth of 390 nm light is about 53 nm appropriate for reflection mode detection, the penetration depth at 780 nm is about 10 μm so carriers were generated nearly uniformly throughout the membrane thickness. After the pump pulse launched the acoustic wavepacket, it took about 210 ps to cross the 1.7 μm membrane where it was detected at the other side. The excitation beam was introduced at t = 260 ps from the pump-side. The excitation caused significant reductions in the subsequent signals from the acoustic wavepacket making successive round trips in the membrane, clearly indicating acoustic attenuation due to interactions with the photoexcited carriers. The results were presented in reference [144].

The experimental result showed good agreement with the theoretical calculation derived from the Fermi's Golden rule [132]:

$$\frac{1}{\tau_{qv}^{ep}} = \frac{(2\pi m^*)^{1/2} D_A^2}{(k_B T)^{3/2} g_d \rho v_s} exp\left(-\frac{m^* v_s^2}{2k_B T}\right) n\omega_{qv}, \tag{5.1}$$

where τ_{qv}^{ep} is the lifetime of phonons with wavevector q and longitudinal branch index v, m^* is the effective mass of the carriers, D_A is the acoustic deformation potential ($D_{A,e} = 5.2eV$ for electrons and $D_{A,h} = 4.8eV$ for holes), k_B is the Boltzmann constant, T is the temperature, g_d is the number of equivalent carrier pockets, ρ is the mass density, v_s is the sound velocity, n is the carrier concentration, and ω_{qv} is the angular frequency of the phonon mode. The result from the study above showed

a linear dependence between the carrier concentration and the scattering rate for the 250 GHz coherent acoustic phonons. This result motivated the study of the thermal conductivity change due to the carrier-induced phonon scattering [144].

5.3 Effect of electron-phonon coupling on thermal transport monitored with TDTR

To measure the thermal conductivity in semiconductor membranes, the time-domain thermoreflectance (TDTR) method was employed on a 2.2 μm silicon membrane with a 100 nm aluminum film deposited on the surface. TDTR directly measures heat diffusion on a nanometer length scale by tracking the temperature change on the surface [145, 146]. In this work, unconventional TDTR methods were implemented to study the electron-phonon coupling effect on thermal transport. The excitation beam that generated carriers in the silicon membrane also increased the temperature of the aluminum film, enabling the detection of the temperature change.

5.3.1 Introduction to time-domain thermoreflectance

In the TDTR method, a thin metal transducer film is deposited on top of a material of interest. Then through a time-delayed pump-probe measurement, changes in reflectivity of the transducer are recorded for a thermometry measurement. When a pump beam irradiates the metal film, absorbed energy produces a sudden jump in temperature $\Delta T_1(t)$. The change of temperature in time can be recorded through the reflectivity change, $\Delta R_1(t) = (dR/dT)\Delta T_1(t)$. Since the thermal diffusion length is much smaller than the radius of the focused pump beam, the surface temperature $\Delta T_1(t)$ can be calculated using a one-dimensional heat flow model [147, 148].

Generally in a 100 nm thin metal film, the electron temperatures becomes well-defined within 500 fs when laser photons are absorbed by the free electrons. With some variations depending on the electronic structures of transducer metal, excited electrons redistribute their energy through two major processes: ballistic electron

transport and electron-electron collisions. Ballistic electrons will travel 100 nm in 100 fs when the electron velocities are close to the Fermi velocity of about 10^6 m/s. Due to the electron mean-free-paths of 50 to 100 nm in metals, hot electrons will be distributed uniformly within 100 to 200 fs, and the electron temperature will equilibrate through electron-electron interactions within 500 fs [149–151].

The energy from electrons is transferred to the lattice through electron-phonon coupling. Energy transfer between the electrons and the lattice takes longer than electron-electron energy redistribution due to the large momentum difference between electrons and phonons [151]. In aluminum, the lattice thermalization time has been measured to be about a picosecondl. For effective heat transfer from the aluminum film into the silicon substrate, thermal energy has to be removed from all regions of the film including those near the free surface as well as those near the aluminum-silicon interface. Thus the time for heat to be transported to the silicon will be limited by the thermal diffusion time within the aluminum film, given by

$$\tau \approx \frac{d^2}{\pi^2 \alpha}, \tag{5.2}$$

where d is the film thickness and α is the thermal diffusivity. From this relationship, the time constant is about 10 to 30 ps in a 100 nm film of aluminum [147]. This is significantly shorter than the ns measurement timescale of the thermal transport within the silicon. That transport ultimately cools the aluminum layer, as measured by changes in its reflectivity.

Aluminum, the metal transducer of choice in this experiment, has unusually large thermoreflectance at the probe wavelength for Ti:sapphire laser system as seen in the Figure 5-2. For a probe around 800 nm, $dR/dT \approx 10^{-4}K^{-1}$ at room temperature. An aluminum film on the substrate can therefore be ideal for picosecond acoustics due to a high sensitivity of Al reflectivity to the strain [152]. There are two major fitting parameters for the TDTR signal: the silicon thermal conductivity κ and the thermal conductance G between the film and the sample. The challenges in fitting these two parameters at the same time will be discussed later in the chapter.

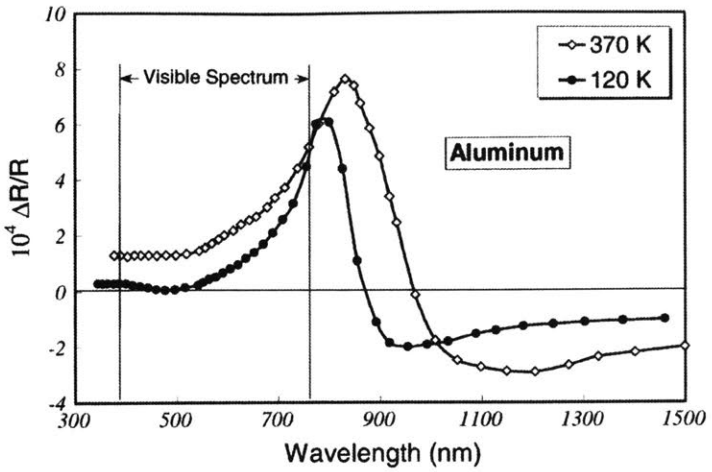

Figure 5-2: Thermoreflectance spectrum of aluminum at 370 K and 120 K. (adopted from [153])

5.3.2 Back-side pump TDTR

To introduce photo-excited carriers in the silicon membrane, a three-beam geometry, similar to that in the study discussed in Section 5.2, was introduced. The 790 nm beam from the Ti:sapphire laser had a pulse width of 200 fs at 250 kHz repetition rate with 4 μJ pulse energy. The beam was split into the pump and probe beams, and the probe was time-delayed using a mechanical delay stage that spans about 6.5 ns. After the pump arm was sent through a BBO crystal, about 20 percent of the beam was frequency doubled to generate a 395 nm pump. Using a dichroic filter, the beam from the BBO crystal was split into the fundamental frequency excitation arm and the frequency-doubled pump arm. The 395 nm pump came in from the front (aluminum) side for a conventional TDTR geometry along with the 790 nm probe. The pump scatter was spectrally filtered out from the probe. From the back (silicon) side, the 790 nm excitation beam with variable power was introduced to generate carriers as depicted in Figure 5-3 (a). The penetration depth of 790 nm excitation beam is about 10 μm appropriate for generating carriers nearly uniformly throughout the 2.2 μm Si sample. Photons from the excitation pulse can traverse through the membrane and back within 15 femtoseconds so the carrier generation throughout the thickness can be considered essentially simultaneous.

The experimental scheme, however, was revised to a two-beam geometry due to a strong absorption at 790 nm as well as at 395 nm in the aluminum transducer. Applying both the 395 nm pump and the 790 nm excitation beam resulted in double thermal stimuli on the aluminum film, so the 395 nm pump beam was removed to reduce complications in thermal modeling. The photon absorption efficiency used for the carrier generation was about 30 percent. To acquire the absorption coefficient, a region on the silicon substrate was protected during the aluminum deposition, and the transmission and reflection of the excitation beam in this aluminum-free area was measured. The excitation beam induced an instantaneous temperature rise in the Si of up to 10 K after each pulse and a steady-state temperature rise of up to 20 K at the 250-kHz laser repetition rate.

Figure 5-4 shows normalized raw data from TDTR measurements. There is a sharp initial change in the reflectivity from electronic and temperature responses. The excitation beam also generated coherent phonon wavepackets with echoes observed about every 540 picoseconds, which corresponded to the time for phonons to travel 2.2 μm back and forth. The signal decayed more slowly with increasing pump fluence, indicating lower thermal conductance in the silicon membrane, which is in agreement with predictions that higher carrier concentration would scatter the heat-carrying phonons resulting in lower thermal conductivity. For quantitative analysis, the decay curve was fit to a model developed in the Gang Chen group for calculating thermal conductivity and interface conductance [154]. The results are shown in Figure 5-5.

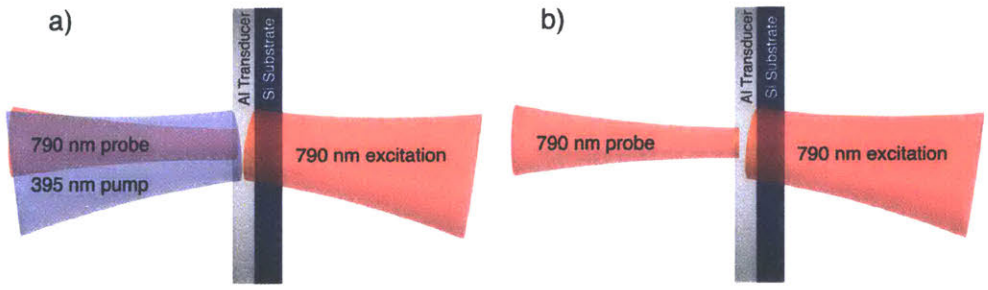

Figure 5-3: Beam geometry of the TDTR measurement. Initially, a 395 nm pump was introduced to initiate temperature change in the Al film as shown in (a). A 790 nm excitation beam was later used for both the generation of carriers and the thermal excitation.

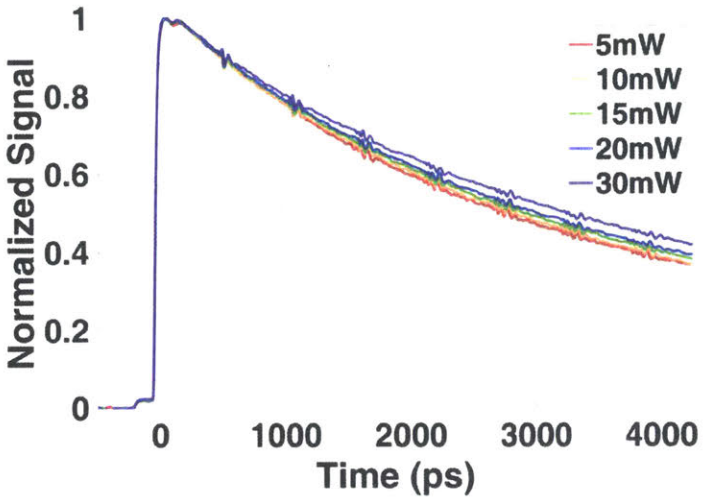

Figure 5-4: Raw signal from the TDTR measurement. As the power of the excitation increases, the normalized signal decays more slowly, indicating that the increase in carrier density resulted in lower thermal conductivity.

Only the decay curve from the 1000 ps after the excitation was used for the model fitting to avoid any influence from the fast responses in the transducer discussed earlier. The carrier lifetime is about 10 ns in a silicon membrane with a carrier density of about $10^{19} cm^{-3}$ at room temperature [155–157]. Therefore, the photoinduced carriers were present throughout the measurements.

Due to nonlinear pump-power effects in the sample, the maximum excitation power used for the experiment was 25 mW, and the corresponding carrier density was $4 \times 10^{19} cm^{-3}$. The power was converted to carrier density, n, by:

$$n = \alpha \frac{E}{\hbar\omega} \frac{1}{\pi d r^2}, \tag{5.3}$$

where α is the absorption coefficient, ω is the photon frequency, d is the substrate thickness, and r is the radius of the beam. The laser pulse energy, E, was acquired from the power of the laser excitation beam, P, and the modulation frequency, f_{mod}, by the relationship $E = P/f_{mod}$. The measured thermal conductivity at a given carrier density was compared to a prediction by the DFT calculation and plotted in the Figure 5-6. The carrier density estimation had about 30 percent margin of error,

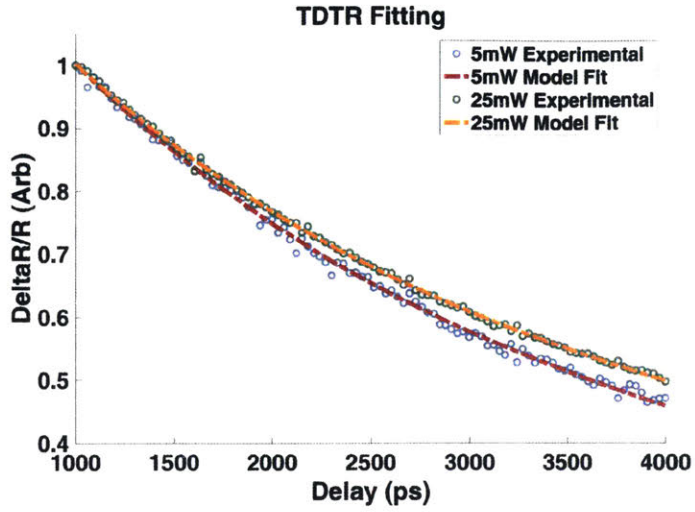

Figure 5-5: TDTR experimental and model data. The thermal decay curves were fit to a model to calculate the thermal conductivity and interface conductance. Only the data from $\geq$ 1000 picoseconds after excitation were used to avoid any effects from fast electronic responses in the Al layer.

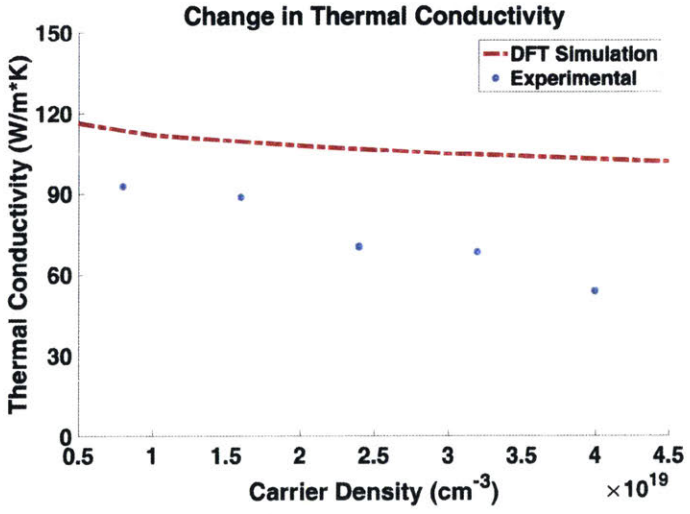

Figure 5-6: Comparison between the measured thermal conductivity in 2.2 μm silicon and DFT calculation. The measured thermal conductivity had a downward trend with increasing carrier concentration in qualitative agreement with the theory, but the measured values changed significantly more than the simulated results.

and the thermal conductivity fitting had about 10 $W/m \cdot K$ margin of error. The thermal conductivity decreased with increasing carrier concentration as expected, but the changes in the measured values were significantly larger than those predicted by the DFT calculations. In TDTR experiments, the measured thermal conductivity value is usually about 10 to 20 percent lower than the calculated value due to other scattering events from the surface, interfaces, and structural imperfections such as dopants and vacancies. However, the difference between the two observed in this study was significantly larger especially with high carrier concentration.

5.3.3 Challenges in the fitting thermal conductivity

Analogous to a mismatch in optical refractive indices causing optical reflection at an interface, the difference in densities and speeds of sound result in an acoustic impedance mismatch for an interface between dissimilar materials. In the acoustic-mismatch model with an assumption that scattering due to interface imperfections is absent, the transmission coefficient t_{AB} for phonons coming to the interface at normal incidence is:

$$t_{AB} = \frac{4Z_A Z_B}{(Z_A + Z_B)^2}, \tag{5.4}$$

where $Z = \rho c$ is the acoustic impedance for materials A and B respectively, and c and ρ are the speed of sound and the mass density respectively. In the diffuse mismatch model, phonons scatter at the interface to one side or the other with a probability proportional to the density of states [158]. However, in addition to these factors, it has been demonstrated that interface contamination can have a large effect on the transmission of the phonons [148, 158, 159].

To model the TDTR thermal decay curves, there are two main fitting parameters: thermal conductivity of the substrate and interface conductance between the substrate and the transducer. For this study it is critical to find a precise and accurate thermal conductivity value in silicon membrane. In Figure 5-7, it is shown that small variations in interface conductance can significantly change the calculated thermal conductivity. Varying the thermal interface conductance of 74 and 84 $MW/m^2 \cdot K$, the thermal

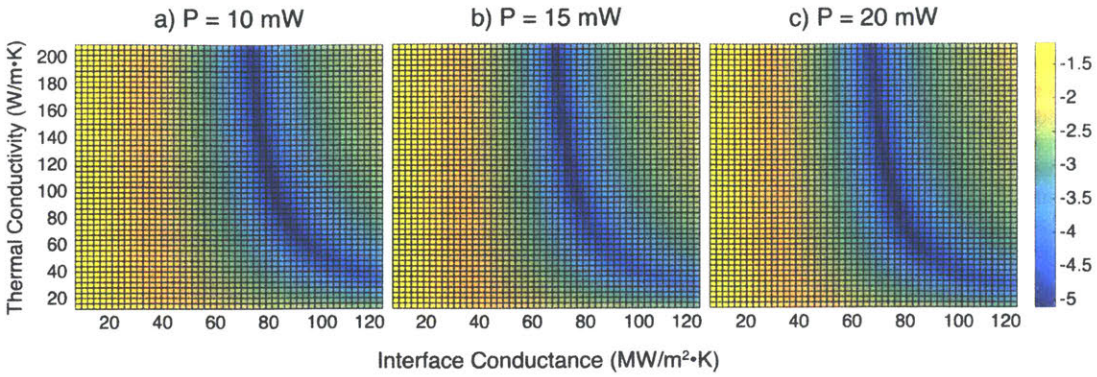

Figure 5-7: Residue plot from thermal model fitting of thermal conductivity and interface conductance with varying pump laser powers. A small variation in the interface conductance could result in a large error in the thermal conductivity.

conductivity can be found anywhere between 60 and 200 $W/m \cdot K$ with good fits to the data.

A strong acoustic echo signal is present bouncing back and forth between the silicon-air free surface and silicon-aluminum interface, as shown in the Figure 5-4. The strong presence of the echoes and their very slow attenuation indicate that the silicon-aluminum interface quality may be poor due to imperfections or contamination introduced during the aluminum deposition process [35, 160]. The effect of a poor interface conductance is shown in Figure 5-8. The simulated residue plot was based on an ideal thermal decay curve with Si thermal conductivity of 130 $W/m \cdot K$. Increasing interface conductance results in a smaller range for the thermal conductivity fit. When the interface conductance is as high as 500 $MW/m^2 \cdot K$, the target value of 130 $W/m \cdot K$ becomes the only viable fit. If the aluminum film deposition process is improved to increase the interface conductance, a more precise measurement of the thermal conductivity reduction due to electron-phonon scattering is expected.

In this section, an investigation of the electron-phonon scattering effect on the thermal conductivity through TDTR measurements was discussed. Thermal conductivity reductions were experimentally observed above a carrier density of 10^{19}cm^{-3} agreeing with the theory and the previous study of coherent acoustic phonons, but there was a large discrepancy between the experimentally measured and the first-principles-calculation values of thermal conductivity in silicon. The thin metal film

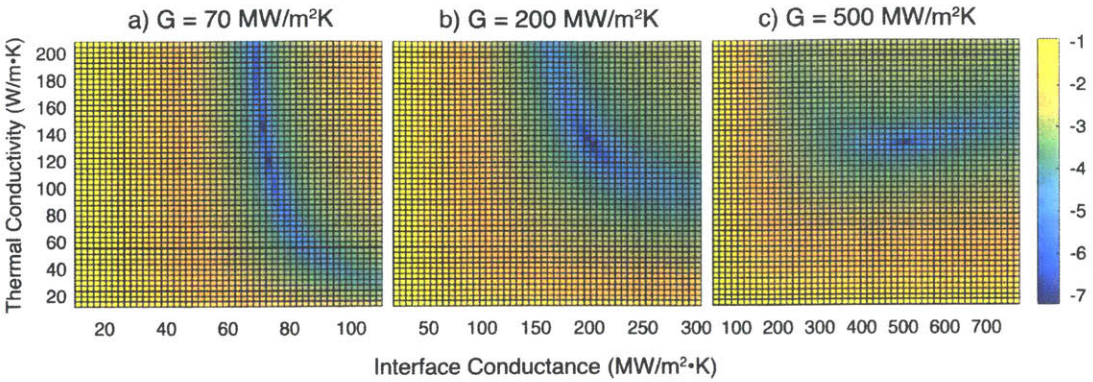

Figure 5-8: Simulated residue plot from the thermal model fitting for a fixed laser power. The thermal conductivity was assumed to be 130 $W/m \cdot K$ and the initial interface conductance was set as labeled on each plot. Increasing interface conductance decreases the thermal conductivity fitting range.

transducer is included in the modeling, but the presence of significant non-equilibrium effects can make the data ambiguous [161, 162]. In addition, the thermal boundary resistance can hinder heat flow from one material to the other [148, 163]. To eliminate the effects from the interface, transient thermal grating was used to measure the same effect in a free standing silicon membrane, as presented in the next section.

5.4 Effect of electron-phonon coupling on thermal transport monitored with TTG

To measure the thermal conductivity in free standing silicon membranes, the transient thermal grating (TTG) technique was employed in a transmission mode on 400 nm, 2 μm, and 10 μm silicon membranes and in reflection mode on bulk silicon. The goal of this chapter is to track the thermal conductivity change, therefore a slowly decaying thermal signal was obtained through an amplitude grating. Technical description of the TTG technique was introduced in Chapter 2. To optically generate free carriers in silicon, an additional excitation beam was introduced to the TTG beam geometry. In this section, further study of electron-phonon coupling effects on thermal transport is described.

5.4.1 Transient thermal grating with carrier excitation beam

In this experiment, the pump pulse was from an amplified Yb:KGW HighQ femtoRegen laser system with 1 kHz repetition rate. Typically, the system lases at 1030 nm with a 300 fs pulse. However, by bypassing the compressor, the laser output was stretched to about 60 ps. Because the thermal decay is in the nanosecond time scale, it was beneficial to avoid sample damage or unwanted nonlinear optical effects from the high peak powers. For this experiment, the pump beam was frequency-doubled using a BBO crystal. Because the BBO was optimally cut for 1064 nm instead of 1030 nm, the BBO temperature was tuned for an efficient second harmonic generation. For the probe beam, a 532 nm continuous beam from a Coherent Verdi V5 frequency-doubled Nd:YAG laser was used. To avoid unnecessary heating of the sample, the probe beam was chopped with an electro-optic modulator at 1 kHz. To achieve the TTG beam geometry, a phase mask was used for splitting both the pump and the probe, which provided passive phase stabilization and a correct angle to overlap the reference and the Bragg diffracted probe. For this experiment, a 4.25 μm period thermal grating profile was created using a phase mask and a set of imaging lenses. One of the split probe arms was attenuated with a ND filter and was used as a reference. The probe arm gets diffracted from the thermal grating produced by the crossed pump pulses, and the reference arm and superposed diffracted signal were sent to the detector to monitor the change in either transmission or reflection mode. The signal traces were recorded on a 33 GHz Digital Phosphor Oscilloscope from Tektronix.

To observe the change in the thermal conductivity from electron-phonon scattering, an excitation beam was added to the four-beam transient thermal grating geometry. An 1030 nm excitation beam was introduced 3.84 ns after the pump beams generated the thermal grating. The IR excitation beam with 450 μm spot size was overlapped with 532 nm continuous probe with 160 μm spot size. When the beams were properly aligned, there was a transient reflectivity change. The fundamental frequency of pump at 1030 nm was initially chosen as an excitation beam, because of ease of spectral separation between the excitation beam and the probe. Also, 1030 nm

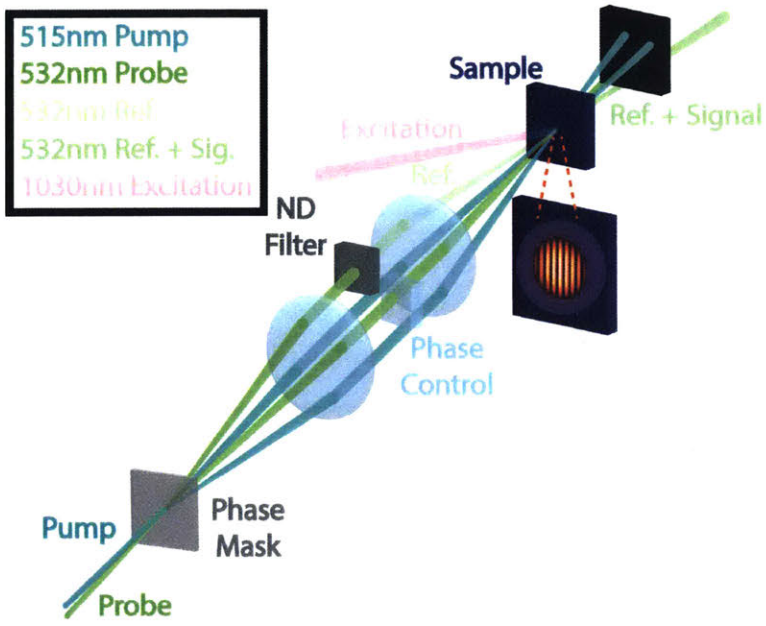

Figure 5-9: Beam geometry of the TTG setup. An excitation beam was added at 3.84 ns after the pump beam generated thermal grating. In the later experiments, the excitation beam was frequency-doubled to 515 nm.

was above the silicon bandgap of 1.1 eV, or 1127nm [164]. However, the introduction of 1030 nm excitation beam had no effect on the thermal conductivity in the 2 μm membrane, the 10 μm membrane, or the bulk silicon, as seen in Figure 5-10. The excitation beam power was increased up to the damage threshold at 150 mW, but no measurable difference in thermal conductivity was observed. As the thickness of the silicon membrane was increased, the signal started to show coherent oscillations indicating some phase grating contributions.

The same experiment was performed with a 400 nm silicon membrane. The damage threshold in this membrane was only 70 mW. When the excitation beam reached the power of 50 mW, a sizable change in the decay rate was observed. However, upon closer inspection, the sample showed nonlinear power effects to the probe as shown in Figure 5-11. When the silicon samples were exposed to the high fluence 1030 nm beam, they did not show significant change in thermal conductivity. Only nonlinear power effects were shown before a dielectric breakdown. Since the excitation photon energy (1.2 eV) was only 10 percent higher than the band gap of 1.1 eV with 341 μm

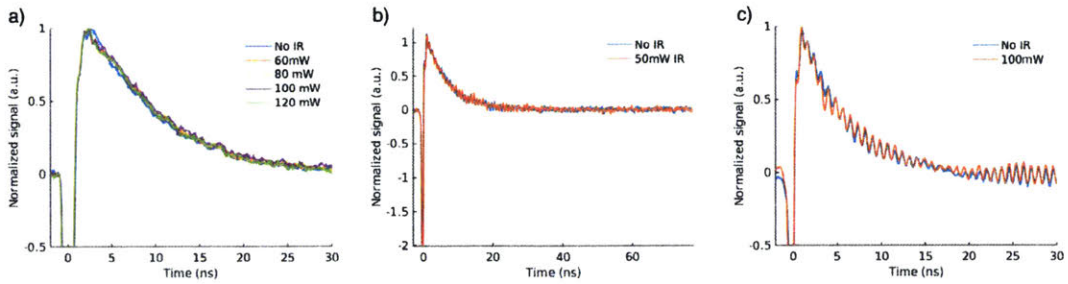

Figure 5-10: Results from the TTG experiment with the 1030 nm excitation beam in the 2 μm Si membrane (a), the 10 μm membrane (b), and bulk silicon (c). The thicker samples showed coherent oscillations even though the experiment was performed in the amplitude grating, indicating that a phase grating contribution was not completely suppressed.

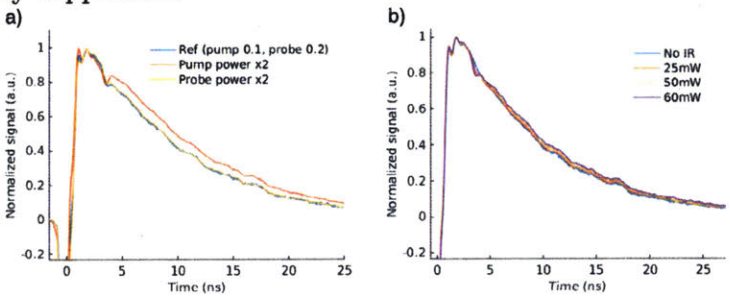

Figure 5-11: Results from the TTG experiment with the 1030 nm excitation beam in the 400 nm membrane. The data showed a fluence dependence, but it failed to pass the linearity test. The excitation power was high enough to cause a nonlinear response in the 400 nm.

penetration depth, the excitation beam wavelength was revised to 515 nm.

5.4.2 Analysis of the thermal transport

In depth analysis of the thermal grating decay is provided in reference [85]. In this section, the thermal grating decay analysis includes a finite absorption depth of the excitation light. The thermal diffusion equation describing temperature dynamics after transient grating heating on the surface of a semi-infinite sample is given by,

$$k_x \frac{\partial^2 T}{\partial x^2} + k_z \frac{\partial^2 T}{\partial z^2} = \rho c \frac{\partial T}{\partial t} + Q_0 \cos(qx) \exp(-\zeta z) \delta(t), \tag{5.5}$$

where x is the grating dimension, z is the in depth dimension, T is the temperature, ρ is density, c is heat capacity, Q_0 is the energy deposited by the laser pulse, $1/\zeta$ is the penetration depth, and k_x and k_z are the thermal conductivity components parallel and perpendicular to the sample surface respectively. The boundary conditions at the surface are given by,

$$\frac{\partial T}{\partial z}(z=0)=0 \tag{5.6}$$

$$T(z=\infty)=0. \tag{5.7}$$

Assuming a sinusoidal spatial dependence of T on x following equation 5.5 and performing a Fourier transform,

$$\frac{\partial^2 \tilde{T}}{\partial z^2}=\frac{\alpha_x q^2+i\omega}{\alpha_z}\tilde{T}+Q_0\exp(-\zeta z), \tag{5.8}$$

where $\alpha_i = k_i/\rho c$ is the thermal diffusivity. Using solutions for the homogeneous and particular solutions respectively and utilizing the boundary conditions provides the analytical frequency-domain solution as following:

$$\tilde{T}=\frac{Q_0}{\varphi^2-\zeta^2}\left(\exp(-\zeta z)-\frac{\zeta}{\varphi}\exp(-\varphi z)\right),\ \textit{where}\ \varphi=\sqrt{\frac{\alpha_x q^2+i\omega}{\alpha_z}}. \tag{5.9}$$

The time-domain solution can be recovered through numerical inverse Fourier transform [84, 85]. For time domain decay, the anlytical solution in the limit of surface heating is given by,

$$T(z=0)=A_T(\alpha_z t)^{-1/2}\exp(\alpha_x q^2 t). \tag{5.10}$$

In this case, the transient grating measurement is only sensitive to the in-plane thermal diffusivity. The in-plane thermal diffusivity can be retrieved by fitting the signal to an exponential decay. The cross-plane diffusitivy α_z only changes the amplitude A_T of the signal, but the data are normalized before fitting.

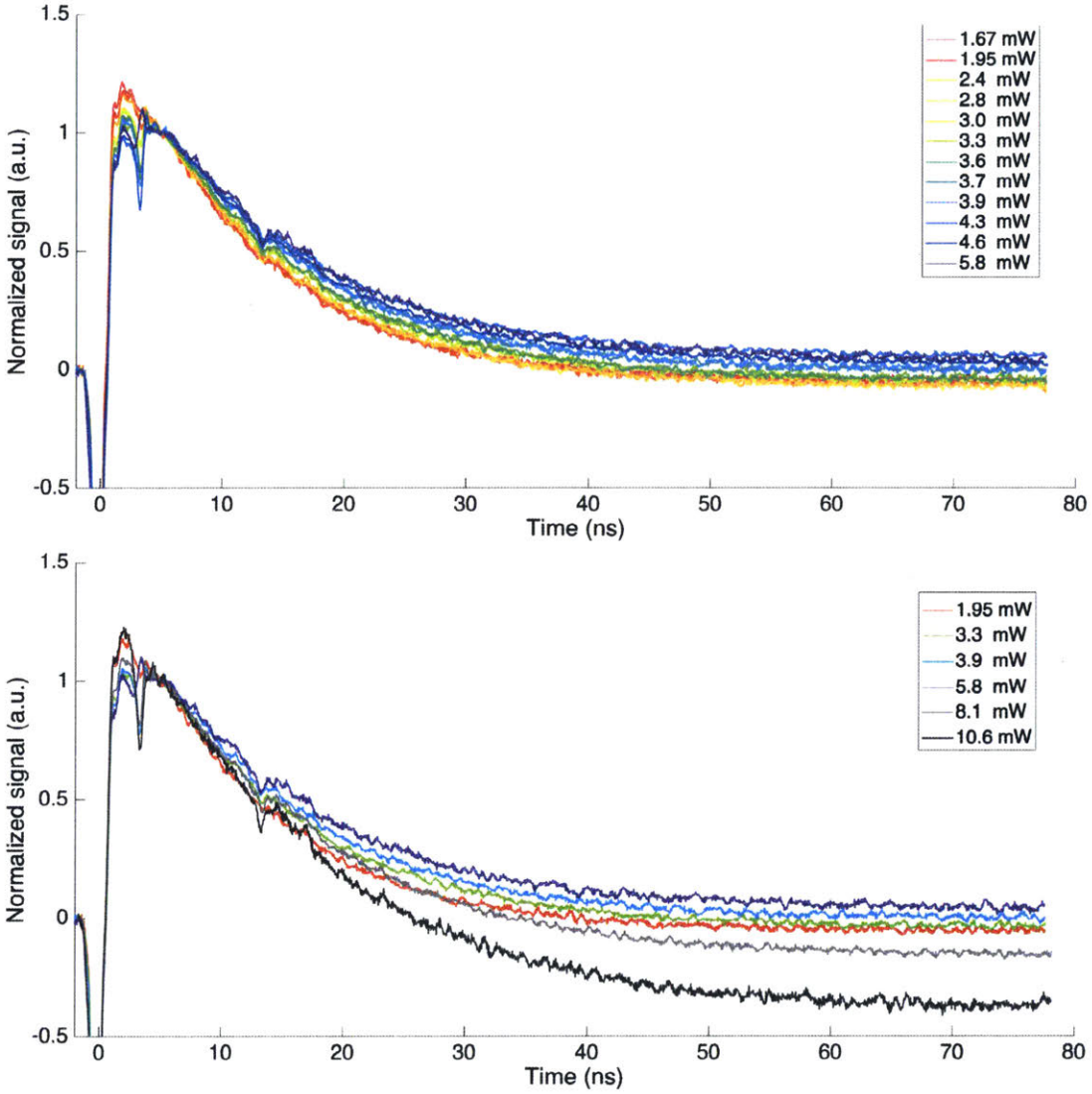

Figure 5-12: Pump fluence dependence of TTG signal. Between 1.67 mW and 5.8 mW excitation power (between 3×10^{19} and 1.2×10^{20} cm^3 carrier concentration), the thermal conductivity consistently decreases with increasing carrier concentration(top). However, when the pump power goes over 5.8 mW, the decay curves show nonlinear power dependence (bottom).

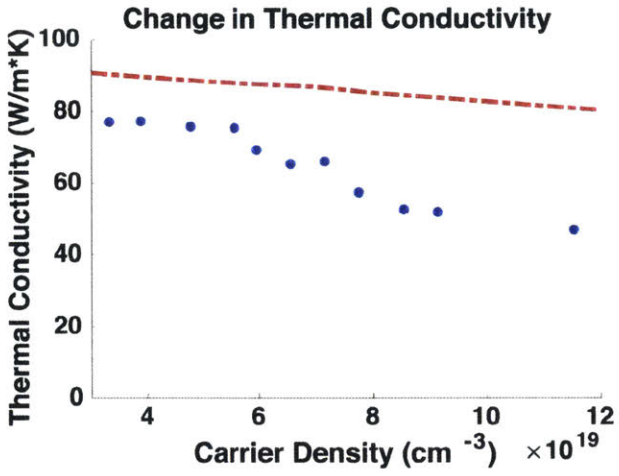

Figure 5-13: Thermal conductivity vs. carrier concentration. The experimental results (blue dots) are compared to the model (red dotted line).

5.4.3 Carrier density dependence of thermal conductivity

The experiment from the previous section was repeated with a 515 nm excitation beam. The excitation power was varied between 1.67 mW and 10.6 mW, which corresponded to the carrier concentration of 3×10^{19} and 2.7×10^{20} cm^3 respectively from equation 5.3. As seen in Figure 5-12, the thermal conductivity consistently decreased as the carrier concentration increased between the 1.67 mW and 5.8 mW excitation power. The displayed signals were normalized at 5 ns from the initial thermal profile generation. Above 5.8 mW, nonlinear responses of the material were observed. The slow decaying thermal signal decreased past zero, which is not physical and which suggests that there was already signal prior to t=0 due to cumulative effects. Another indication of a nonlinear response was the pulsating sample. The sample slowly and visibly vibrated at a low frequency due to photon pressure. Even though the sample was not irreversibly damaged, the measurement was reliable only up to 5.8 mW.

In Figure 5-13, the thermal conductivity in the 400 nm membrane is plotted against the carrier concentration. The blue dots in the figure show the experimental results. The red dotted line comes from the theoretical calculation from the Gang Chen group. The relaxation time due to boundary scattering is taken to be L/v,

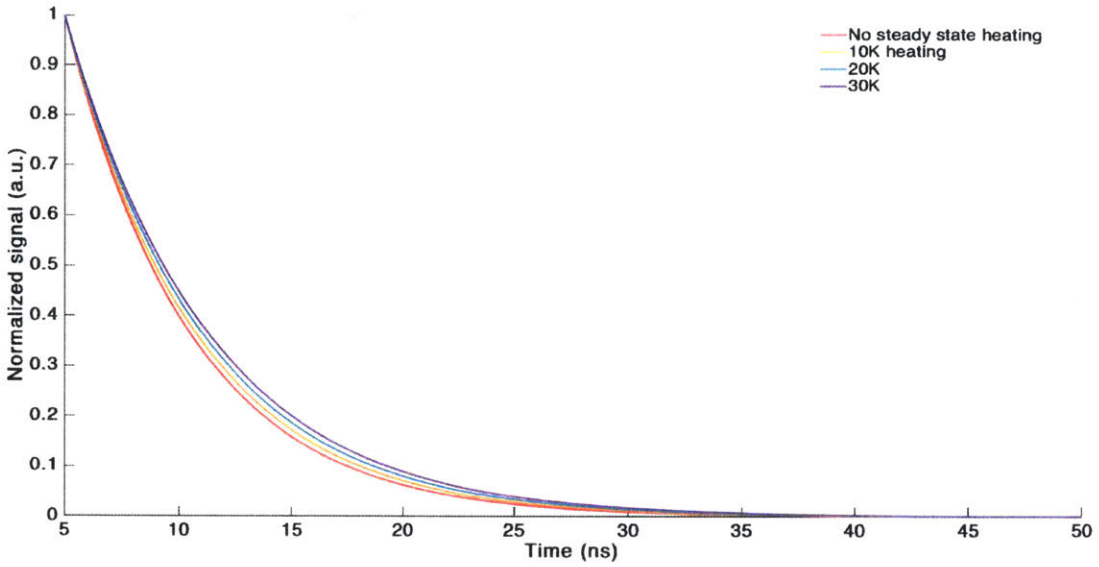

Figure 5-14: Steady state heating effect on thermal conductivity. When laser power is stored in the sample and increases the temperature of the sample, the silicon thermal conductivity decreases.

where v is the phonon group velocity. The thermal conductivity reduction due to electron-phonon scattering is evident, however the measured thermal conductivity is significantly lower than the theoretical predictions. The gap became even larger towards the higher carrier densities. Due to high fluence on the 400 nm thin film, steady state heating became a concern for the result, which will be discussed in the next section.

5.4.4 Steady state heating and thermal conductivity

When heating from the laser pulses is present, the thermal conductivity decreases. Because both the higher carrier concentration and the lattice heating decrease the thermal conductivity, while the higher laser power increases both, it is hard to disentangle the effects from the two. To verify that the thermal conductivity reduction was indeed caused by phonon scattering from carriers, different experiments need to be performed. One way to test if the thermal conductivity change was from laser heating is to introduce the excitation beam before the thermal grating generation. If the excitation beam arrives about 5 - 10 ns before the thermal grating generation, the

carriers decay away while the heating effect should persist. Another way to test this is to decrease the modulation frequency. This will increase the overall experiment time, but it decreases the steady state heating while maintaining the same signal to noise ratio. The temperature dependence of the thermal conductivity in Si is known [165]. Starting at room temperature, TTG signals with the experimental period of 4.25 μm were calculated as shown in Figure 5-14. It is clear that heating effects could be significant and need to be taken into account.

5.5 Summary

In this chapter, thermal conductivity of silicon membranes was measured with the TDTR and TTG techniques. In both cases, the optically generated carriers reduced measured thermal conductivity. In the TDTR measurements, the interface conductance between the aluminum transducer and the silicon layer became a very important variable to determine accurate absolute thermal conductivity values. Still, the relative changes in thermal conductivity due to photoexcited carriers were apparent. In the TTG measurements, it was observed that slightly above band-gap IR excitation beam was not effectively creating carriers to suppress the thermal conductivity. A frequency-doubled green excitation beam effectively decreased thermal conductivity in the 400 nm silicon membrane. The penetration depth of 515 nm beam was about 670 nm, so it was not an effective wavelength to generate carriers throughout the thicker samples. Also, the presence of steady state heating could not be easily disentangled from the carrier effect. In the future efforts could be focused on isolating the steady state effect. Also, it would be beneficial to use another wavelength excitation beam, such as the 790 nm beam used in the TDTR measurements.

List of Figures

Bibliography

[1] C. V. RAMAN and K. S. KRISHNAN, A new type of secondary radiation, Nature **121**, 501 (1928).

[2] J. D. Ferry, *Viscoelastic Properties of Polymers*, 3rd ed. (Wiley, 1980).

[3] T. Christensen and N. B. Olsen, Determination of the frequency-dependent bulk modulus of glycerol using a piezoelectric spherical shell, Phys. Rev. B **49**, 15396 (1994).

[4] T. Christensen and N. B. Olsen, A rheometer for the measurement of a high shear modulus covering more than seven decades of frequency below 50 khz, Review of Scientific Instruments **66**, 5019 (1995).

[5] U. Kaatze, R. Behrends, and K. Lautscham, Acoustic relaxation spectrometers for liquids, Ultrasonics **39**, 393 (2001).

[6] Y. Yan and K. A. Nelson, Impulsive stimulated light scattering. ii. comparison to frequency-domain light-scattering spectroscopy, The Journal of Chemical Physics **87**, 6257 (1987).

[7] L. Comez, D. Fioretto, F. Scarponi, and G. Monaco, Density fluctuations in the intermediate glass-former glycerol: A brillouin light scattering study, The Journal of Chemical Physics **119**, 6032 (2003).

[8] H. Maris, Picosecond ultrasonics, Scientific American **278**, 86 (1998).

[9] L. Comez, D. Fioretto, G. Monaco, and G. Ruocco, Brillouin scattering investigations of fast dynamics in glass forming systems, Journal of Non-Crystalline Solids **307-310**, 148 (2002).

[10] J. Wuttke, J. Hernandez, G. Li, G. Coddens, H. Z. Cummins, F. Fujara, W. Petry, and H. Sillescu, Neutron and light scattering study of supercooled glycerol, Phys. Rev. Lett. **72**, 3052 (1994).

[11] F. H. Stillinger and P. G. Debenedetti, Glass transition thermodynamics and kinetics, Annual Review of Condensed Matter Physics **4**, 263 (2013).

[12] P. Lunkenheimer, U. Schneider, R. Brand, and A. Loid, Glassy dynamics, Contemporary Physics **41**, 15 (2000).

[13] N. Petzold and E. A. Rossler, Light scattering study on the glass former o-terphenyl, J. Chem. Phys. **133**, 124512 (2010).

[14] P. Debenedetti and F. Stillinger, Supercooled liquids and the glass transition, Nature **410**, 259 (2001).

[15] K. Binder and W. Kob, *Glassy Materials and Disordered Solids : An Introduction to Their Statistical Mechanics* (World Scientific Publishing Co., Singapore, 2005).

[16] C. A. Angell, K. L. Ngai, G. B. McKenna, P. F. McMillan, and S. W. Martin, Relaxation in glassforming liquids and amorphous solids, J. Appl. Phys **88**, 3113 (2000).

[17] J. Hansen and I. McDonald, *Theory of Simple Liquids* (Elsevier, New York, 2006).

[18] W. Gotze, Recent tests of the mode-coupling theory for glassy dynamics., J. Phys.: Condens. Matter **11**, A1 (1999).

[19] D. R. Reichman and P. Charbonneau, Mode-coupling theory, J. Stat. Mech. **P05013** (2005).

[20] W. Gotze and L. Sjogren, Scaling properties in supercooled liquids near the glass transition., J. Phys. C: Solid State Phys **21**, 3407 (1988).

[21] T. Hecksher, D. H. Torchinsky, C. Klieber, J. A. Johnson, J. C. Dyre, and K. A. Nelson, Mechanical spectra of glass-formin liquids. i. broadband longitudinal spectra of the silicone oil dc704, PACS (2012).

[22] C. Klieber, T. Hecksher, T. Pezeril, D. H. Torchinsky, J. C. Dyre, and K. A. Nelson, Mechanical spectra of glass forming liquids. ii. gigahertz-frequency longitudinal and shear acoustic dynamics in glycerol and dc704 studied by time-domain brillouin scattering, J. Chem. Phys. **138**, 12A544 (2013).

[23] J. Fourier and A. Freeman, *The Analytical Theory of Heat* (The University Press, 1878).

[24] G. Nilsson and G. Nelin, Study of the homology between silicon and germanium by thermal-neutron spectrometry, Phys. Rev. B **6**, 3777 (1972).

[25] X. Wang and B. Huang, Computational study of in-plane phonon transport in si thin films, Scientific Reports **4**, 6399 EP (2014), article.

[26] N. W. Ashcroft and N. D. Mermin, *Solid state physics* (Brooks/Cole Cengage Learning Learning, 2018).

[27] J. Callaway, Model for lattice thermal conductivity at low temperatures, Phys. Rev. **113**, 1046 (1959).

[28] J. Ziman, *Electrons and Phonons: The Theory of Transport Phenomena in Solids*, International series of monographs on physics (OUP Oxford, 2001).

[29] D. A. Broido, M. Malorny, G. Birner, N. Mingo, and D. A. Stewart, Intrinsic lattice thermal conductivity of semiconductors from first principles, Applied Physics Letters **91**, 231922 (2007).

[30] A. Ward and D. A. Broido, Intrinsic phonon relaxation times from first-principles studies of the thermal conductivities of si and ge, Phys. Rev. B **81**, 085205 (2010).

[31] K. Esfarjani, G. Chen, and H. T. Stokes, Heat transport in silicon from first-principles calculations, Phys. Rev. B **84**, 085204 (2011).

[32] J. A. Johnson, J. K. Eliason, A. A. Maznev, T. Luo, and K. A. Nelson, Non-diffusive thermal transport in gaas at micron length scales, Journal of Applied Physics **118**, 155104 (2015).

[33] A. D. Pierce, *Acoustics: An Introduction to Its Physical Principles and Applications* (Springer International Publishing, 2019).

[34] R. M. White, Generation of elastic waves by transient surface heating, Journal of Applied Physics **34**, 3559 (1963).

[35] C. Thomsen, H. T. Grahn, H. J. Maris, and J. Tauc, Surface generation and detection of phonons by picosecond light pulses, Phys. Rev. B **34**, 4129 (1986).

[36] H. T. Grahn, H. J. Maris, and J. Tauc, Picosecond ultrasonics, IEEE Journal of Quantum Electronics **25**, 2562 (1989).

[37] S. A. Akhmanov and V. É. Gusev, Laser excitation of ultrashort acoustic pulses: New possibilities in solid-state spectroscopy, diagnostics of fast processes, and nonlinear acoustics, Soviet Physics Uspekhi **35**, 153 (1992).

[38] J. Israelachvili and H. Wennerström, Role of hydration and water structure in biological and colloidal interactions, Nature **379**, 219 (1996).

[39] R. G. Horn and J. N. Israelachvili, Direct measurement of structural forces between two surfaces in a nonpolar liquid, The Journal of Chemical Physics **75**, 1400 (1981).

[40] T. R. Jensen, M. Østergaard Jensen, N. Reitzel, K. Balashev, G. H. Peters, K. Kjaer, and T. Bjørnholm, Water in contact with extended hydrophobic surfaces: Direct evidence of weak dewetting, Phys. Rev. Lett. **90**, 086101 (2003).

[41] J. N. Israelachvili, Chapter 13 - van der waals forces between particles and surfaces, in *Intermolecular and Surface Forces (Third Edition)* (Academic Press, San Diego, 2011) third edition ed., pp. 253 – 289.

[42] A. Centrone, E. Penzo, M. Sharma, J. W. Myerson, A. M. Jackson, N. Marzari, and F. Stellacci, The role of nanostructure in the wetting behavior of mixed-monolayer-protected metal nanoparticles, Proceedings of the National Academy of Sciences **105**, 9886 (2008).

[43] T. Fukuma, Y. Ueda, S. Yoshioka, and H. Asakawa, Atomic-scale distribution of water molecules at the mica-water interface visualized by three-dimensional scanning force microscopy, Phys. Rev. Lett. **104**, 016101 (2010).

[44] R. Mancinelli, The effect of confinement on water structure, Journal of Physics: Condensed Matter **22**, 404213 (2010).

[45] L. Cheng, P. Fenter, K. L. Nagy, M. L. Schlegel, and N. C. Sturchio, Molecular-scale density oscillations in water adjacent to a mica surface, Phys. Rev. Lett. **87**, 156103 (2001).

[46] S. H. Khan, G. Matei, S. Patil, and P. M. Hoffmann, Dynamic solidification in nanoconfined water films, Phys. Rev. Lett. **105**, 106101 (2010).

[47] T. Mitsui, M. K. Rose, E. Fomin, D. F. Ogletree, and M. Salmeron, Water diffusion and clustering on pd(111), Science **297**, 1850 (2002).

[48] A. NOWICK and B. BERRY, Chapter 1 - characterization of anelastic behavior, in *Anelastic Relaxation in Crystalline Solids* (Academic Press, 1972) pp. 1 – 29.

[49] B. Auld, *Acoustic fields and waves in solids*, A Wiley-Interscience publication (Wiley, 1973).

[50] D. Sander, The correlation between mechanical stress and magnetic anisotropy in ultrathin films, Reports on Progress in Physics **62**, 809 (1999).

[51] E. Muybridge, Sallie gardner at a gallop (Library of Congress Prints and Photographs Division, 1878).

[52] H. Edgerton and J. James R. Killian, Milk drop coronet, in *Flash! Seeing the Unseen by Ultra-High Speed Photography* (Boston: Hale, Cushman & Flint, 1939).

[53] C. Klieber, E. Peronne, K. Katayama, J. Choi, M. Yamaguchi, T. Pezeril, and K. A. Nelson, Narrow-band acoustic attenuation measurements in vitreous silica at frequencies between 20 and 400 ghz, Applied Physics Letters **98**, 211908 (2011).

[54] D. Baddeley, C. Batram, Y. Weiland, C. Cremer, and U. J. Birk, Nanostructure analysis using spatially modulated illumination microscopy, Nature Protocols **2**, 2640 EP (2007).

[55] E. Betzig, G. H. Patterson, R. Sougrat, O. W. Lindwasser, S. Olenych, J. S. Bonifacino, M. W. Davidson, J. Lippincott-Schwartz, and H. F. Hess, Imaging intracellular fluorescent proteins at nanometer resolution, Science **313**, 1642 (2006).

[56] C. S. Shin, C. E. Avalos, M. C. Butler, D. R. Trease, S. J. Seltzer, J. P. Mustonen, D. J. Kennedy, V. M. Acosta, D. Budker, A. Pines, and V. S. Bajaj, Room-temperature operation of a radiofrequency diamond magnetometer near the shot-noise limit, Journal of Applied Physics **112**, 124519 (2012), j Appl Phys061ECTimes Cited:1Cited References Count:15.

[57] G. S. Bumbrah and R. M. Sharma, Raman spectroscopy – basic principle, instrumentation and selected applications for the characterization of drugs of abuse, Egyptian Journal of Forensic Sciences **6**, 209 (2016).

[58] C. Kittel, *Introduction to Solid State Physics*, 8th ed. (John Wiley and Sons Inc, 2004).

[59] C. Morath, G. Tas, T.-D. Zhu, and H. Maris, Phonon attenuation in glasses studied by picosecond ultrasonics, Physica B: Condensed Matter **219-220**, 296 (1996), pHONONS 95.

[60] B. Rethfeld, A. Kaiser, M. Vicanek, and G. Simon, Ultrafast dynamics of nonequilibrium electrons in metals under femtosecond laser irradiation, Phys. Rev. B **65**, 214303 (2002).

[61] G. Tas and H. J. Maris, Electron diffusion in metals studied by picosecond ultrasonics, Phys. Rev. B **49**, 15046 (1994).

[62] L. Landau and E. Lifshitz, *Mechanics*, v. 1 (Elsevier Science, 1982).

[63] R. Slayton, *Developing a transient grating technique to probe fast acoustic dynamics in liquids*, Ph.D. thesis, Harvard University (2002).

[64] C. Klieber, *Ultrafast Photo-Acoustic Spectroscopy of Supercooled Liquids*, Ph.D. thesis, Massachusetts Institute of Technology (2010).

[65] A. Bartels, T. Dekorsy, H. Kurtz, and K. Kohler, Coherent zone-folded longitudinal acoustic phonons in semiconductor superlattices: Excitation and detection, Phys. Rev. Lett. **82**, 1044 (1998).

[66] A. Yamamoto, T. Mishina, Y. Masumoto, and M. Nakayama, Coherent oscillation of zone-folded phonon modes in gaas-alas superlattices, Phys. Rev. Lett. **73**, 5 (1994).

[67] G.-W. Chern, K.-H. Lin, Y.-K. Huang, and C.-K. Sun, Spectral analysis of high-harmonic coherent acoustic phonons in piezoelectric semiconductor multiple quantum wells, Phys. Rev. B **67**, 121303 (2003).

[68] K. H. Lin, H. H. Tsai, K. J. Wang, S. H. Chen, K. L. Chi, J. W. Shi, P. C. Chen, and J. K. Sheu, Acoustic spectroscopy for studies of vitreous silica up to 740 ghz, AIP Adv **3**, 072126 (2013).

[69] A. Maznev, K. J. Manke, K.-H. Lin, K. A. Nelson, C.-K. Sun, and J.-I. Chyi, Broadband terahertz ultrasonic transducer based on a laser-driven piezoelectric semiconductor superlattice, Ultrasonics **52**, 1 (2012).

[70] C.-K. Sun, J.-C. Liang, and X.-Y. Yu, Coherent acoustic phonon oscillations in semiconductor multiple quantum wells with piezoelectric fields, Phys. Rev. Lett. **84**, 179 (2000).

[71] H. N. Lin, R. J. Stoner, H. J. Maris, and J. Tauc, Phonon attenuation and velocity measurements in transparent materials by picosecond acoustic interferometry, Journal of Applied Physics **69**, 3816 (1991).

[72] J. W. Goodman, ed., Acousto-optics, in *Fundamentals of Photonics* (John Wiley and Sons, Ltd, 2001) Chap. 20, pp. 799–831.

[73] C. Klieber, D. Torchinsky, T. Pezeril, K. Manke, S. Andrieu, and K. A. Nelson, High frequency longitudinal and shear acoustic waves in glass-forming liquids, Journal of Physics: Conference Series **214**, 012033 (2010).

[74] A. A. Maznev, F. Bencivenga, A. Cannizzo, F. Capotondi, R. Cucini, R. A. Duncan, T. Feurer, T. D. Frazer, L. Foglia, H.-M. Frey, H. Kapteyn, J. Knobloch, G. Knopp, C. Masciovecchio, R. Mincigrucci, G. Monaco, M. Murnane, I. Nikolov, E. Pedersoli, A. Simoncig, A. Vega-Flick, and K. A. Nelson, Generation of coherent phonons by coherent extreme ultraviolet radiation in a transient grating experiment, Applied Physics Letters **113**, 221905 (2018).

[75] D. W. P. Hans Joachim Eichler, Peter Gunter, *Laser-Induced Dynamic Gratings*, 0342-4111 (Springer, Berlin, Heidelberg, 1986).

[76] J. Nye and P. Nye, *Physical Properties of Crystals: Their Representation by Tensors and Matrices*, Oxford science publications (Clarendon Press, 1985).

[77] L. Landau, E. Lifshitz, A. Kosevich, J. Sykes, L. Pitaevskii, and W. Reid, *Theory of Elasticity*, Course of theoretical physics (Elsevier Science, 1986).

[78] J. A. Rogers, Y. Yang, and K. A. Nelson, Elastic modulus and in-plane thermal diffusivity measurements in thin polyimide films using symmetry-selective real-time impulsive stimulated thermal scattering, Applied Physics A **58**, 523 (1994).

[79] Y. Yang and K. A. Nelson, Impulsive stimulated thermal scattering study of alpha relaxation dynamics and the debye-waller factor anomaly in ca0.4k0.6(no3)1.4, The Journal of Chemical Physics **104**, 5429 (1996).

[80] B. Berne and R. Pecora, *Dynamic Light Scattering: With Applications to Chemistry, Biology, and Physics*, Dover Books on Physics (Dover Publications, 2013).

[81] J. A. Johnson, A. A. Maznev, M. T. Bulsara, E. A. Fitzgerald, T. C. Harman, S. Calawa, C. J. Vineis, G. Turner, and K. A. Nelson, Phase-controlled, heterodyne laser-induced transient grating measurements of thermal transport properties in opaque material, Journal of Applied Physics **111**, 023503 (2012).

[82] A. A. Maznev, K. A. Nelson, and J. A. Rogers, Optical heterodyne detection of laser-induced gratings, Opt. Lett. **23**, 1319 (1998).

[83] R. Collier, *Optical Holography* (Elsevier Science, 2013).

[84] J. A. Johnson, *Optical Characterization of Complex Mechanical and Thermal Transport Properties*, Ph.D. thesis, Massachusetts Institute of Technology, Cambridge, MA 2011 (2011).

[85] O. W. Käding, H. Skurk, A. A. Maznev, and E. Matthias, Transient thermal gratings at surfaces for thermal characterization of bulk materials and thin films, Applied Physics A **61**, 253 (1995).

[86] M. Gibbs, *Modern Trends in Magnetostriction Study and Application*, Nato Science Series II: (Springer Netherlands, 2000).

[87] J. J. Esq., Xvii. on the effects of magnetism upon the dimensions of iron and steel bars, The London, Edinburgh, and Dublin Philosophical Magazine and Journal of Science **30**, 76 (1847).

[88] E. Villari, Ueber die aenderungen des magnetischen moments, welche der zug und das hindurchleiten eines galvanischen stroms in einem stabe von stahl oder eisen hervorbringen, Annalen der Physik **202**, 87 (1865).

[89] G. Petculescu, R. Wu, and R. McQueeney, Chapter three - magnetoelasticity of bcc fe–ga alloys (Elsevier, 2012) pp. 123 – 226.

[90] S. Legvold, J. Alstad, and J. Rhyne, Giant magnetostriction in dysprosium and holmium single crystals, Phys. Rev. Lett. **10**, 509 (1963).

[91] J. J. Rhyne and S. Legvold, Magnetostriction of tb single crystals, Phys. Rev. **138**, A507 (1965).

[92] A. E. Clark, B. F. DeSavage, and R. Bozorth, Anomalous thermal expansion and magnetostriction of single-crystal dysprosium, Phys. Rev. **138**, A216 (1965).

[93] A. Clark, Chapter 15 magnetostrictive rfe2 intermetallic compounds, in *Alloys and Intermetallics*, Handbook on the Physics and Chemistry of Rare Earths, Vol. 2 (Elsevier, 1979) pp. 231 – 258.

[94] E. Beaurepaire, J.-C. Merle, A. Daunois, and J.-Y. Bigot, Ultrafast spin dynamics in ferromagnetic nickel, Phys. Rev. Lett. **76**, 4250 (1996).

[95] Y. Xu, M. Deb, G. Malinowski, M. Hehn, W. Zhao, and S. Mangin, Ultrafast magnetization manipulation using single femtosecond light and hot-electron pulses, Advanced Materials **29**, 1703474 (2017).

[96] A. E. Clark, K. B. Hathaway, M. Wun-Fogle, J. B. Restorff, T. A. Lograsso, V. M. Keppens, G. Petculescu, and R. A. Taylor, Extraordinary magnetoelasticity and lattice softening in bcc fe-ga alloys, Journal of Applied Physics **93**, 8621 (2003).

[97] R. O'Handley, *Modern Magnetic Materials: Principles and Applications* (Wiley, 1999).

[98] R. A. Kellogg, *Development and modeling of iron-gallium alloys*, Ph.D. thesis, Iowa State University (2003).

[99] Y. Du, M. Huang, S. Chang, D. L. Schlagel, T. A. Lograsso, and R. J. Mcqueeney, Relation between ga ordering and magnetostriction of fe-ga alloys studied by x-ray diffuse scattering (2010).

[100] O. Ikeda, R. Kainuma, I. Ohnuma, K. Fukamichi, and K. Ishida, Phase equilibria and stability of ordered b.c.c. phases in the fe-rich portion of the fe–ga system, Journal of Alloys and Compounds **347**, 198 (2002).

[101] C. Hepburn, *Dynamic Interplay between Magnetization and Surface Acoustic Waves in Magnetostrictive Fe(1–x) Ga(x) Thin Films*, Ph.D. thesis, UNIVERSITE PIERRE ET MARIE CURIE (2018).

[102] J. Coey and J. Coey, *Magnetism and Magnetic Materials*, Knovel Library (Cambridge University Press, 2010).

[103] H. Kronmuller and S. Parkin, *Handbook of magnetism and advanced magnetic materials. Novel techniques for characterizing and preparing samples*, edited by Chichester, Vol. 3 (Wiley-VCH, 2007).

[104] J.-Y. Bigot, M. Vomir, and E. Beaurepaire, Coherent ultrafast magnetism induced by femtosecond laser pulses, Nature Physics **5**, 515 EP (2009), article.

[105] T. Parpiiev, *Ultrafast Magneto-Acoustics in Magnetostrictive Materials*, Ph.D. thesis, Le Mans Universite (2017).

[106] T. Lahtinen, *Ferromagnetic-ferroelectric domain coupling in multiferroic heterostructures*, Ph.D. thesis, Aalto University (2013).

[107] O. Matsuda, O. B. Wright, D. H. Hurley, V. E. Gusev, and K. Shimizu, Coherent shear phonon generation and detection with ultrashort optical pulses, Phys. Rev. Lett. **93**, 095501 (2004).

[108] A. K. Ganguly, K. L. Davis, D. C. Webb, and C. Vittoria, Magnetoelastic surface waves in a magnetic film–piezoelectric substrate configuration, Journal of Applied Physics **47**, 2696 (1976).

[109] D. Fritsch and C. Ederer, First-principles calculation of magnetoelastic coefficients and magnetostriction in the spinel ferrites $cofe_2o_4$ and $nife_2o_4$, Phys. Rev. B **86**, 014406 (2012).

[110] M. Polyanskiy, Refractive index database, Website (2008).

[111] G. Jellison, Optical functions of gaas, gap, and ge determined by two-channel polarization modulation ellipsometry, Optical Materials **1**, 151 (1992).

[112] S. Adachi and T. Taguchi, Optical properties of znse, Phys. Rev. B **43**, 9569 (1991).

[113] Y.-C. Wen, S.-H. Guol, H.-P. Chen, J.-K. Sheu, and C.-K. Sun, Femtosecond ultrasonic spectroscopy using a piezoelectric nanolayer: Hypersound attenuation in vitreous silica films, Applied Physics Letters **99**, 051913 (2011).

[114] C.-C. Shen, M.-Y. Weng, J.-K. Sheu, Y.-T. Yao, and C.-K. Sun, In situ monitoring of chemical reactions at a solid–water interface by femtosecond acoustics, The Journal of Physical Chemistry Letters **8**, 5430 (2017), pMID: 29058902.

[115] A. Bartels, T. Dekorsy, H. Kurz, and K. Köhler, Coherent zone-folded longitudinal acoustic phonons in semiconductor superlattices: Excitation and detection, Phys. Rev. Lett. **82**, 1044 (1999).

[116] P. Babilotte, P. Ruello, T. Pezeril, G. Vaudel, D. Mounier, J.-M. Breteau, and V. Gusev, Transition from piezoelectric to deformation potential mechanism of hypersound photogeneration in n-doped gaas semiconductors, Journal of Applied Physics **109**, 064909 (2011).

[117] G.-W. Chern, K.-H. Lin, and C.-K. Sun, Transmission of light through quantum heterostructures modulated by coherent acoustic phonons, Journal of Applied Physics **95**, 1114 (2004).

[118] G. D. Sanders, C. J. Stanton, and C. Sub Kim, Theory of coherent acoustic phonons in $in_xga_{1-x}N$/GaN multiple quantum wells, Phys. Rev. B **64**, 235316 (2001).

[119] J. T. Kobayashi, N. P. Kobayashi, and P. D. Dapkus, Nucleation and growth behavior for gan grown on (0001) sapphire via multistep growth approach, J. Electron. Mater. **26**, 1114 (1997).

[120] O. Lagerstedt and B. Monemar, Variation of lattice parameters in gan with stoichiometry and doping, Phys. Rev. B **19** (1979).

[121] S. F. Chichibu, A. C. Abare, M. S. Minsky, S. Keller, S. B. Fleischer, J. E. Bowers, E. Hu, U. K. Mishra, L. A. Coldren, S. P. DenBaars, and T. Sota, Effective band gap inhomogeneity and piezoelectric field in ingan/gan multiquantum well structures, Applied Physics Letters **73**, 2006 (1998).

[122] S. Chuang, *Physics of Optoelectronic Devices*, Wiley Series in Pure and Applied Optics (Wiley, 1995).

[123] D. A. B. Miller, D. S. Chemla, and S. Schmitt-Rink, Relation between electroabsorption in bulk semiconductors and in quantum wells: The quantum-confined franz-keldysh effect, Phys. Rev. B **33**, 6976 (1986).

[124] P.-A. Mante, Y.-R. Huang, S.-C. Yang, T.-M. Liu, A. A. Maznev, J.-K. Sheu, and C.-K. Sun, Thz acoustic phonon spectroscopy and nanoscopy by using piezoelectric semiconductor heterostructures, Ultrasonics **56**, 52 (2015).

[125] C. Boney, D. Starikov, I. Hernandez, R. Pillai, and A. Bensaoula, Molecular beam epitaxy growth of ingan-gan superlattices for optoelectronic devices, Journal of Vacuum Science and Technology B **29**, 03C106 (2011).

[126] C. Deger, E. Born, H. Angerer, O. Ambacher, M. Stutzmann, J. Hornsteiner, E. Riha, and G. Fischerauer, Sound velocity of $in_xga_{1-x}N$ thin films obtained by surface acoustic-wave measurements, Applied Physics Letters **72**, 2400 (1998).

[127] T. Kuech, *Handbook of Crystal Growth: Thin Films and Epitaxy*, 2nd ed., Handbook of Crystal Growth (Elsevier Science, 2014).

[128] K. Kusakabe and K. Ohkawa, X-ray diffraction study of ingan/gan superlattice interfaces, Journal of Vacuum Science and Technology B: Microelectronics and Nanometer Structures **21** (2003).

[129] L. Lindsay, D. A. Broido, and T. L. Reinecke, Thermal conductivity and large isotope effect in gan from first principles, Phys. Rev. Lett. **109**, 095901 (2012).

[130] A. A. Maznev, T.-C. Hung, Y.-T. Yao, T.-H. Chou, J. S. Gandhi, L. Lindsay, H. D. Shin, D. W. Stokes, R. L. Forrest, A. Bensaoula, C.-K. Sun, and K. A. Nelson, Propagation of thz acoustic wave packets in gan at room temperature, Applied Physics Letters **112**, 061903 (2018).

[131] T. M. Tritt, *Thermal Conductivity: Theory, Properties, and Applications*, us ed., Physics of Solids and Liquids (Springer, 2004).

[132] B. Liao, B. Qiu, J. Zhou, S. Huberman, K. Esfarjani, and G. Chen, Significant reduction of lattice thermal conductivity by the electron-phonon interaction in silicon with high carrier concentrations: A first-principles study, Phys. Rev. Lett. **114**, 115901 (2015).

[133] J. Zhou, B. Liao, and G. Chen, First-principles calculations of thermal, electrical, and thermoelectric transport properties of semiconductors, Semiconductor Science and Technology **31**, 043001 (2016).

[134] G. Chen, *Nanoscale Energy Transport and Conversion: A Parallel Treatment of Electrons, Molecules, Phonons, and Photons*, MIT-Pappalardo Series in Mechanical Engineering (Oxford University Press, 2005).

[135] M. G. Holland, Phonon scattering in semiconductors from thermal conductivity studies, Phys. Rev. **134**, A471 (1964).

[136] D. T. Morelli, J. P. Heremans, C. P. Beetz, W. S. Yoo, and H. Matsunami, Phonon-electron scattering in single crystal silicon carbide, Applied Physics Letters **63**, 3143 (1993).

[137] D. Bansal, C. Li, A. H. Said, D. L. Abernathy, J.-Q. Yan, and O. Delaire, Electron-phonon coupling and thermal transport in the thermoelectric compound mo3sb7-xtex, Physical Review B **92** (2015).

[138] M. Pomerantz, Ultrasonic loss and gain mechanisms in semiconductors, Proceedings of the IEEE **53**, 1438 (1965).

[139] J. C. Hensel, R. Dynes, and D. C. Tsui, Absorption of ballistic phonons by the (001) inversion layer of si: Electron-phonon interaction in two dimensions, Physical Review B **28**, 1124 (1983).

[140] A. Wixforth, J. P. Kotthaus, and G. Weimann, Quantum oscillations in the surface-acoustic-wave attenuation caused by a two-dimensional electron system, Phys. Rev. Lett. **56**, 2104 (1986).

[141] S. Sze and K. Ng, *Physics of Semiconductor Devices* (Wiley, 2006).

[142] Y. Pei, X. Shi, A. LaLonde, H. Wang, L. Chen, and G. J. Snyder, Convergence of electronic bands for high performance bulk thermoelectrics, Nature **473**, 66 EP (2011).

[143] K. Biswas, J. He, I. D. Blum, C.-I. Wu, T. P. Hogan, D. N. Seidman, V. P. Dravid, and M. G. Kanatzidis, High-performance bulk thermoelectrics with all-scale hierarchical architectures, Nature **489**, 414 EP (2012).

[144] B. Liao, A. A. Maznev, K. A. Nelson, and G. Chen, Photo-excited charge carriers suppress sub-terahertz phonon mode in silicon at room temperature, Nature Communications **7**, 13174 EP (2016), article.

[145] D. A. Young, C. Thomsen, H. T. Grahn, H. J. Maris, and J. Tauc, Heat flow in glasses on a picosecond timescale, in *Phonon Scattering in Condensed Matter V*, edited by A. C. Anderson and J. P. Wolfe (Springer Berlin Heidelberg, Berlin, Heidelberg, 1986) pp. 49–51.

[146] C. A. Paddock and G. L. Eesley, Transient thermoreflectance from thin metal films, Journal of Applied Physics **60**, 285 (1986).

[147] W. S. Capinski, H. J. Maris, T. Ruf, M. Cardona, K. Ploog, and D. S. Katzer, Thermal-conductivity measurements of gaas/alas superlattices using a picosecond optical pump-and-probe technique, Phys. Rev. B **59**, 8105 (1999).

[148] D. G. Cahill, W. K. Ford, K. E. Goodson, G. D. Mahan, A. Majumdar, H. J. Maris, R. Merlin, and S. R. Phillpot, Nanoscale thermal transport, Journal of Applied Physics **93**, 793 (2003).

[149] S. D. Brorson, J. G. Fujimoto, and E. P. Ippen, Femtosecond electronic heat-transport dynamics in thin gold films, Phys. Rev. Lett. **59**, 1962 (1987).

[150] R. W. Schoenlein, W. Z. Lin, J. G. Fujimoto, and G. L. Eesley, Femtosecond studies of nonequilibrium electronic processes in metals, Physical review letters **58**, 1680 (1987).

[151] J. Hohlfeld, S.-S. Wellershoff, J. Güdde, U. Conrad, V. Jähnke, and E. Matthias, Electron and lattice dynamics following optical excitation of metals, Chemical Physics **251**, 237 (2000).

[152] D. G. Cahill, P. V. Braun, G. Chen, D. R. Clarke, S. Fan, K. E. Goodson, P. Keblinski, W. P. King, G. D. Mahan, A. Majumdar, H. J. Maris, S. R. Phillpot, E. Pop, and L. Shi, Nanoscale thermal transport. ii. 2003–2012, Applied Physics Reviews **1**, 011305 (2014).

[153] M. G. Burzo, P. L. Komarov, and P. E. Raad, Minimizing the uncertainties associated with the measurement of thermal properties by the transient thermoreflectance method, IEEE Transactions on Components and Packaging Technologies **28**, 39 (2005).

[154] A. J. Schmidt, *Optical Characterization of Thermal Transport from the Nanoscale to the Macroscle*, Ph.D. thesis, Massachusetts Institute of Technology (2008).

[155] D. K. Schroder, Carrier lifetimes in silicon, IEEE Transactions on Electron Devices **44**, 160 (1997).

[156] J. A. del Alamo and R. M. Swanson, Modelling of minority-carrier transport in heavily doped silicon emitters, Solid-State Electronics **30**, 1127 (1987).

[157] M. Tyagi and R. V. Overstraeten, Minority carrier recombination in heavily-doped silicon, Solid-State Electronics **26**, 577 (1983).

[158] E. T. Swartz and R. O. Pohl, Thermal boundary resistance, Rev. Mod. Phys. **61**, 605 (1989).

[159] H. Kinder and K. Weiss, Kapitza conduction by thin lossy surface layers, Journal of Physics: Condensed Matter **5**, 2063 (1993).

[160] O. B. Wright, Thickness and sound velocity measurement in thin transparent films with laser picosecond acoustics, Journal of Applied Physics **71**, 1617 (1992).

[161] G.-M. Choi, R. B. Wilson, and D. G. Cahill, Indirect heating of pt by short-pulse laser irradiation of au in a nanoscale pt/au bilayer, Phys. Rev. B **89**, 064307 (2014).

[162] B. Vermeersch, A. M. S. Mohammed, G. Pernot, Y. R. Koh, and A. Shakouri, Thermal interfacial transport in the presence of ballistic heat modes, Phys. Rev. B **90**, 014306 (2014).

[163] W. S. Capinski and H. J. Maris, Improved apparatus for picosecond pump-and-probe optical measurements, Review of Scientific Instruments **67**, 2720 (1996).

[164] B. G. Streetman and S. Banerjee, *Solid state electronic devices*, 5th ed. (Upper Saddle River, N.J. : Prentice Hall, 2000).

[165] M. Asheghi, M. N. Touzelbaev, K. E. Goodson, Y. K. Leung, and S. S. Wong, Temperature-dependent thermal conductivity of single-crystal silicon layers in soi substrates, Journal of Heat Transfer **120**, 30 (1998).